THE GEOLOGICAL SOCIETY OF AMERICA®

Cenozoic kinematic histories of the Tidding and Lohit thrusts in the northern Indo-Burma Ranges: Implications for crustal thickening and exhumation of Gangdese lower arc crust along the Indus-Yarlung suture zone

Peter J. Haproff[1,†], Drew A. Levy[2], Andrew V. Zuza[2], Julian D. Hooker[1], Matthew T. Heizler[3], Daniel F. Stockli[4], and Mary Braza[5]

[1]*Department of Earth and Ocean Sciences, University of North Carolina Wilmington, North Carolina 28403, USA*
[2]*Nevada Bureau of Mines and Geology, University of Nevada, Reno, Nevada 89557, USA*
[3]*New Mexico Bureau of Geology and Mineral Resources, New Mexico Tech, Socorro, New Mexico 87801, USA*
[4]*Department of Geological Sciences, University of Texas, Austin, Texas 79712, USA*
[5]*Department of Geology and Environmental Science, University of Pittsburgh, Pennsylvania 15260, USA*

ABSTRACT

Crustal thickening has been a key process of collision-induced Cenozoic deformation along the Indus-Yarlung suture zone, yet the timing, geometric relationships, and along-strike continuities of major thrusts, such as the Great Counter thrust and Gangdese thrust, remain inadequately understood. In this study, we present findings of geologic mapping and thermo- and geochronologic, geochemical, microstructural, and geothermobarometric analyses from the easternmost Indus-Yarlung suture zone exposed in the northern Indo-Burma Ranges. Specifically, we investigate the Lohit and Tidding thrust shear zones and their respective hanging wall rocks of the Lohit Plutonic Complex and Tidding and Mayodia mélange complexes. Field observations are consistent with ductile deformation concentrated along the top-to-the-south Tidding thrust shear zone, which is in contrast to the top-to-the-north Great Counter thrust at the same structural position to the west. Upper amphibolite-facies metamorphism of mélange rocks at ~9–10 kbar (~34–39 km) occurred prior to ca. 36–30 Ma exhumation during slip along the Tidding thrust shear zone. To the north, the ~5-km-wide Lohit thrust shear zone has a subvertical geometry and north-side-up kinematics. Cretaceous arc granitoids of the Lohit Plutonic Complex were emplaced at ~32–40 km depth in crust estimated to be ~38–52 km thick at that time. These rocks cooled from ca. 25 Ma to 10 Ma due to slip along the Lohit thrust shear zone. We demonstrate that the Lohit thrust shear zone, Gangdese thrust, and Yarlung-Tsangpo Canyon thrust have comparable hanging wall and footwall rocks, structural geometries, kinematics, and timing. Based on these similarities, we interpret that these thrusts formed segments of a laterally continuous thrust system, which served as the preeminent crustal thickening structure along the Neotethys-southern Lhasa terrane margin and exhumed Gangdese lower arc crust in Oligocene–Miocene time.

INTRODUCTION

Since the onset of India-Asia collision at ca. 60 Ma, crustal thickening has been partially accommodated by shortening across orogenic belts adjacent to the collisional boundary. These belts include: (1) the east-trending Himalayan orogen and southern Lhasa terrane (Le Fort, 1975; Hodges, 2000; Yin and Harrison, 2000; DeCelles et al., 2001; Yin, 2006; Kapp and DeCelles, 2019); and (2) the two north-trending orogenic belts that extend southwards from the eastern and western Himalayan syntaxes (Gansser, 1964; Yin, 2006; Haproff et al., 2018, 2020; Fig. 1A). The geometries, slip magnitudes, and lifespans of crustal-scale contractional structures of the Himalayan orogen and southern Lhasa terrane have been investigated (e.g., Ratschbacher et al., 1994; Quidelleur et al., 1997; Yin et al., 1999; Harrison et al., 2000; Catlos et al., 2001; Murphy and Yin, 2003; Robinson et al., 2003; McQuarrie et al., 2008; Mitra et al., 2010; Long et al., 2011; DeCelles et al., 2016; Kellett et al., 2019; Webb et al., 2017; Fig. 1B). In contrast, major contractional structures located southeast and south of the eastern Himalayan syntaxis are less well understood (cf. Nielsen et al., 2004; Maurin and Rangin, 2009; Rangin et al., 2013; Wang et al., 2014; Betka et al., 2018; Morley et al., 2020; Fig. 1A).

In the northern Indo-Burma Ranges, located directly southeast of the eastern Himalayan syntaxis, two major contractional structures are the Lohit thrust shear zone and the structurally lower Tidding thrust shear zone that mark the respective lower boundaries of the easternmost Cretaceous Gangdese belt and Mesoproterozoic basement of Lhasa terrane (i.e., Lohit Plutonic Complex) and the Indus-Yarlung suture zone (i.e., Tidding and Mayodia mélange complexes) (Dhoundial et al., 1971; Nandy, 1973, 1976; Gururajan and Choudhuri, 2003; Misra, 2009; Singh and Singh, 2011, 2013; Lin et al., 2013; Bikramaditya et al., 2020; Haproff et al., 2018, 2019; Pebam and Kamalakannan, 2019; Fig. 2). Contractional structures to the west that appear to be analogous based on their structural positions and hanging wall and footwall rocks are the late Oligocene–Miocene Great Counter thrust and the Oligocene–early Miocene Gangdese thrust, which mark the boundaries between the Himalayan orogen, Indus-Yarlung suture zone, and southern Lhasa terrane (Heim and Gansser, 1939; Harrison et al., 1992; Yin et al., 1994, 1999; Fig. 1B). The existence of the Gangdese thrust is

Peter Haproff https://orcid.org/0000-0002-3119-2290
[†]haproffp@uncw.edu.

GSA Bulletin;
published online 21 November 2022

https://doi.org/10.1130/B36323.1; 14 figures; 4 tables; 1 supplemental file.

For permission to copy, contact editing@geosociety.org
© 2022 Geological Society of America

Downloaded from http://pubs.geoscienceworld.org/gsa/gsabulletin/article-pdf/doi/10.1130/B36323.1/5738725/b36323.pdf
by University of Nevada Reno user

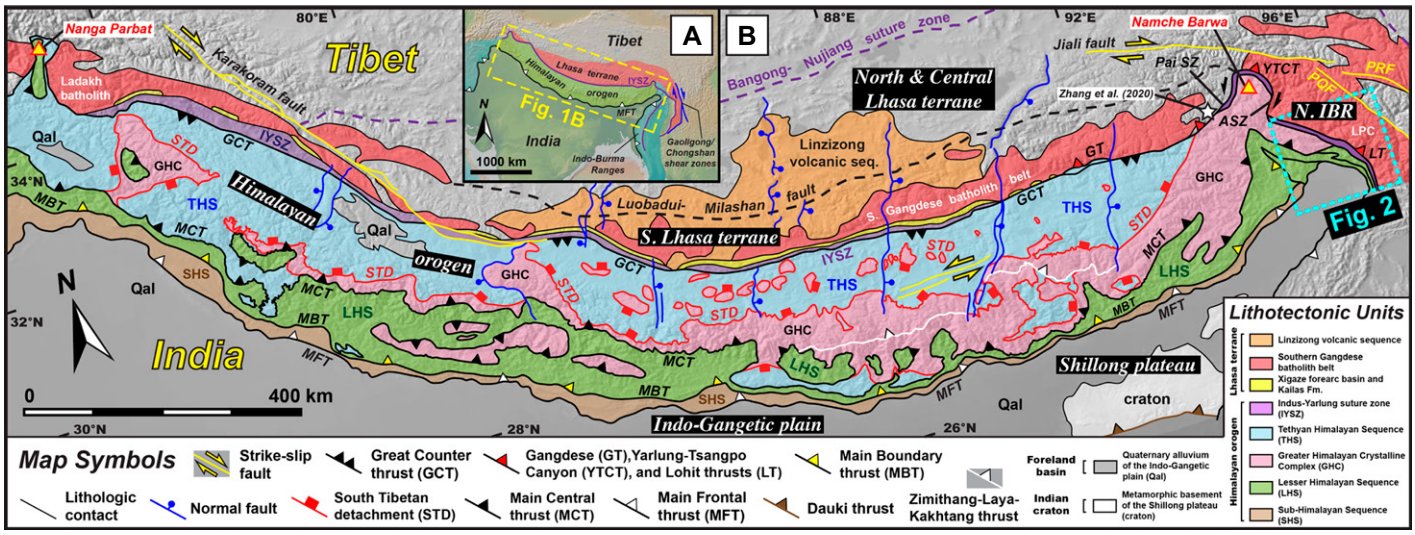

Figure 1. Simplified geologic maps show (A) the India-Asia collisional zone and (B) the Himalayan orogen, southern Lhasa terrane, and northern Indo-Burma Ranges, modified from Webb et al. (2017). Basemap is from geomapapp.org (Ryan et al., 2009). ASZ—Aniqiao shear zone; LPC—Lohit Plutonic Complex; N. IBR—northern Indo-Burma Ranges; PQF—Puqu fault; PRF—Parlung fault; SZ—shear zone.

disputed (Aitchison et al., 2003), yet identifications of: (1) coeval Miocene cooling ages at the eastern Himalayan syntaxis (Booth et al., 2004; Gong et al., 2015); (2) comparable structures including the Yarlung-Tsangpo Canyon thrust (Ding et al., 2001) and Lohit thrust shear zone to the east (Nandy, 1976); and (3) orogen-parallel continuations of lithotectonic units across the syntaxis (Lin et al., 2013; Bikramaditya et al., 2020; Haproff et al., 2019; Pebam and Kamalakannan, 2019; Fig. 3) imply that a laterally continuous and synchronous, south-directed thrust system accommodated crustal thickening along much of the India-Asia collisional boundary. In addition, it is unknown whether the Tidding and Lohit thrust shear zones were coeval with several major strike-slip shear zones located directly to the northeast and east (e.g., the Jiali fault, Gaoligong shear zone, and Chongshan shear zone; Fig. 1A), which could elucidate how strain has been partitioned surrounding northeastern India (e.g., Haproff et al., 2020).

In this study, we conducted geologic mapping and sampling of the Lohit Plutonic Complex, Lohit thrust shear zone, Tidding mélange complex, and Tidding thrust shear zone exposed along the Trans-Arunachal Highway of Dibang Valley in

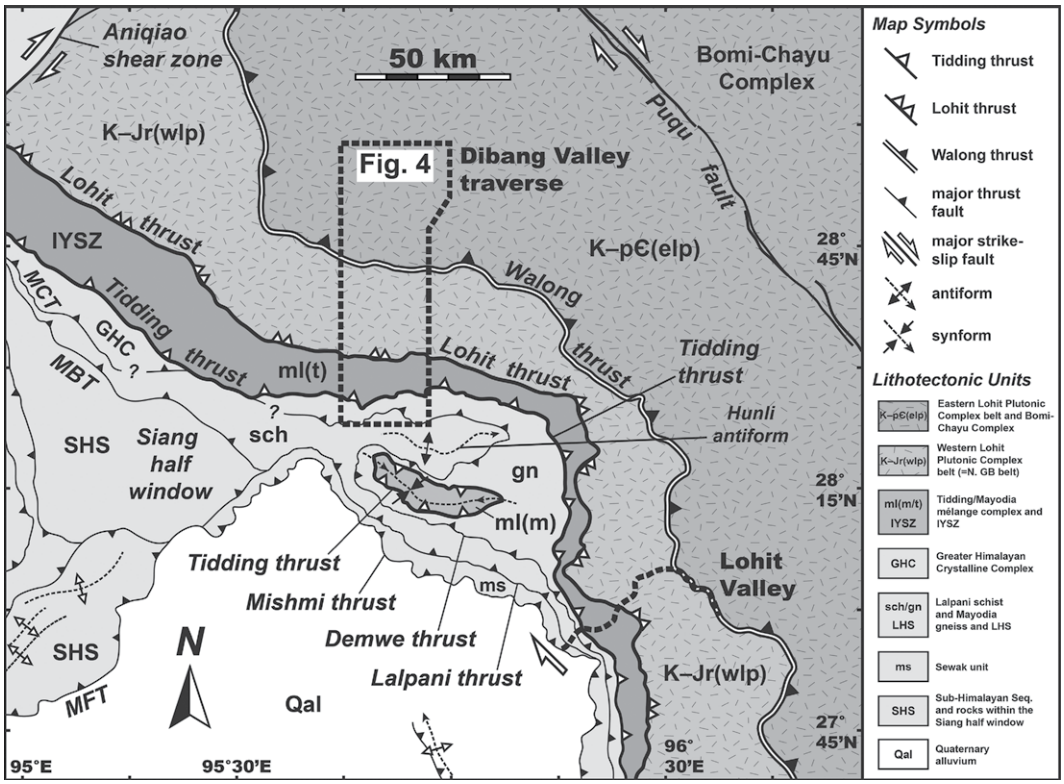

Figure 2. Simplified geologic map of the northern Indo-Burma Ranges shows the locations of the Dibang Valley traverse (Fig. 4) and Lohit Valley, modified from Haproff et al. (2019). Map location is shown in Figure 1. Basemap is from geomapapp.org (Ryan et al., 2009). MCT—Main Central thrust; MFT—Main Frontal thrust; MBT—Main Boundary thrust.

Downloaded from http://pubs.geoscienceworld.org/gsa/gsabulletin/article-pdf/doi/10.1130/B36323.1/5738725/b36323.pdf
by University of Nevada Reno user

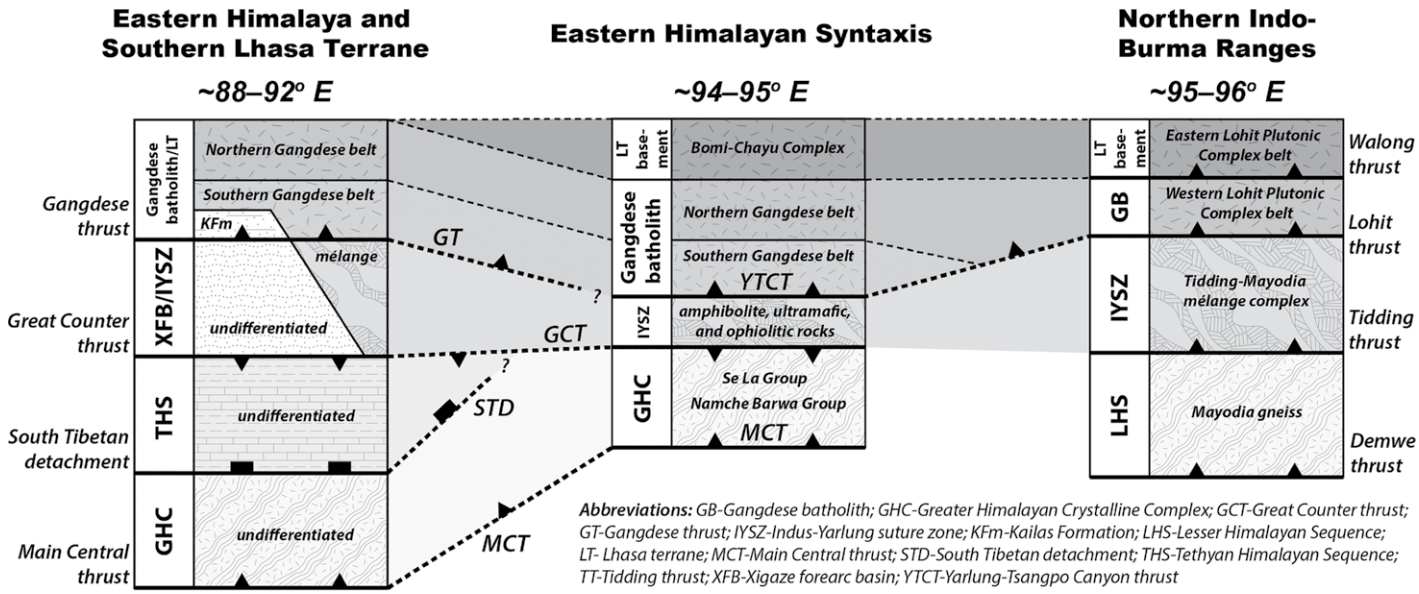

Figure 3. Simplified tectonostratigraphic column shows orogen-parallel correlations and terminations of major lithotectonic units and structures of the eastern Himalaya and southern Lhasa terrane, eastern Himalayan syntaxis (hanging wall of the Main Central thrust), and northern Indo-Burma Ranges (hanging wall of the Demwe thrust). Figure is modified from Haproff et al. (2019).

the northern Indo-Burma Ranges (Figs. 2 and 3). Microstructural observations and results of electron backscatter diffraction (EBSD) analyses from across the Lohit thrust shear zone reveal deformation conditions and mechanisms. By combining new and existing thermo- and geochronologic, geochemical, and geothermobarometric data, we document the depths of Cretaceous pluton emplacement and crustal thickness of the Lohit Plutonic Complex, metamorphic conditions of the Tidding mélange complex, and the timing of Cenozoic slip along the Tidding and Lohit thrust shear zones. These constraints are incorporated in a structural model that improves our understanding of the Cenozoic crustal thickening history of the India-Asia collisional boundary.

GEOLOGIC SETTING

Southern Lhasa Terrane and Indus-Yarlung Suture Zone

The ~100-km-wide southern Lhasa terrane is bounded by the east-striking Luobadui-Milashan fault to the north (Zhang et al., 2014) and the Indus-Yarlung suture zone to the south (Fig. 1B). The southern Lhasa terrane mostly comprises bimodal volcanic rocks of the Paleocene–Eocene Linzizong volcanic sequence (Coulon et al., 1986; Ding et al., 2003; He et al., 2007; Lee et al., 2009; Zhu et al., 2015), and plutonic rocks of the Gangdese batholith, which is divided into a Triassic–Cretaceous northern belt and a Cretaceous–Eocene southern belt (Schärer et al., 1984; Coulon et al., 1986; Debon et al., 1986; Copeland et al., 1995; Wen et al., 2008; Zhu et al., 2008, 2009; Ji et al., 2009; Wang et al., 2016; Fig. 1B). Oligocene–Miocene siliciclastic strata of the Kailas Formation overlie the southern Gangdese batholith along much of its southern margin (Gansser, 1964; Aitchison et al., 2002; DeCelles et al., 2011, 2016; Leary et al., 2016; Laskowski et al., 2018; Fig. 1B). South of the Kailas Formation, the Xigaze forearc basin consists of Cretaceous–Paleogene marine and nonmarine strata (Garzanti and Van Haver, 1988; Einsele et al., 1994; Dürr, 1996; Ding et al., 2005; Wang et al., 2012; An et al., 2014; Orme et al., 2015).

The Indus-Yarlung suture zone marks the India-Asia collisional boundary (Fig. 1) and consists of Jurassic–Cretaceous serpentinite-, ophiolitic-, and sedimentary-matrix mélange and Mesozoic–Cenozoic subduction-related metamorphic rocks (Gansser, 1964; McDermid et al., 2002; Malpas et al., 2003; Ziabrev et al., 2003; Dupuis et al., 2005; Dai et al., 2011; Hébert et al., 2012; Cai et al., 2012; Laskowski et al., 2016). The Indus-Yarlung suture zone is bound by two thrust systems: the south-directed Gangdese thrust (Harrison et al., 1992; Yin et al., 1994) and the north-directed Great Counter thrust (Heim and Gansser, 1939; Figs. 1B and 3).

The Gangdese thrust is exposed directly east of the city of Zedong (~92°E longitude), where it places Paleozoic–Mesozoic strata and Cretaceous–Cenozoic granitoids of the southern Gangdese batholith atop Tertiary conglomerate, Cretaceous volcanic rocks, Late Cretaceous and Tertiary syenite, and mélanges of the Indus-Yarlung suture zone (Yin et al., 1994, 1999; Harrison et al., 2000; Figs. 1B and 3). Thermo- and geochronologic investigations suggest that the Gangdese thrust was active ca. 27–23 Ma (Yin et al., 1999; Harrison et al., 2000) with a lower age bound of ca. 18 Ma based on $^{40}Ar/^{39}Ar$ ages of a cross-cutting andesitic dike (Yin et al., 1994). The Gangdese thrust accommodated at least ~50 km of southward displacement (Yin et al., 1994; Harrison et al., 2000).

Some regional geologic maps of the eastern Himalayan syntaxis show the Gangdese thrust as far east as ~94°30′E, where it links with the southwest-striking, left-slip Pai shear zone along the western limb of the north-plunging Namche Barwa antiform (e.g., Ding et al., 2001) (Fig. 1B). The Pai shear zone links with the south-directed Yarlung-Tsangpo Canyon thrust, which, like the Gangdese thrust, places granitoids of the Gangdese batholith atop mélange of the Indus-Yarlung suture zone and metasedimentary rocks of Indian affinity including the Tethyan Himalayan sequence and Greater Himalayan Crystalline Complex (Figs. 1B and 3). Along the western limb of the Namche Barwa antiform, the Yarlung-Tsangpo Canyon thrust transitions to the southwest-striking, right-slip Aniqiao shear zone, the latter of which links with the Lohit thrust shear zone to the south (Figs. 1B and 3). Ding et al. (2001) proposed two models for the roles of these faults in forming the Namche Barwa antiform. In one model, the Pai shear zone, Yarlung-Tsangpo Canyon thrust, and Aniqiao shear zone originated as a single roof thrust of a crustal-scale duplex that was

Downloaded from http://pubs.geoscienceworld.org/gsa/gsabulletin/article-pdf/doi/10.1130/B36323.1/5738725/b36323.pdf
by University of Nevada Reno user

subsequently folded during exhumation of the Namche Barwa massif. In the alternative model, the Pai and Aniqiao shear zones transferred slip between the Gangdese thrust in the west, the Yarlung-Tsangpo Canyon thrust, and the Lohit thrust shear zone in the east during northward indentation of folded Indian crust. Gangdese-equivalent granitoids in the hanging wall of the Yarlung-Tsangpo Canyon thrust and along the western and eastern limbs of the Namche Barwa antiform yield ca. 23–13 Ma biotite $^{40}Ar/^{39}Ar$ ages (Gong et al., 2015, and references therein) and two ca. 21 Ma U–Pb zircon ages (Booth et al., 2004). Thermochronologic ages of ca. 11–1 Ma are concentrated within the core and immediate vicinity of the Namche Barwa antiform, which has been interpreted to be related to coeval high-grade metamorphism, anatexis, and rapid crustal exhumation driven by focused erosion (Ding et al., 2001; Booth et al., 2009; Zeitler et al., 2014; Gong et al., 2015; Govin et al., 2020).

In contrast to the intermittently exposed Gangdese thrust, the Great Counter thrust is well exposed along much of the Himalayan orogen–southern Lhasa terrane boundary (Fig. 1B). Near Xigaze (~88°E) and to the west, the Great Counter thrust cuts the Tethyan Himalayan sequence, whereas near Zedong (~92°E) and to the east, several splays of the thrust place the Tethyan Himalayan sequence atop mélanges of the Indus-Yarlung suture zone, strata of the Xigaze forearc basin, and plutonic rocks of the southern Gangdese batholith (Yin et al., 1994, 1999; Figs. 1B and 3). The Great Counter thrust was active at ca. 25–10 Ma (Yin et al., 1999; Harrison et al., 2000; Wang et al., 2015; Laskowski et al., 2018) and accommodated at least ~12 km of northward displacement (Quidelleur et al., 1997). Laskowski et al. (2018) postulated that the multiple splays of the Great Counter thrust form a foreland-dipping, passive roof duplex that repeats the Xigaze forearc basin and mélanges of the Indus-Yarlung suture zone. In this "Gangdese culmination model," the Great Counter thrust duplex system is kinematically linked with the Gangdese thrust as part of a blind hinterland-dipping duplex in the southern Lhasa terrane to the north.

Himalayan Orogen

The east-trending Himalayan orogen is a ~200–300-km-wide thrust belt located between the Indus-Yarlung suture zone to the north and the Indo-Gangetic plain to the south (Yin, 2006; Fig. 1B). The Himalayan orogen terminates at the eastern and western Himalayan syntaxes, where the orogen makes ~90° oroclinal bends to the south (Fig. 1A). Major lithotectonic units of the Himalayan orogen from north to south consist of: (1) Proterozoic–Eocene unmetamorphosed to low-grade metasedimentary and metavolcanic rocks of the Tethyan Himalayan sequence; (2) Paleoproterozoic–Ordovician high-grade metamorphic rocks and migmatite, ca. 500 Ma granitoids, and Miocene leucogranites of the Greater Himalayan Crystalline Complex; (3) Proterozoic–Cambrian medium- to low-grade metasedimentary and metavolcanic rocks of the Lesser Himalayan sequence; and (4) late Cenozoic siliciclastic strata of the Sub-Himalayan sequence. These lithotectonic units are separated by the north-directed South Tibetan detachment, the south-directed Main Central thrust, the south-directed Main Boundary thrust, and the south-directed Main Frontal thrust (Heim and Gansser, 1939; Gansser, 1964; Le Fort, 1975; Yin and Harrison, 2000; Yin, 2006; Kapp and DeCelles, 2019; Fig. 1B).

Northern Indo-Burma Ranges

The northwest- to north-trending northern Indo-Burma Ranges, located directly southeast of the eastern Himalayan syntaxis, expose a ~100–150-km-wide thrust belt (Nandy, 1973, 1976; Thakur and Jain, 1974, 1975; Misra and Singh, 2002; Gururajan and Choudhuri, 2003; Misra, 2009; Sarma et al., 2012; Ningthoujam et al., 2015; Haproff et al., 2018; Salvi et al., 2020; Figs. 1B and 2). The thrust belt is bound by two active fault systems: the right-lateral oblique-slip Mishmi thrust along the range front to the southwest, and the two southeastern extensions of the right-slip Jiali fault (i.e., the Puqu and Parlung faults) to the northeast (Haproff et al., 2020; Fig. 2). Five laterally continuous lithotectonic units are exposed in the Dibang and Lohit valleys (Fig. 2). The northeasternmost lithotectonic unit is the Lohit Plutonic Complex, which is subdivided into an Eastern Lohit Plutonic Complex belt of predominantly Mesoproterozoic and Cretaceous migmatite, metaigneous rocks, and granitoids, and a Western Lohit Plutonic Complex belt of latest Jurassic–Cretaceous granitoids, separated by the south-directed Walong thrust (Thakur and Jain, 1975; Misra and Singh, 2002; Gururajan and Choudhuri, 2003, 2007; Misra, 2009; Haproff et al., 2018, 2019; Figs. 2 and 3). Mesoproterozoic migmatite and metaigneous rocks of the Eastern Lohit Plutonic Complex belt are correlative with the basement of the Lhasa terrane and the Bomi-Chayu complex exposed at the eastern Himalayan syntaxis (Xu et al., 2013) based on their spatial proximity and similar rock types and crystallization ages (Haproff et al., 2019; Fig. 2). Latest Jurassic–Cretaceous granitoids of the Eastern and Western Lohit Plutonic Complex belts are interpreted to be the southeastward continuation of the Triassic–Cretaceous northern Gangdese batholith (Fig. 1B) based on similar crystallization ages and geochemistry (Gururajan and Choudhuri, 2007; Lin et al., 2013; Haproff et al., 2019; Pebam and Kamalakannan, 2019; Bikramaditya et al., 2020).

The northeastern Eastern Lohit Plutonic Complex belt is cut by the Puqu and Parlung faults (e.g., Molnar and Tapponnier, 1975; Tapponnier and Molnar, 1977; Armijo et al., 1989) (Figs. 1B and 2), which were active at ca. 23–11 Ma (Ding et al., 2001; Lee et al., 2003; Lin et al., 2009) and have since resumed slip as seismogenic faults (Ni and York, 1978; Thingbaijam et al., 2008; Mukhopadhyay and Dasgupta, 2015; Haproff et al., 2020). These strike-slip faults, together with the Gaoligong (ca. 24–12 Ma; Zhong et al., 1991; Lin et al., 2009) and Chongshan (ca. 34–22 Ma and ca. 19–14 Ma; Wang et al., 2006; Akciz et al., 2008; Zhang et al., 2010) shear zones located ~200 km to the southeast (Fig. 1A), accommodated southward extrusion of Asian lithosphere around the eastern Himalayan syntaxis.

Structurally beneath the Walong thrust, the Lohit thrust shear zone places the Western Lohit Plutonic Complex belt atop metasedimentary rocks, metaigneous, and serpentinized ultramafic rocks of the Tidding mélange complex and the Tidding thrust at its base (Dhoundial et al., 1971; Gururajan and Choudhuri, 2003; Quanru et al., 2006; Misra, 2009; Haproff et al., 2019; Dutt et al., 2021a 2021b; Fig. 2). Similar sedimentary- and serpentinite-matrix mélange rocks of the Mayodia mélange complex are exposed within a thrust-bound klippe located ~30 km south of the Tidding mélange complex (Fig. 2). From this structural architecture, Haproff et al. (2018) interpreted that the Tidding and Mayodia mélange complexes originate from the same tectonic mélange (i.e., the Tidding-Mayodia mélange complex) that was thrust southwards atop the northeastern Greater Indian margin by the Tidding thrust shear zone and subsequently folded and partially eroded. The Tidding and Mayodia mélange complexes are the southeastern extension of the Indus-Yarlung suture zone that continues southwards into the southern Indo-Burma Ranges (Gururajan and Choudhuri, 2003; Misra, 2009; Saha et al., 2012; Singh and Singh, 2013; Fig. 1A).

The Tidding thrust shear zone places the Tidding and Mayodia mélange complexes atop metasedimentary rocks with detrital zircon age spectra similar to those of the Lesser Himalayan sequence (Haproff et al., 2019). These metasedimentary rocks consist of paragneiss, augen gneiss, and quartzo-feldspathic schist of the Mayodia gneiss and quartzo-feldspathic schist, paragneiss, quartzite, and marble of the structurally lower Lalpani schist (Gururajan and Choudhuri, 2003; Misra, 2009; Haproff et al.,

Downloaded from http://pubs.geoscienceworld.org/gsa/gsabulletin/article-pdf/doi/10.1130/B36323.1/5738725/b36323.pdf
by University of Nevada Reno user

2019; Fig. 2). The Mayodia gneiss and Lalpani schist are separated by the south-directed Demwe thrust, which is also known as the Mayodia thrust (Salvi et al., 2020; Fig. 2). In the core of the thrust belt, the Demwe thrust is folded into the northwest-trending Hunli antiform (Fig. 2) above a duplex (Haproff et al., 2018, 2020; Salvi et al., 2020). Below the Demwe thrust, the mylonitic Lalpani thrust places the Lalpani schist atop quartzite, marble, chert, slate, phyllite, and quartzo-feldspathic schist of the Sewak unit (Gururajan and Choudhuri, 2003; Misra, 2009; Fig. 2). The southwesternmost thrust in the northern Indo-Burma Ranges is the active, range-bounding Mishmi thrust, which places the Sewak unit atop Quaternary foreland basin strata of the Brahmaputra River plain (Fig. 2). The Mishmi thrust is the southeastern continuation of the Main Frontal thrust and may have a right-lateral component based on a recalculated focal mechanism for the M_W 8.7 1950 Assam earthquake (Coudurier-Curveur et al., 2020) and displaced Quaternary fluvial terraces (Haproff et al., 2018, 2020).

LITHOLOGIC AND STRUCTURAL OBSERVATIONS

We conducted geologic mapping along northern Dibang Valley during the winters of 2013, 2015, and 2020 to document rock types and structures of the Western and Eastern Lohit Plutonic Complex belts, Lohit thrust shear zone, Tidding mélange complex, and Tidding thrust shear zone (Figs. 4 and 5). Representative samples were collected during this and previous field seasons for U–Pb zircon geochronology, geochemistry, $^{40}Ar/^{39}Ar$ thermochronology, geothermobarometry, and EBSD analyses.

Eastern Lohit Plutonic Complex Belt and Walong Thrust

The Eastern Lohit Plutonic Complex belt is the northernmost lithotectonic unit exposed along Dibang Valley and comprises two lithologic units: (1) well-foliated garnet migmatitic orthogneiss with minor amphibolite, mafic dikes, deformed leucogneiss, and undeformed leucogranite bodies (abbreviated "mogn" in Figs. 4A and 5), and (2) weakly foliated to undeformed granitoid of intermediate and felsic composition with minor gabbro, leucogranite, and mafic dikes (abbreviated "gr" in Figs. 4A and 5). U–Pb zircon crystallization ages of Eastern Lohit Plutonic Complex migmatitic orthogneiss and granitoids are ca. 1286 Ma and ca. 135–69 Ma, respectively (Haproff et al., 2019; Fig. 4A).

The migmatitic orthogneiss unit is exposed in two sections of Dibang Valley (Fig. 4A) and contains quartz- and feldspar-rich felsic and pyroxene- and amphibole-rich amphibolite compositional layers with thicknesses ranging from ~1 cm to ~3 m (Figs. 6A–6C). Quartz- and feldspar-rich felsic layers often contain abundant ~1-mm- to ~5-cm-diameter garnet grains (Fig. 6C). A well-developed foliation, defined by flattened felsic and mafic minerals oriented parallel to the compositional layers, strikes east-northeast and dips ~90–20° northwest and southeast (Figs. 4A and 5). A mineral stretching lineation within the foliation, although weakly developed or not present in most of the migmatitic orthogneiss, trends north–northeast and plunges ~50–20° (Figs. 4A and 5). Undeformed leucogranite and mafic dikes, with thicknesses ranging from tens of centimeters to ~3 m, crosscut the foliation in some locations. Sub-meter–scale shear bands are pervasive within the migmatitic orthogneiss and occur both parallel and perpendicular to the foliation. The migmatitic orthogneiss also contains disharmonic and often isoclinal folds with wavelengths in outcrop between ~1 cm to ~10 m (Fig. 6D). Select measured hinges of macroscopic folds trend northeast and plunge ~90–10° (Fig. 4A). A-type folds are prevalent in some locations, with the mineral stretching lineation parallel to fold hinges.

Two samples were collected from the migmatitic orthogneiss unit of the Eastern Lohit Plutonic Complex belt (Fig. 4A). The northernmost sample, PH-11-10-15-19, contains amphibolite and felsic compositional layers formed by flattened amphibole, muscovite, quartz, and feldspar, which define the east-dipping foliation (19°) (Haproff et al., 2018; Fig. 4A). Sample PH-11-10-15-16 was collected ~5 km southwest of sample PH-11-10-15-19 and consists of similar lithologies. The foliation within the sample strikes 066° and dips 89° southeast (Haproff et al., 2019; Fig. 4A). Felsic compositional layers were targeted for sampling.

The weakly foliated to undeformed, intermediate- to felsic-composition granitoids of the Eastern Lohit Plutonic Complex belt are exposed as a series of ~1- to ~5-km-wide bodies and a single ~15-km-wide body (Figs. 4A and 5). A northward transition from the migmatitic orthogneiss to intermediate- to felsic-composition granitoids features a progressive increase in the width and occurrence of cross-cutting dikes and bodies of granitoid, leucogranite, and gabbro. The density of dikes and bodies increases toward the ~15-km-wide granitoid body that contains rafted blocks of migmatitic orthogneiss along its walls (Fig. 5).

The foliation within the intermediate- to felsic-composition granitoids is defined by flattened felsic and mafic minerals and strikes between east and north and dips between ~80–30° south and west (Figs. 4A and 5). A mineral stretching lineation was not observed (Fig. 4A). At some granitoid outcrops, a separate magmatic foliation is defined by the parallel alignment of euhedral amphibole, biotite, and feldspar crystals and forms ~10-cm- to ~10-m-wavelength folds in outcrop. Sparse, weakly foliated, ~1–5-m-wide leucogranite dikes crosscut the magmatic foliation. Leucogranite dikes and host granitoids are cut by ~1-cm- to ~1-m-wide mafic dikes.

Sample PH-11-11-15-1 is an intermediate-composition granitoid collected from a ~3-km-wide body that intrudes the migmatitic orthogneiss (Fig. 4A). The magmatic foliation within the sampled outcrop strikes 210° and dips 62° northwest (Fig. 4A).

Two thrust shear zones were mapped in contact with the Eastern Lohit Plutonic Complex belt (Fig. 4A). The ~1-m-wide northern thrust shear zone cuts the migmatitic orthogneiss and granitoid (Fig. 4A). The southern shear zone is interpreted to be the Walong thrust, which is expressed as a ~1-km-wide mylonite zone that places the migmatitic orthogneiss and amphibolite of the Eastern Lohit Plutonic Complex belt atop migmatitic orthogneiss of the Western Lohit Plutonic Complex belt (Fig. 4A). Fabric elements within the Walong thrust shear zone consist of a north-dipping mylonitic foliation (~50–60°) and a down-dip, north-plunging mineral stretching lineation (~50°) (Figs. 4A and 5). Ductile kinematic indicators within the Walong thrust shear zone consist of top-to-the-south S-C fabric, asymmetric folds, and asymmetric clasts (Haproff et al., 2020).

Western Lohit Plutonic Complex Belt

The Western Lohit Plutonic Complex belt is the southernmost lithotectonic unit in the hanging wall of the Lohit thrust shear zone along Dibang Valley and comprises two lithologic units: (1) well-foliated migmatitic orthogneiss with minor marble bands, leucogranite, leucogneiss (see Fig. S1 in the Supplemental Material[1]), and gabbro (abbreviated "K(mogn)" in Fig. 4), and (2) weakly to well-foliated granitoids of intermediate composition (abbreviated "K(gr)" in Fig. 4B). The migmatitic orthogneiss unit is exposed in two sections and separated by a single exposure of intermediate composition granitoids (Fig. 4). Both the granitoid and migmatitic orthogneiss units yield Cretaceous U–Pb zircon ages ranging from ca. 144–90 Ma (Lin

[1]Supplemental Material. Methodological details, additional figures, and data tables. Please visit https://doi.org/10.1130/GSAB.S.21067348 to access the supplemental material, and contact editing@geosociety.org with any questions.

Downloaded from http://pubs.geoscienceworld.org/gsa/gsabulletin/article-pdf/doi/10.1130/B36323.1/5738725/b36323.pdf
by University of Nevada Reno user

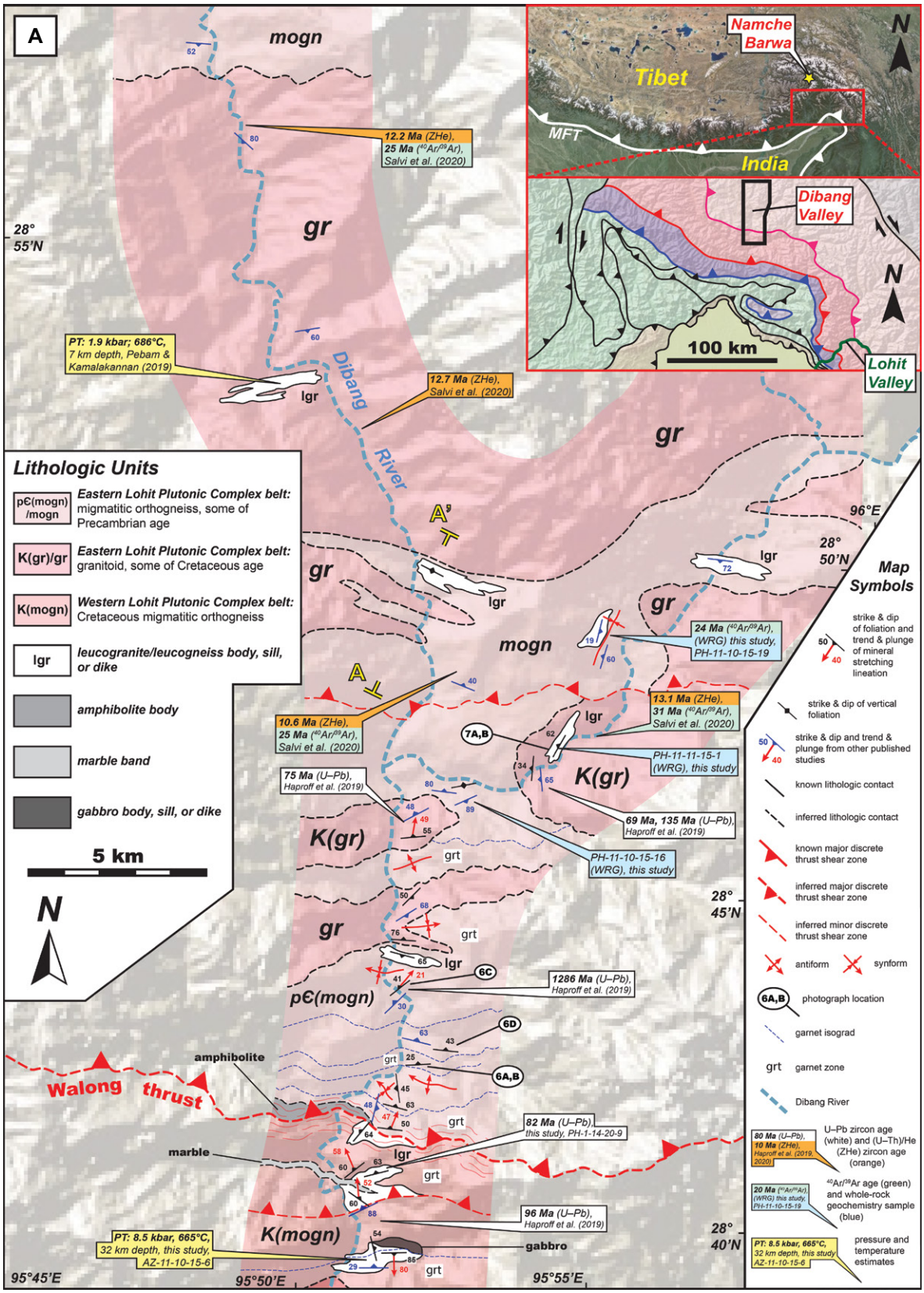

Figure 4. Detailed geologic maps show the (A) northern and (B) southern halves of the Dibang Valley traverse, northern Indo-Burma Ranges. The maps are modified from Haproff et al. (2020). Blue-colored measurement symbols are from Haproff et al. (2018, 2019, 2020). Basemaps are from Google Earth and geomapapp.org (Ryan et al., 2009).

Downloaded from http://pubs.geoscienceworld.org/gsa/gsabulletin/article-pdf/doi/10.1130/B36323.1/5738725/b36323.pdf
by University of Nevada Reno user

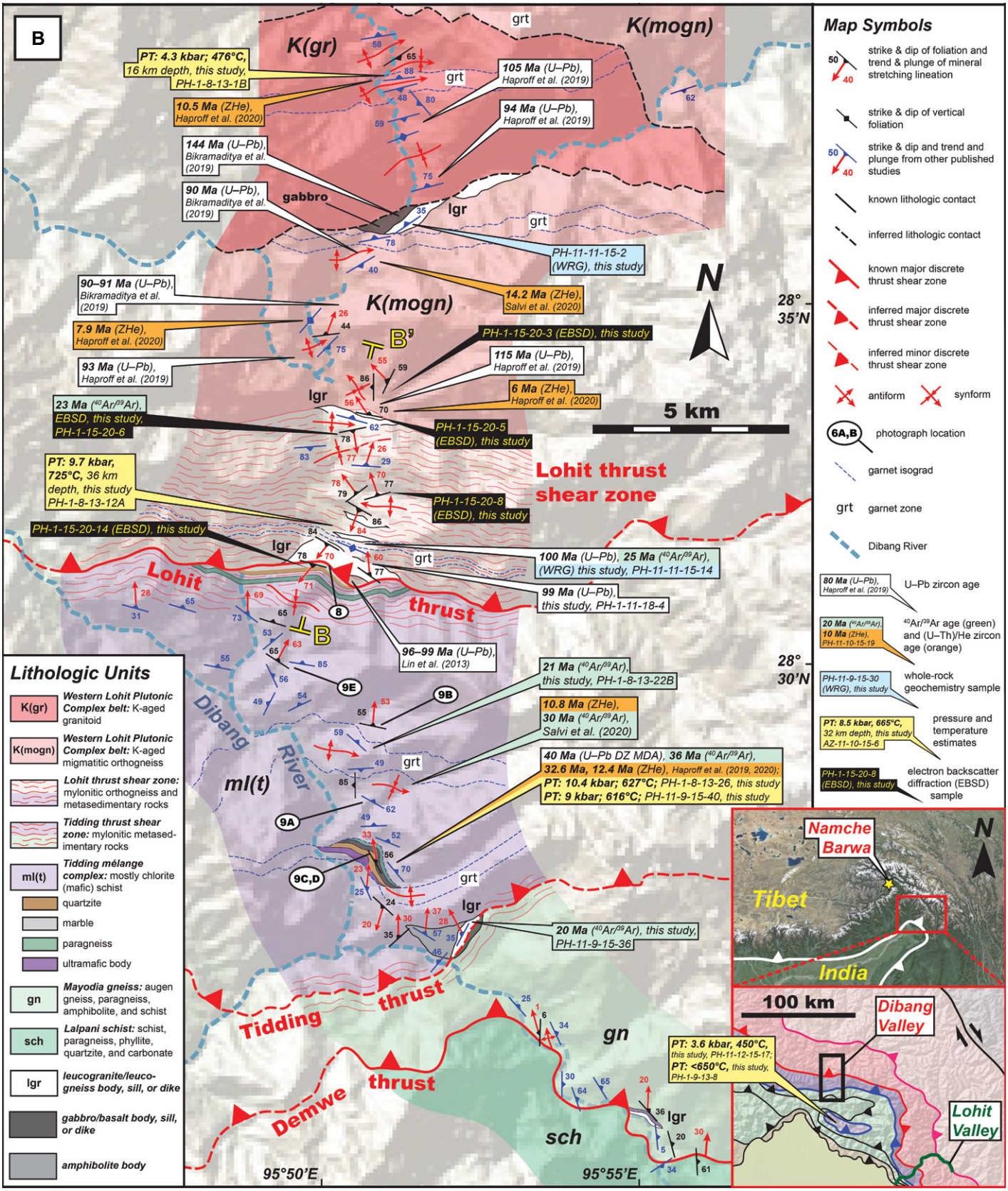

Figure 4. (Continued)

Downloaded from http://pubs.geoscienceworld.org/gsa/gsabulletin/article-pdf/doi/10.1130/B36323.1/5738725/b36323.pdf
by University of Nevada Reno user

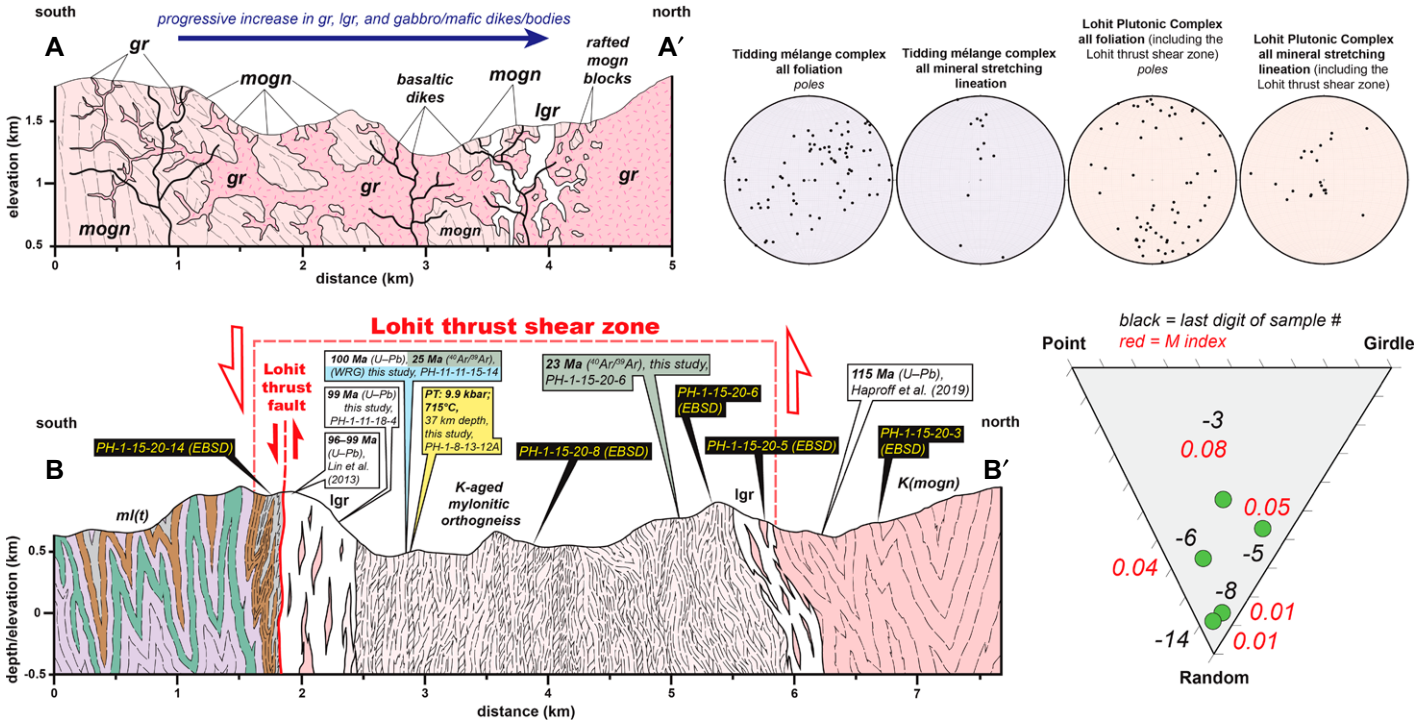

Figure 5. Schematic cross sections are shown across the contact between migmatitic orthogneiss and intermediate and felsic composition granitoids within the Eastern Lohit Plutonic Complex belt (A–A′) and the Lohit thrust shear zone (B–B′). Stereograms of foliation and mineral stretching lineation measured throughout the Tidding mélange complex and Lohit Plutonic Complex are shown in the top right. Stereograms include measurements from Haproff et al. (2018, 2019, 2020). Fabric strength results of electron backscatter diffraction (EBSD) analyses across the Lohit thrust shear zone are shown in the bottom right on a ternary diagram of Vollmer (1990). gr—granitoid; lgr—leucogranite; mogn—migmatitic orthogneiss.

et al., 2013; Haproff et al., 2019; Bikramaditya et al., 2020; Fig. 4).

The migmatitic orthogneiss unit of the Western Lohit Plutonic Complex belt is similar to that of the Eastern Lohit Plutonic Complex belt in that it contains garnet-, quartz-, and feldspar-rich felsic and pyroxene- and amphibole-rich amphibolite compositional layers (Fig. S2; see footnote 1 for all supplemental material). Layer thicknesses range from ~1 cm to ~5 m (Fig. S2). At the northern exposure of the migmatitic orthogneiss, felsic and amphibolite components are interlayered with ~1-m-wide marble bands and ~1–10-m-wide, deformed gabbro and leucogneiss (Fig. 4). Foliation-parallel compositional layers are cross-cut by ~20-cm- to ~2-m-wide leucogranite dikes. The well-developed foliation within the migmatitic orthogneiss unit is parallel to compositional layers and strikes east and northeast with dips of between ~90–30° north and northwest (Figs. 4 and 5). A well-developed mineral stretching lineation defined by rodded quartz, feldspar, mica, and amphibole trends northwest to northeast and plunges between ~80–25° (Figs. 4 and 5). Like that of the Eastern Lohit Plutonic Complex belt, migmatitic orthogneiss of the Western Lohit Plutonic Complex belt contains sub-meter-scale, foliation-parallel, and perpendicular shear bands and ~1-cm- to ~10-m-wavelength disharmonic and isoclinal folds (Fig. S2). One ~1-m-wide, north-dipping, mylonitic thrust shear zone repeats the migmatitic orthogneiss unit within its northern exposure (Fig. 4A) and contains top-to-the-south S-C fabric, asymmetric folds, and asymmetric clasts.

Four samples were collected from the migmatitic orthogneiss unit of the Western Lohit Plutonic Complex belt (Fig. 4A). Sample PH-1-14-20-9 was collected from a ~2-m-wide, quartz- and feldspar-rich leucogranite dike that cross-cuts amphibolite, located ~1 km to the south of the Walong thrust in its footwall within the northern exposure of the migmatitic orthogneiss unit (Fig. 4A). The sampled leucogranite dike strikes 185° and dips 80° west. The foliation within the cross-cut amphibolite strikes 256° and dips 63° northwest (Fig. 4A). Sample AZ-11-10-15-6 was collected from a garnet-bearing, quartz- and feldspar-rich felsic layer of migmatitic orthogneiss, located ~2 km south of sample PH-1-14-20-9 within the same unit exposure (Fig. 4A). Well-developed foliation formed by flattened felsic and mafic minerals within the sample strikes 270° and dips 29° north (Fig. 4A). Sample PH-11-11-15-2 was collected from a quartz- and feldspar-rich felsic layer of migmatitic orthogneiss located within the southern unit exposure near the northern contact with the intermediate-composition granitoid unit (Fig. 4A). The well-developed foliation within the sample strikes 236° and dips 35° northwest (Haproff et al., 2019; Fig. 4A). The southernmost sample, PH-1-15-20-3, was collected from orthogneiss directly north of the Lohit thrust shear zone. The well-developed foliation within the sample is predominantly defined by flattened quartz, muscovite, and biotite and strikes 206° and dips 59° northwest (Fig. 4A). A mineral stretching lineation predominantly defined by quartz trends 315° and plunges 55° (Fig. 4A).

The intermediate-composition granitoid unit contains a weakly developed foliation defined by flattened felsic and mafic minerals that are segregated as compositional layers. The foliation strikes east and dips ~90–50° north and south (Figs. 4B and 5). Compositional layers often form ~5-cm- to ~10-m-wavelength folds (Fig. 7A) and are cross-cut by both folded and undeformed felsic and mafic dikes (Fig. 7B). A mineral stretching lineation was not observed (Fig. 4B).

Downloaded from http://pubs.geoscienceworld.org/gsa/gsabulletin/article-pdf/doi/10.1130/B36323.1/5738725/b36323.pdf
by University of Nevada Reno user

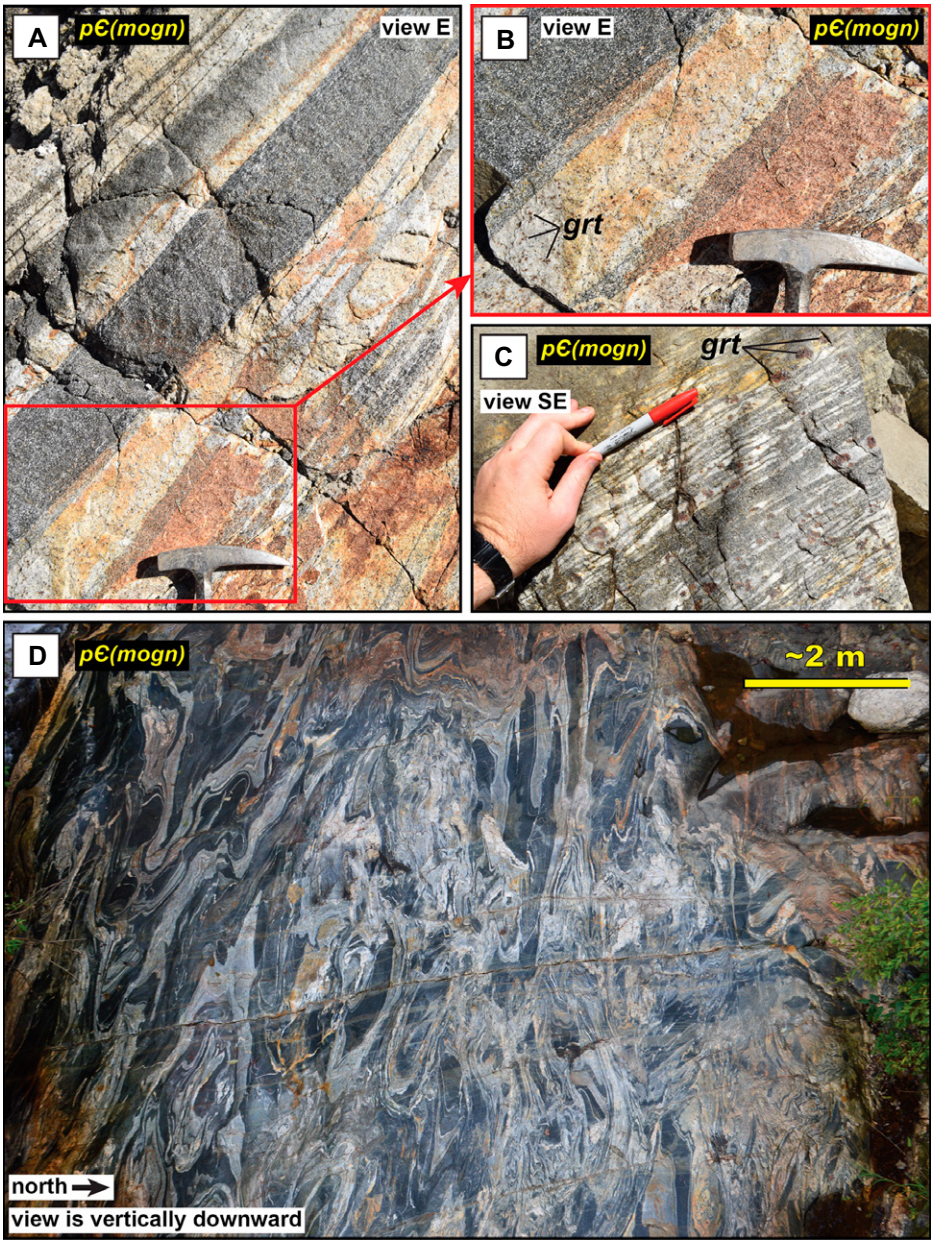

Figure 6. Field photographs of the Eastern Lohit Plutonic Complex belt including (A–C) garnet (grt) orthogneiss with interlayered mafic and felsic components, and (D) folded migmatitic orthogneiss. mogn—migmatitic orthogneiss.

Sample PH-1-8-13-1B is a monzodiorite collected ~5 km south of sample AZ-11-10-15-6 from the middle part of the Western Lohit Plutonic Complex belt (Fig. 4B). The weakly developed foliation within the sample strikes 083° and dips 88° north (Haproff et al., 2019; Fig. 4A).

Lohit Thrust Shear Zone

The most prominent structure exposed along Dibang Valley is the Lohit thrust shear zone, which is a ~5-km-wide mylonite zone that extends ~4 km north into the Western Lohit Plutonic Complex belt and ~1 km south into the Tidding mélange complex (Haproff et al., 2020) (Figs. 4B and 5). Our field observations support the interpretation of a discrete Lohit thrust fault located ~1 km above the base of the ~5-km-wide mylonite zone, where there is a sharp local change in lithology from predominantly mylonitic orthogneiss, amphibolite, and leucogneiss in the hanging wall to mylonitic marble in the footwall (Figs. 4B and 5). The surface of the discrete Lohit thrust fault within the mylonite zone is overturned and strikes 104° and dips 71° south (Fig. 8). Above the discrete Lohit thrust fault, shear zone compositional layers of mylonitic orthogneiss and amphibolite are ~1 cm to ~1 m thick (Fig. 8). Minor leucogneiss is exposed as two ~100-m-wide sections located near the northern and southern margins of the mylonite zone (Figs. 4B and 5) and several ~50-cm- to 1-m-wide leucogneiss bodies that occur parallel to mylonitic foliation within the shear zone (Fig. 4B). Metasedimentary rocks below the Lohit thrust fault consist of ~1-cm- to ~5-m-thick compositional layers of mylonitic marble, quartzite, paragneiss, amphibolite, and quartzo-feldspathic and mafic schist (Fig. S3).

The east-striking mylonitic foliation throughout the ~5-km-wide Lohit thrust shear zone is defined by flattened mafic and felsic minerals that are oriented parallel to compositional layers. The mylonitic foliation is mostly subvertical, with dips between ~90–60° north and south (Figs. 4B and 5), and commonly forms both micro- and macroscopic asymmetric and isoclinal folds with outcrop wavelengths of between ~2 cm and ~10 m (Fig. S3). The stretching lineation formed by rodded minerals throughout the shear zone is oriented down dip within the mylonitic foliation and steeply plunges ~80–60° north and south (Figs. 4B and 5). North-side-up ductile kinematic indicators observed throughout the Lohit thrust shear zone include sub-meter-scale σ and δ porphyroclasts and asymmetric boudins (~1 cm to ~10 m long and ~1 cm to ~1 m wide in outcrop), both of which are mostly defined by quartz and feldspar, and S-C fabric (Figs. 8, S3, and S4). S-C fabric zones in outcrop are ~2 cm to ~5 m wide and formed by ~1-cm- to ~1-m-thick layers of flattened quartz, feldspar, mica, calcite, and amphibole (Figs. 8, S3, and S4).

Seven samples were collected across the width of the Lohit thrust shear zone (Figs. 4B and 5). The northernmost samples, PH-1-15-20-5 and PH-1-15-20-6, are mylonitic orthogneisses that were collected ~1 km apart. The mylonitic foliation within sample PH-1-15-20-5 strikes 281° and dips 70° north. The mineral stretching lineation within the same sample trends 326° and plunges 56°. The mylonitic foliation within sample PH-1-15-20-6 strikes 79° and dips 78° south (Figs. 4B and 5). The mineral stretching lineation within the same sample trends 171° and plunges 77° (Fig. 4B). Sample PH-1-15-20-8 is a mylonitic orthogneiss collected from the middle portion of the shear zone. The mylonitic foliation within the sample strikes 254° and dips 77° north (Figs. 4B and 5). The mineral stretching lineation trends 341° and plunges 70° (Fig. 4B). Samples PH-1-8-13-12A and PH-11-11-15-14 are mylonitic orthogneisses collected <1 km apart along strike

Downloaded from http://pubs.geoscienceworld.org/gsa/gsabulletin/article-pdf/doi/10.1130/B36323.1/5738725/b36323.pdf
by University of Nevada Reno user

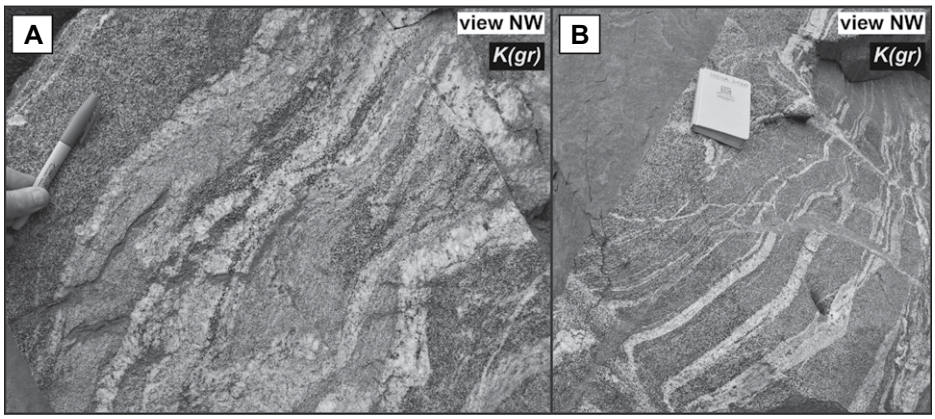

Figure 7. Field photographs of the Western Lohit Plutonic Complex belt include (A) interlayered felsic and mafic components and (B) cross-cutting dikes within dioritic granitoids. gr—granitoid.

within the southern-central portion of the shear zone. The mylonitic foliation within sample PH-1-8-13-12A strikes 316° and dips 85° southwest (Figs. 4B and 5). Sample PH-1-11-18-4 is a mylonitic leucogneiss collected from the southernmost section of the Western Lohit Plutonic Complex belt within the Lohit thrust shear zone, directly above the discrete thrust contact with the Tidding mélange complex. The mylonitic foliation within the sample strikes 82° and dips 72° south (Figs. 4B and 5). The southernmost sample, PH-1-15-20-14, is a mylonitic marble collected from the northernmost section of the Tidding mélange complex within the Lohit thrust shear zone. The mylonitic foliation within the sample strikes 105° and dips 78° south (Figs. 4B and 5). The mineral stretching lineation trends 220° and plunges 71° (Fig. 4B).

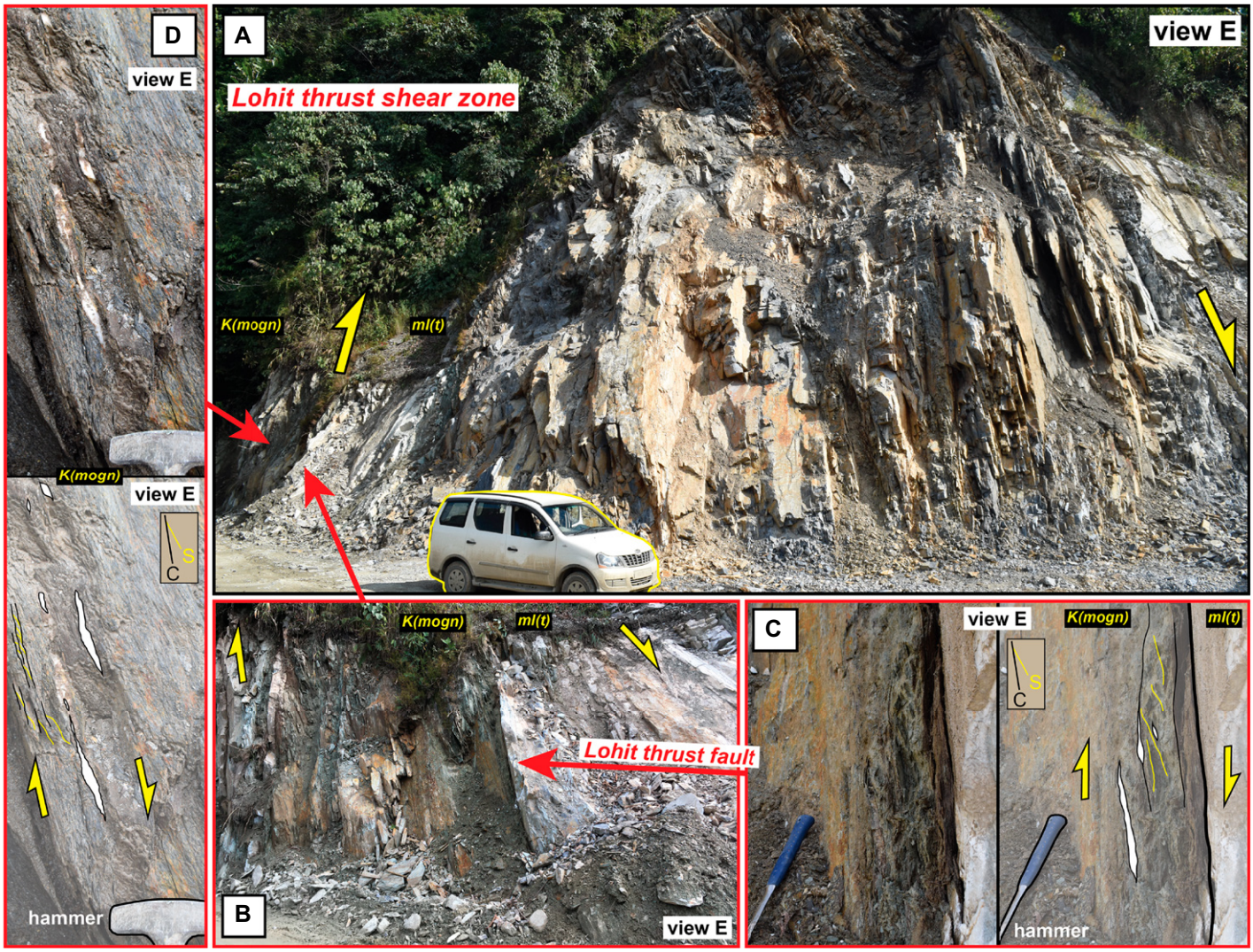

Figure 8. Field photographs show (A) the subvertical, southernmost section of the Lohit thrust shear zone, (B–C) the Lohit thrust fault, (C) subvertical, and (D) overturned, north-side-up S-C fabric and asymmetric quartz boudins.

Downloaded from http://pubs.geoscienceworld.org/gsa/gsabulletin/article-pdf/doi/10.1130/B36323.1/5738725/b36323.pdf
by University of Nevada Reno user

Tidding Mélange Complex

The Tidding mélange complex is the southernmost lithotectonic unit mapped along Dibang Valley and consists of ~1-cm- to >10-m-thick compositional layers of quartzite, marble, paragneiss, amphibolite, gabbro, ultramafic bodies, garnet biotite schist, and chlorite schist (Figs. 4B, 5, and 9). Maximum thicknesses of compositional layers increase southwards from ~1 cm in the Lohit thrust shear zone to >10 m in the interior of the Tidding mélange complex (Figs. 9 and S3). A well-developed foliation is defined by flattened mica, amphibole, quartz, and feldspar and oriented parallel to compositional layers. The foliation strikes southeast to northeast (Figs. 4B and 5) and is parallel to mylonitic foliation within the Lohit thrust shear zone above and Tidding thrust shear zone below (Fig. 4B). A mineral stretching lineation within the foliation trends north and plunges ~60–20° (Fig. 4B). East-trending and south-vergent, asymmetric folds are pervasive at both macro- and microscopic scales and often have isoclinal limbs (Fig. 9). Outcrop wavelengths are between ~2 cm to ~25 m (Fig. 9).

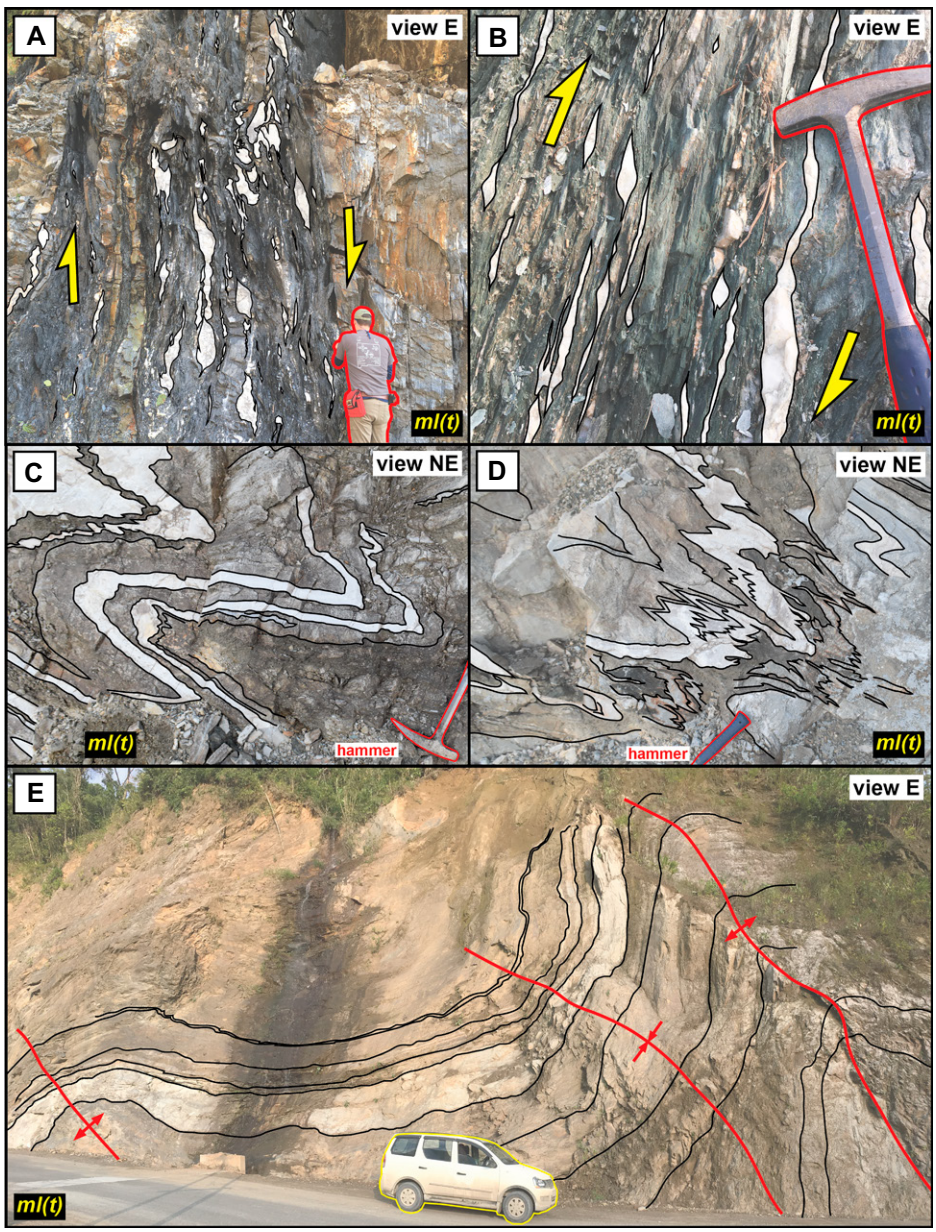

Figure 9. Field photographs of the Tidding mélange complex include (A) overturned, north-side-up, and (B) top-to-the-south asymmetric quartz and feldspar boudins, asymmetric clasts, and isoclinal folds within schist and quartzite, (C–D) sub-meter–wavelength folds in quartzite and schist, and (E) decameter-wavelength folds.

Four samples were collected from the metasedimentary portions of the Tidding mélange complex (Fig. 4B). Garnet schist sample PH-1-8-13-22B, collected from the middle portion of the mélange complex, contains a foliation predominantly defined by flattened muscovite, biotite, and quartz that strikes 312° and dips 59° northeast (Haproff et al., 2019; Fig. 4B). Garnet schist samples PH-11-9-15-40 and PH-1-8-13-26 were collected within ~50 m of each other from the middle section of the Tidding mélange complex. The foliation within the samples is defined by biotite, muscovite, quartz, and feldspar and strikes 274–307° and dips 25–32° northeast (Fig. 4B). A mineral stretching lineation within both samples trends 007–354° and plunges 23–25° (Fig. 4B). Gneiss sample PH-11-9-15-36 was collected from the lowermost section of the mélange complex adjacent to the Tidding thrust shear zone. The foliation within the sample is predominantly defined by quartz and feldspar and strikes 209° and dips 35° northwest (Fig. 4B). A mineral stretching lineation within the sample trends 332° and plunges 28° (Fig. 4B). Two samples of garnet chlorite schist (PH-1-9-13-8 and PH-11-12-15-17) were sampled from sedimentary matrix portions of the Mayodia mélange complex, located south of the Tidding mélange complex. Sample PH-1-9-13-8, located <1 km from the Tidding thrust, contains a well-developed foliation defined by flattened chlorite and quartz that strikes 312° and dips 25° southwest (Haproff et al., 2019; Fig. 4B). Sample PH-11-12-15-17, collected <100 m from sample PH-1-9-13-8, contains a well-developed foliation defined by flattened chlorite, muscovite, quartz, and feldspar that strikes 114° and dips 54° southwest (Haproff et al., 2019) (Fig. 4B).

Tidding Thrust Shear Zone

The northernmost exposure of the Tidding thrust shear zone was identified as a ~1-km-wide, north-dipping mylonite zone that extends across the contact between the Tidding mélange complex in the hanging wall and the Mayodia gneiss in the footwall (Gururajan and Choudhuri, 2003; Haproff et al., 2020; Fig. 4B). Our field observations support a discrete Tidding thrust fault in the middle section of the shear zone, where a ~50-m-thick, north-dipping (~30°N) zone of more intense ductile strain locally separates chlorite schist and minor amphibolite and leucogneiss in the hanging wall from quartzo-feldspathic schist and paragneiss in the footwall (Fig. 4B). Compositional layers parallel to mylonitic foliation decrease in thickness from >10 m in both the Tidding mélange

Downloaded from http://pubs.geoscienceworld.org/gsa/gsabulletin/article-pdf/doi/10.1130/B36323.1/5738725/b36323.pdf
by University of Nevada Reno user

TABLE 1. SUMMARY OF U–Pb ZIRCON GEOCHRONOLOGIC AGES OF THE LOHIT PLUTONIC COMPLEX

Sample	Rock type	Location		Elevation (m)	Weighted mean $^{206}Pb/^{238}U$ age	MSWD	n
		Latitude (°N)	Longitude (°E)				
PH-1-11-18-4	mylonitic leucogneiss	28 31.597	95 50.358	810	99 ± 0.2	1.5	97
PH-11-11-15-14	mylonitic orthogneiss	28 31.871	95 50.660	798	100.1 ± 0.1	6.3	34
PH-1-14-20-9	leucogranite	28 40.822	95 51.384	1208	81.8 ± 0.1	4.8	86

Note: MSWD—mean square of weighted deviates.

complex and Mayodia gneiss to ~1 cm within the Tidding thrust shear zone near the location of the fault. The shear zone stretching lineation is defined by rodded quartz, feldspar, amphibole, and mica and shallowly plunges ~30° down dip to the north (Haproff et al., 2020; Fig. 4B). Top-to-the-south ductile kinematic indicators within the shear zone include sub-meter-scale σ and δ porphyroclasts, asymmetric boudins (~1 cm to ~1 m long and ~1–50 cm wide in outcrop), and ~1-cm- to ~1-m-wide S-C fabric zones.

ANALYTICAL METHODS

U–Pb Zircon Geochronology

We analyzed zircon grains from two leucogneiss samples and one leucogranite sample of the Western Lohit Plutonic Complex belt (Fig. 4; Table 1) to determine U–Pb crystallization ages and test whether the rocks were emplaced during periods of Cenozoic crustal thickening. Zircon grains from whole-rock samples were separated at ZirChron, L.L.C., in Tucson, Arizona, using standard procedures (Quidelleur et al., 1997), mounted on 1-in-diameter epoxy pucks and polished with carbide paper. Cathodoluminescence images of grains were collected using a JEOL JSM-6510LV scanning electron microscope at the Southeastern North Carolina Regional Microanalytical and Imaging Consortium, Fayetteville State University in Fayetteville, North Carolina, USA. Zircon grains from the samples are euhedral, prismatic crystals with long axes of ~50–500 μm (Fig. S5). Most grains display oscillatory zoning (Fig. S5). Zircon grains were analyzed via laser ablation–inductively coupled plasma–mass spectrometry (LA-ICP-MS) using a Thermo Element 2 instrument at the UTChron Facility, University of Texas at Austin, Austin, Texas, USA. Between 44 and 109 zircon grains were analyzed from each sample (Table S1). Rims of zircon grains were targeted for ~30-μm-diameter shots. GJ-1 zircon (608.5 Ma age; Jackson et al., 2004) was the primary standard, and 91500 (ca. 1065 Ma age; Wiedenbeck et al., 1995) and Plešovice (ca. 337 Ma age, Sláma et al., 2008) were secondary standards. Data reduction was completed with Iolite version 3.4 (Paton et al., 2010) and VizualAge (Petrus and Kamber, 2012). We report $^{206}Pb/^{238}U$ dates with <10% 2σ error given that the dates of all analyses are younger than 850 Ma and include $^{206}Pb/^{238}U$ dates with <30% discordance ($^{206}Pb/^{238}U$ versus $^{207}Pb/^{235}U$). For the three granitoid samples, we used the online program IsoplotR (Vermeesch, 2018) and the common lead correction of Stacey and Kramers (1975) to calculate the weighted means of concordant $^{206}Pb/^{238}U$ ages (Table 1) and generate Concordia diagrams.

Geochemistry

Whole-rock and trace-element geochemical analyses were performed on five samples collected from the Cretaceous portions of the Western and Eastern Lohit Plutonic Complex belts (Fig. 4; Table S2) to constrain their bulk composition, melt source, and tectonic setting of generation. Whole-rock samples were crushed and powdered at University of California, Los Angeles (UCLA), Los Angeles, California, USA, and sent to Activation Laboratories, Ltd., in Ontario, Canada, where they were placed in Teflon bombs, fused with lithium metaborate/tetraborate, and digested with HNO_3. Concentrations of major and minor oxides and trace elements were determined via ICP-MS.

$^{40}Ar/^{39}Ar$ Thermochronology

We performed $^{40}Ar/^{39}Ar$ thermochronology on muscovite and biotite grains from three samples of the Lohit Plutonic Complex and two samples of the Tidding mélange complex (Figs. 4 and 5; Table 2) to constrain the timing of cooling through biotite and muscovite closure temperature ranges of ~300–400 °C and ~350–500 °C, respectively (Harrison et al., 1985; Hames and Bowring, 1994; Grove and Harrison, 1996; Harrison et al., 2009). Muscovite and biotite separation and $^{40}Ar/^{39}Ar$ analyses were performed at the Nevada Isotope Geochronology Lab, University of Nevada, Las Vegas, Nevada, USA. Detailed $^{40}Ar/^{39}Ar$ analytical procedures are described in the Supplemental Material and Table S3. Multi-diffusion domain (MDD) modeling of K-feldspar grains from Western Lohit Plutonic Complex belt sample PH-11-11-15-14 was performed at the New Mexico Institute of Mining and Technology in Socorro, New Mexico, USA, to determine the time-temperature path of the sample. K-feldspar grains were step-heated in a temperature-controlled furnace. A Thermo Scientific Helix MC Plus multi-collector–mass spectrometer was used to analyze Ar isotopes. Detailed analytical procedures of the MDD modeling are included in the Supplemental Material and listed in Tables S4 and S5.

Geothermobarometry

Mineral composition geothermobarometric analyses were performed on three samples of the Western Lohit Plutonic Complex belt and four samples of the Tidding and Mayodia mélange complexes (Fig. 4; Table 3) to determine their pressure–temperature (*P–T*) conditions. Whole-rock samples were cut into standard 24 × 46 mm petrographic thin sections and polished. Thin sections were imaged using a petrographic microscope and scanning electron microscope at UCLA to target mineral phases that are not separated by reaction zones and were observed to be in textural equilibrium (e.g., no breakdown or overprinting mineral phases). Selected phases were shot with

TABLE 2. SUMMARY OF $^{40}Ar/^{39}Ar$ THERMOCHRONOLOGIC AGES OF THE LOHIT PLUTONIC COMPLEX AND TIDDING-MAYODIA MÉLANGE COMPLEX

Sample	Rock type (mineral)	Location		Elevation (m)	Calculated age (Ma)	MSWD
		Latitude (°N)	Longitude (°E)			
Lohit Plutonic Complex						
PH-11-10-15-19	migmatitic orthogneiss (muscovite)	28 48.880	95 55.286	1618	24.1 ± 0.1	0.2
PH-1-15-20-6	mylonitic orthogneiss (muscovite)	28 33.169	95 50.530	771	22.8 ± 0.4	42.4
PH-11-11-15-14*	mylonitic orthogneiss (K-feldspar)	28 31.871	95 50.660	798	25–10	N/A
Tidding-Mayodia mélange complex						
PH-1-8-13-22B	garnet schist (biotite)	28 29.086	95 50.632	775	20.6 ± 0.1	13.5
PH-11-9-15-36	gneiss (muscovite)	28 26.186	95 52.226	558	19.9 ± 0.1	5.5

*Sample PH-11-11-15-14 was analyzed via the multi-diffusion domain method; MSWD—mean square of weighted deviates.

Downloaded from http://pubs.geoscienceworld.org/gsa/gsabulletin/article-pdf/doi/10.1130/B36323.1/5738725/b36323.pdf
by University of Nevada Reno user

TABLE 3. SUMMARY OF PRESSURE–TEMPERATURE ESTIMATES FOR THE TIDDING-MAYODIA MÉLANGE COMPLEX AND LOHIT PLUTONIC COMPLEX

Sample and lithology	Technique	T (°C)	P (kbar)	Cor*	Depth (km)†	Location	
						Latitude (°N)	Longitude (°E)
Tidding-Mayodia mélange complex							
PH-1-8-13-26 (garnet schist)	THERMOCALC 3.37	627 ± 28	10.4 ± 1.1	0.841	39	28 26.897	95 50.957
PH-11-9-15-40 (garnet schist)	THERMOCALC 3.37	616 ± 11	9 ± 0.5	0.604	34	28 26.903	95 50.959
PH-11-12-15-17 (garnet chlorite schist)	THERMOCALC 3.37	450 ± 50	3.6 ± 1.1	0.957	13	28 16.926	95 55.229
Lohit Plutonic Complex							
AZ-11-10-15-6 (migmatitic orthogneiss)	THERMOCALC 3.37	665 ± 153	8.5 ± 3.6	3.2	32	28 38.493	95 51.299
PH-1-8-13-12A (mylonitic orthogneiss)	amphibole-plagioclase§	725 ± 58	–	–	–	28 32.162	95 50.656
	Al-in-hornblende#	–	9.7 ± 0.8	–	36	28 32.162	95 50.656
PH-1-8-13-1B (monzodiorite)	amphibole-plagioclase	476 ± 42	–	–	–	28 37.975	95 51.138
	Al-in-hornblende	–	4.3 ± 0.9	–	16	28 37.975	95 51.138

Note: Dashes indicate immeasurable values.
*Correlation coefficient used by THERMOCALC 3.37 (Holland and Powell, 1998).
†Depth estimates assume a constant lithostatic gradient and average crustal density of 2.7 g/cm^3.
§Amphibole-plagioclase geothermometry calibration of Holland and Blundy (1994).
#Al-in-hornblende geobarometry calibration of Anderson and Smith (1995).

a 15 nA electron beam of 10 μm size using a JEOL 8200 microprobe at UCLA. Element maps of selected garnet grains were generated using energy-dispersive X-ray spectroscopy on the electron microprobe to document chemical zonation related to metamorphism. Oxide weight percentages and activity coefficients were calculated using the program AX and input into the average *P–T* mode of the THERMOCALC 3.37 program (Holland and Powell, 1998). Intersections of equilibria reactions in *P–T* space were determined based on the internally consistent data set of Holland and Powell (1998). THERMOCALC *P–T* determinations involve the following sources of uncertainty: precision of individual microprobe spot analyses, compositional variability of analyzed mineral phases, mineral activities, and the chosen thermodynamic data set (e.g., Holland and Powell, 1998). Microprobe analyses were all conducted using the same instrument under identical run conditions, which limited inter-sample variability of the spot analyses. For hornblende-bearing granitoid samples of the Western Lohit Plutonic Complex belt, *P–T* conditions were determined by using the Al-in-hornblende geobarometry calibration of Anderson and Smith (1995) and amphibole-plagioclase geothermometry calibration of Holland and Blundy (1994). Reported *P–T* conditions from Al-in-hornblende geobarometry and amphibole-plagioclase geothermometry are the means and two standard deviations of the spread of results for each sample. Pressure-based depth estimates assume a constant lithostatic gradient and average crustal density of 2.7 g/cm^3.

Microstructural Observations and EBSD Analyses

We performed petrographic and EBSD analyses of quartz grains in four samples and calcite grains in one sample across the Lohit thrust shear zone (Figs. 4B and 5; Table 4) to examine crystallographic preferred orientations (CPOs) related to deformation conditions and kinematics (e.g., Schmid and Casey, 1986; Law et al., 1990; Kruhl, 1996; Stipp et al., 2002; Law et al., 2004; Zibra et al., 2020). EBSD analyses were conducted using a Nordlys Nano high-resolution detector on a JEOL 7100 FE scanning electron microscope at the Mackay Microbeam Laboratory, University of Nevada, Reno, Nevada. Post-processing was completed using AZtecHKL software and MTEX v. 5.1.1 (Bachmann et al., 2011). Grain sizes were calculated using the methods of Cross et al. (2017), which determines recrystallized versus relict grains depending on the range of intragranular misorientations. Pole figures were plotted on lower hemisphere stereograms in sample reference frame and shown as orientation distribution functions (ODFs) (Wenk and Wilde, 1972; Ismaïl and Mainprice, 1998) of one-point-per grain analyses. Quartz misorientation axes with angles of between 5° and 10° were plotted and contoured on inverse pole figures with 10° halfwidth, following the approach of Piette-Lauzière et al. (2020) for recrystallized and relict grains. Interpretations of the misorientation axes in terms of active slip systems were guided by the methods of Neumann (2000). We calculated the relative strength and shape of the CPOs in MTEX, including *K* and *M* indices (Mainprice et al., 2015), and point (*P*), girdle (*G*), cylindricity ($B = P + G$), and random (*R*) indices (Vollmer, 1990). Eigenvalue analysis determined the shape parameter *K* (Woodcock, 1977) (Fig. 5; Table 4). Lastly, we determined the crystal kinematic vorticity axis (CVA) for each sample using the grain-scale crystallographic orientation dispersion methods and code of Michels et al. (2015). Additional details of sample preparation and analytical methods are presented in the Supplemental Materials.

TABLE 4. SUMMARY OF MICROSTRUCTURAL OBSERVATIONS AND ELECTRON BACKSCATTER DIFFRACTION (EBSD) ANALYTICAL RESULTS

Sample	Lithology (analyzed phase)*	Step (μm)	*M index*	*P*	*G*	*R*	B	*K linear*	Recrystallized grainsize (μm)†	Flow stress (MPa)	Location	
											Latitude (°N)	Longitude (°E)
PH-1-15-20-3	orthogneiss (qtz)	4.90	0.08	0.27	0.27	0.46	0.54	1.05	70 ± 42	31	28 33.837	95 50.920
PH-1-15-20-5	mylonitic orthogneiss (qtz)	9.80	0.05	0.22	0.11	0.67	0.33	3.26	94 ± 60	26	28 33.500	95 50.671
PH-1-15-20-6	mylonitic orthogneiss (qtz)	5.90	0.04	0.09	0.34	0.57	0.43	0.27	89 ± 47	27	28 33.169	95 50.530
PH-1-15-20-8	mylonitic orthogneiss (qtz)	5.90	0.01	0.06	0.09	0.86	0.15	1.02	67.2 ± 42	32	28 32.329	95 50.877
PH-1-15-20-14	mylonitic marble (qtz)	11.75	0.01	0.07	0.05	0.88	0.12	2.58	134 ± 56	21	28 30.347	94 24.422
PH-1-15-20-14	mylonitic marble (clc)	11.75	0.07	0.28	0.12	0.60	0.40	3.80	66 ± 31	17	28 30.347	94 24.422

Notes: Fabric stretch and shape indices: Misorientation (M) (Skemer et al., 2005); K (Woodcock, 1977); Point (P), Girdle (G), and Random (R) (Vollmer, 1990); Cylindricity (B = P + G) (Vollmer, 1990).
*Quartz (qtz) and calcite (clc) parameters for sample PH-1-15-20-14.
†Calculated using Cross et al. (2017) MTEX code.

Downloaded from http://pubs.geoscienceworld.org/gsa/gsabulletin/article-pdf/doi/10.1130/B36323.1/5738725/b36323.pdf
by University of Nevada Reno user

ANALYTICAL RESULTS

U–Pb Zircon Geochronology

The three samples of the Western Lohit Plutonic Complex belt yield Cretaceous U–Pb zircon crystallization ages clustered at ca. 82 Ma and ca. 100–99 Ma (Fig. 10; Table 1). Mylonitic leucogneiss sample PH-1-11-18-4 yields a weighted mean U–Pb zircon age of 99 ± 0.2 Ma from 97 grains (MSWD = 1.5) (Fig. 10A). Mylonitic orthogneiss sample PH-11-11-15-14 yields a similar weighted mean U–Pb zircon age of 100.1 ± 0.1 Ma from 34 grains (MSWD = 6.33) (Fig. 10B). Leucogranite sample PH-1-14-20-9 yields a weighted mean U–Pb zircon age of 81.8 ± 0.1 Ma from 86 grains (MSWD = 4.8) (Fig. 10C). Complete isotopic data of all U–Pb zircon analyses are shown in Table S1.

Geochemistry

The five samples collected from the Cretaceous portions of the Western and Eastern Lohit Plutonic Complex belts plot within the diorite, granodiorite, and granite fields of the total alkali versus silica diagram (Fig. S6; Table S2). All samples are peraluminous with high values of Al_2O_3 (>14 wt%), $Al_2O_3/(CaO + Na_2O + K_2O)$ (>1.5), and $Al_2O_3/(Na_2O + K_2O)$ (>2.2) (Fig. S7A). Trace-element concentrations are consistent with generation in a volcanic arc setting (Pearce et al., 1984; Fig. S7B). All samples fall within the non-A–type granitoid field (Fig. S7C).

$^{40}Ar/^{39}Ar$ Thermochronology

Garnet schist sample PH-1-8-13-22B of the Tidding mélange complex contains a well-developed foliation defined by biotite and muscovite grains and recrystallized quartz and plagioclase grains (Fig. S8). The foliation wraps around small, <1-mm-wide, euhedral garnet porphyroblasts. Quartz grains display undulose extinction and lobate and interfingering boundaries indicative of dynamic recrystallization via grain boundary migration (GBM) at temperatures of ~550–650 °C (e.g., Law, 2014). $^{40}Ar/^{39}Ar$ thermochronology of biotite yields a generally downward-stepping age spectrum over the final ~80% of released ^{39}Ar (nine steps), which corresponds to a weighted mean age of 20.6 ± 0.1 Ma (Fig. 11A; Tables 2 and S3). The initial old apparent ages are likely caused by excess Ar contamination, which is common for biotite in Himalayan samples (e.g., Stübner et al., 2017), including some samples from Dibang Valley (Salvi et al., 2020). Despite the effects of excess Ar in the sample, the weighted mean age of the nine steps is comparable to other biotite, muscovite, and K-feldspar $^{40}Ar/^{39}Ar$ ages from this study (see below) and Salvi et al. (2020).

Gneiss sample PH-11-9-15-36 of the Tidding mélange complex contains a well-developed foliation defined by biotite and muscovite grains and recrystallized quartz, plagioclase, and K-feldspar grains (Fig. S9). Quartz grains display textures indicative of GBM recrystallization at ~550–650 °C (e.g., Law, 2014). $^{40}Ar/^{39}Ar$ thermochronology of muscovite yields a relatively flat age spectrum comprising ~90% of released ^{39}Ar (seven steps), which corresponds to a weighted mean age of 19.9 ± 0.1 Ma (Fig. 11B; Tables 2 and S3).

Migmatitic orthogneiss sample PH-11-10-15-19 of the Eastern Lohit Plutonic Complex belt contains a well-developed foliation predominantly defined by muscovite- and amphibole-rich layers and recrystallized quartz-, plagioclase, and K-feldspar-rich layers. $^{40}Ar/^{39}Ar$ thermochronology of muscovite yields a flat age spectrum comprising >90% of released ^{39}Ar (eight steps), which corresponds to a weighted mean age of 24.1 ± 0.1 Ma (Fig. 11C; Table 2).

Mylonitic orthogneiss sample PH-1-15-20-6 of the Lohit thrust shear zone contains a well-developed mylonitic foliation predominantly defined by quartz- and plagioclase-rich layers and muscovite- and chlorite-rich layers that contain minor amphibole and epidote grains (Fig. S10). Quartz grains display undulose extinction and lobate and interfingering boundaries indicative of GBM at ~550–650 °C (e.g., Law, 2014). $^{40}Ar/^{39}Ar$ thermochronology of muscovite yields an age spectrum with an overall climbing pattern (Fig. 11D). The apparent ages begin at ca. 12 Ma and steadily climb toward over ~30% of ^{39}Ar released toward a somewhat flat segment at ca. 23 Ma spanning ~70% of released ^{39}Ar. The flat steps yield a mean $^{40}Ar/^{39}Ar$ age of 22.8 ± 0.4 Ma. (Fig. 11D; Tables 2 and S3). The age spectra may reflect cooling of differently sized domains within the muscovite grain (Harrison et al., 2009; Harrison and Lovera, 2014), with rapid cooling at ca. 23 Ma recorded by the larger-sized, higher-temperature domains followed by slower cooling recorded by smaller-sized, lower-temperature domains until ca. 12 Ma. Additional MDD modeling could better resolve this protracted cooling history (e.g., Zuza et al., 2021).

Mylonitic orthogneiss sample PH-11-11-15-14 of the Lohit thrust shear zone contains a well-developed mylonitic foliation that is predominantly defined by muscovite- and chlorite-rich layers and recrystallized quartz-, plagioclase-, and K-feldspar-rich layers that contain minor epidote, sphene, and <1-mm-diameter garnet grains (Fig. S11). MDD $^{40}Ar/^{39}Ar$ thermochronology

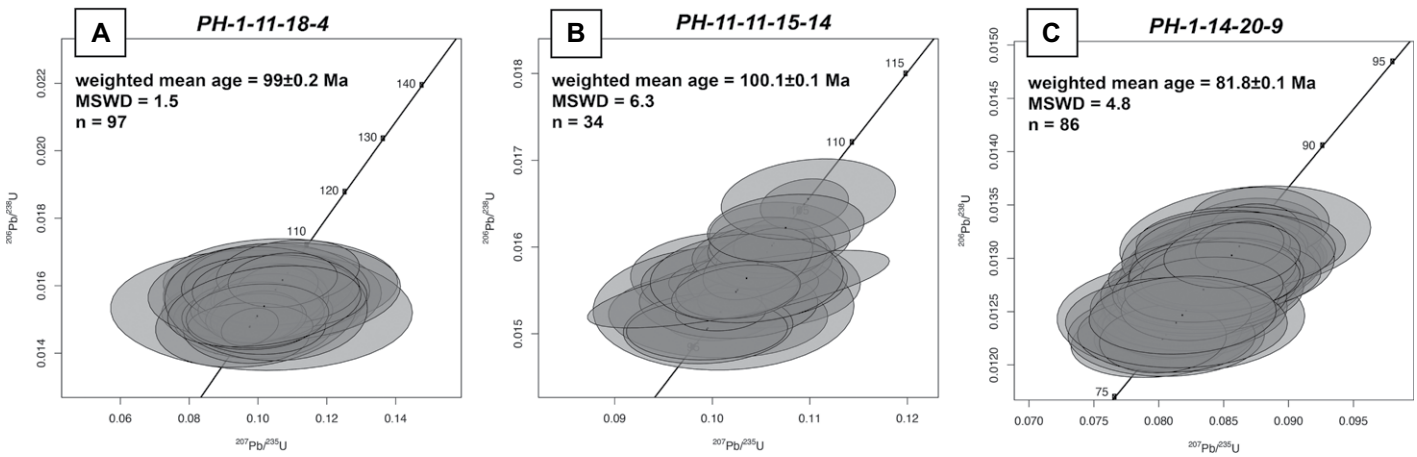

Figure 10. Concordia diagrams and weighted mean ages of U–Pb zircon geochronologic results are shown for samples (A) PH-1-11-18-4, (B) PH-11-11-15-14, and (C) PH-1-14-20-9.

Downloaded from http://pubs.geoscienceworld.org/gsa/gsabulletin/article-pdf/doi/10.1130/B36323.1/5738725/b36323.pdf
by University of Nevada Reno user

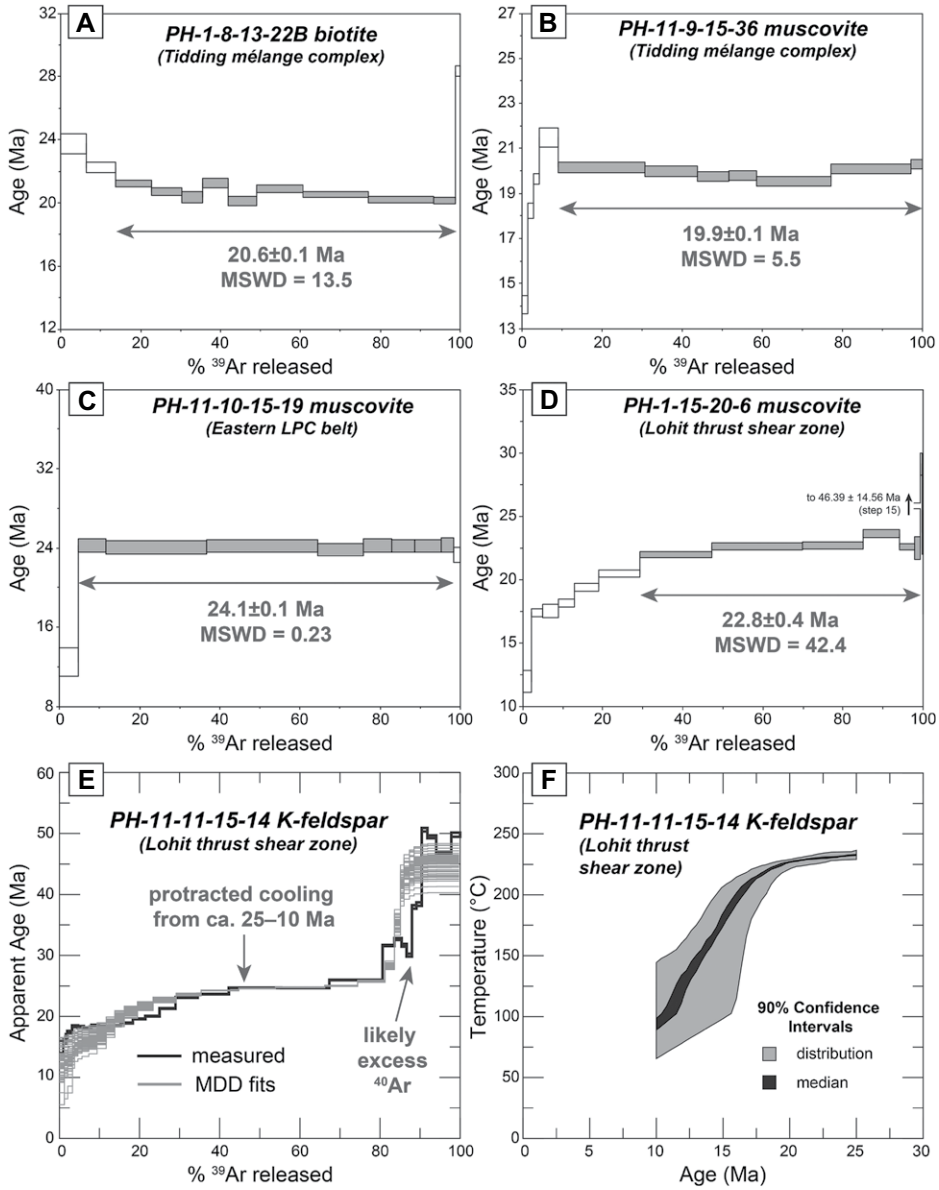

Figure 11. $^{40}Ar/^{39}Ar$ thermochronologic age plots for samples (A) PH-1-8-13-22B, (B) PH-11-9-15-36, (C) PH-11-10-15-19, (D) PH-1-15-20-6, and (E–F) PH-11-11-15-14.

results of K-feldspar have initial ages of ca. 10 Ma that climb to ca. 25 Ma near the middle of the spectrum before sharply climbing to ca. 50 Ma over the final ~20% of the spectrum (Figs. 11E and 11F). The sample has a generally low K/Ca that likely indicates plagioclase mixed with the K-feldspar, and it is possible that the sharp rise in age for the higher temperature heating steps reflects excess Ar exsolved from the plagioclase. The MDD modeling supports protracted cooling from roughly 25 Ma with temperatures of ~250 °C that decreased to ~125 °C by 12–10 Ma. This cooling history corresponds to ~80% of the spectrum, and the older ages may reflect larger-sized domains (Harrison et al., 2009; Harrison and Lovera, 2014) that record cooling in the ~300–250 °C range from ca. 50 Ma to 25 Ma. Additional MDD analytical details are shown in Figure S12.

Geothermobarometry

Monzodiorite sample PH-1-8-13-1B of the Western Lohit Plutonic Complex belt contains garnet, plagioclase, K-feldspar, amphibole, quartz, biotite, muscovite, pyroxene, and titanite (Fig. S13). Biotite, muscovite, and quartz define the weak foliation and occur both as inclusions and along the boundaries of larger plagioclase, K-feldspar, amphibole, pyroxene, and garnet grains. Large adjacent and interlocking plagioclase and amphibole grains were targeted for microprobe analyses. Use of Al-in-hornblende geobarometry (Anderson and Smith, 1995) and amphibole-plagioclase geothermometry (Holland and Blundy, 1994) yield *P–T* conditions of 4.3 ± 0.9 kbar (= ~16 km depth) and 476 ± 42 °C (Fig. 12; Table 3).

Mylonitic orthogneiss sample PH-1-8-13-12A of the Lohit thrust shear zone contains amphibole, plagioclase, K-feldspar, quartz, and titanite (Fig. S14). The well-developed mylonitic foliation is defined by fine-grained, recrystallized quartz grains and large, elongated plagioclase, amphibole, quartz, and K-feldspar grains. Large plagioclase and K-feldspar grains contain quartz and titanite inclusions. Large quartz grains display undulose extinction that is indicative of high-temperature deformation. Adjacent and interlocking plagioclase and amphibole grains were targeted for microprobe analyses. Use of Al-in-hornblende geobarometry (Anderson and Smith, 1995) and amphibole-plagioclase geothermometry (Holland and Blundy, 1994) yield *P–T* conditions of 9.7 ± 0.8 kbar (= ~36 km depth) and 725 ± 58 °C (Fig. 12; Table 3).

Migmatitic orthogneiss sample AZ-11-10-15-6 of the Western Lohit Plutonic Complex belt contains garnet, plagioclase, amphibole, clinozoesite, quartz, rutile, and ilmenite (Fig. S15). Poikiloblastic garnet grains are ~1–3 mm in diameter and contain quartz and clinozoesite inclusions. Clinozoisite, plagioclase, and quartz grains occur along the boundaries of larger amphibole grains. We targeted adjacent garnet, amphibole, and plagioclase grains and clinozoisite inclusions near garnet rims for microprobe analyses. Use of THERMOCALC 3.37 (Holland and Powell, 1998) yields *P–T* conditions of 8.5 ± 3.6 kbar (= ~32 km depth) and 665 ± 153 °C (Fig. 12; Table 3). The garnet grains analyzed are Fe-rich almandines with diffusion zoning defined by increasing Fe and decreasing Ca from rim to core (Fig. S16). The garnet composition used in the *P–T* calculation is an average of individual rim analyses that yield a similar Fe-rich almandine composition ($X_{Mg} = 0.21$). The higher uncertainties of the *P–T* conditions for this sample may be a result of the precision of individual microprobe spot analyses, compositional variability of the mineral phases analyzed, and mineral activities.

Garnet schist sample PH-1-8-13-26 of the Tidding mélange complex contains garnet, plagioclase, biotite, muscovite, quartz, amphibole, and ilmenite (Fig. S17). The well-developed foliation is predominantly defined by muscovite- and biotite-rich layers and recrystallized quartz- and plagioclase-rich layers. Large, elongated plagioclase and amphibole porphyroclasts have

Downloaded from http://pubs.geoscienceworld.org/gsa/gsabulletin/article-pdf/doi/10.1130/B36323.1/5738725/b36323.pdf
by University of Nevada Reno user

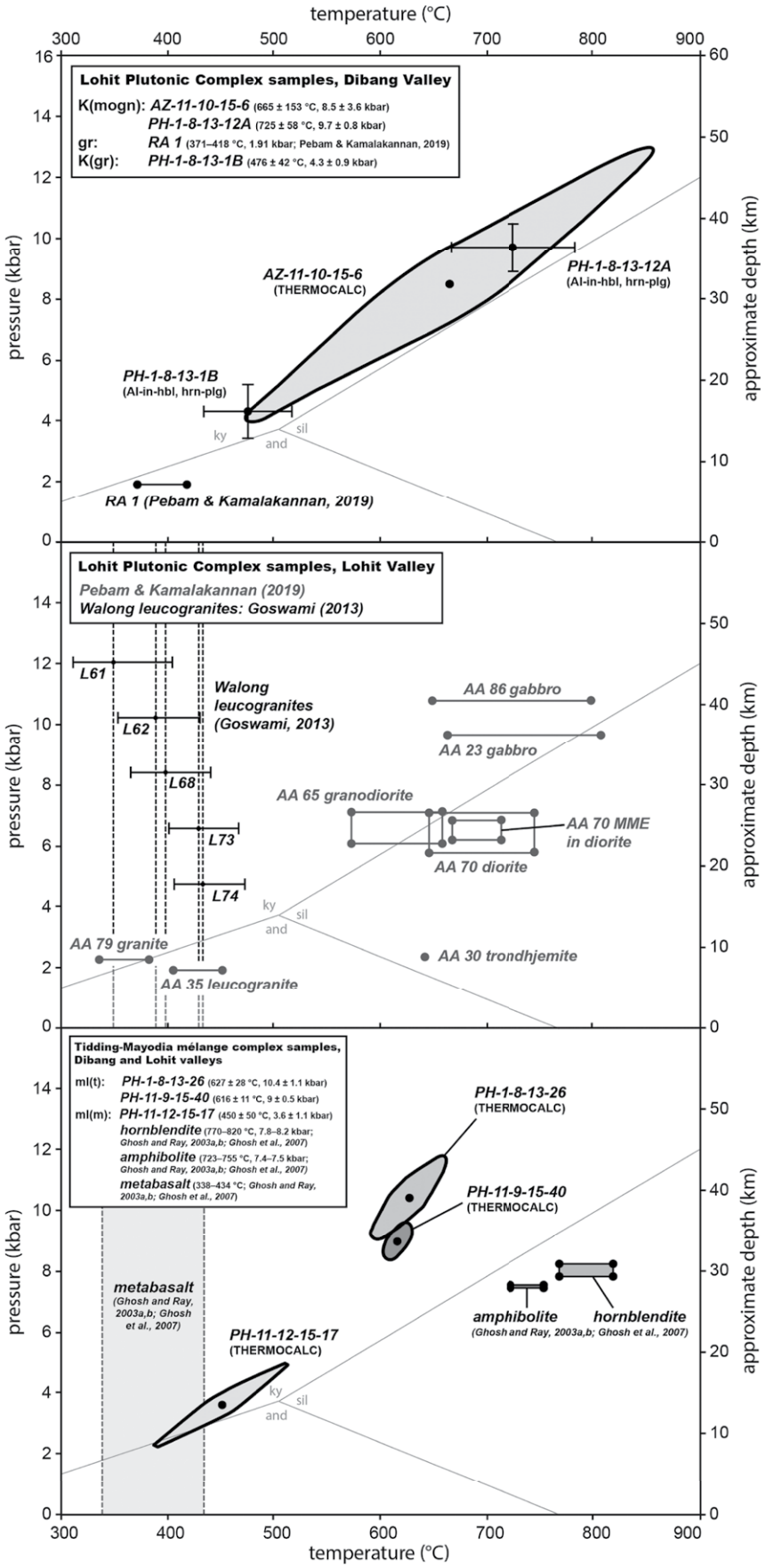

asymmetric, recrystallized tails that are indicative of a top-to-the-south sense of shear. Haproff et al. (2020) noted that the sample contains euhedral, ~1–8-mm-wide garnet porphyroblasts with fluid and quartz inclusions and a snowball texture that are indicative of rotation during growth. Amphibole porphyroclasts contain internal foliation that is parallel to the matrix foliation. Quartz grains display undulose extinction and lobate and interfingering boundaries indicative of dynamic recrystallization via GBM (Haproff et al., 2020). For microprobe analyses, we targeted adjacent biotite and muscovite blades and plagioclase grains that occur along garnet rims. Use of THERMOCALC 3.37 (Holland and Powell, 1998) for sample PH-1-8-13-26 yields upper amphibolite *P–T* conditions of 10.4 ± 1.1 kbar (= ~39 km depth) and 627 ± 28 °C (Fig. 12; Table 3). Garnet grains analyzed are Fe-rich almandines with a relatively homogenous, unzoned composition ($X_{Mg} = 0.15$).

Garnet schist sample PH-11-9-15-40 of the Tidding mélange complex contains the same mineral assemblage as sample PH-1-8-13-26 and a well-developed foliation predominantly defined by muscovite- and biotite-rich layers and recrystallized quartz- and plagioclase-rich layers (Fig. S18). The foliation wraps around ~1–5-mm-wide, euhedral garnet grains and is isoclinally folded. Garnet porphyroblasts and elongated amphibole and plagioclase porphyroclasts contain an internal foliation and aligned biotite, muscovite, and quartz inclusions that are parallel to the matrix foliation. Quartz grains display undulose extinction and lobate and interfingering boundaries that are indicative of dynamic recrystallization via GBM. For microprobe analyses, we targeted adjacent biotite and muscovite blades, recrystallized plagioclase grains, and elongated amphibole and ilmenite grains that occur along garnet rims. Use of THERMOCALC 3.37 yields upper amphibolite *P–T* conditions of 9 ± 0.5 kbar (= ~34 km depth) and 616 ± 11 °C (Fig. 12; Table 3). Analyzed

Figure 12. Compilation of pressure–temperature conditions of samples collected from the Lohit Plutonic Complex exposed along Dibang Valley (top) and Lohit Valley (middle), and the Tidding and Mayodia mélange complexes exposed along the Dibang and Lohit valleys (bottom). Data are compiled from this study, Ghosh and Ray (2003a, 2003b), Ghosh et al. (2007), Goswami (2013), and Pebam and Kamalakannan (2019). Pressure-based depth estimates assume a constant geothermal gradient and average crustal density of 2.7 g/cm^3.

Downloaded from http://pubs.geoscienceworld.org/gsa/gsabulletin/article-pdf/doi/10.1130/B36323.1/5738725/b36323.pdf
by University of Nevada Reno user

garnet grains are Fe-rich almandines with a relatively homogenous, unzoned composition ($X_{Mg} = 0.17$).

Garnet chlorite schist sample PH-11-12-15-17 of the Mayodia mélange complex contains garnet, plagioclase, muscovite, chlorite, clinozoesite, quartz, and rutile (Fig. S19). The well-developed foliation is predominantly defined by muscovite- and chlorite- and recrystallized quartz- and plagioclase-rich layers. The foliation is isoclinally folded and wraps around euhedral, ~1–5-mm-wide garnet porphyroblasts. Garnet grains contain quartz inclusions and asymmetric tails formed by muscovite and recrystallized quartz and plagioclase. We targeted clinozoisite grains, muscovite, and chlorite blades, and recrystallized plagioclase grains that occur along garnet rims for microprobe analyses. Use of THERMOCALC 3.37 yields greenschist *P–T* conditions of 3.6 ± 1.1 kbar (= ~13 km depth) and 450 ± 50 °C (Fig. 12; Table 3). Fe-rich almandine garnet grains show prograde growth zoning defined by increasing Mn and decreasing Mg from rim to core (Fig. S16; Table 3). The garnet composition used in the *P–T* calculation is an average of individual rim analyses that yield a similar Fe-rich almandine composition ($X_{Mg} = 0.09$).

Garnet chlorite schist sample PH-1-9-13-8 of the Mayodia mélange complex contains garnet, plagioclase, muscovite, chlorite, clinozoisite, quartz, titanite, and rutile (Fig. S20). The well-developed foliation is predominantly defined by muscovite, chlorite, and quartz and wraps around euhedral, ≤1-mm-wide garnet grains with asymmetric tails formed by chlorite and recrystallized quartz. Garnet grains are Fe-rich almandines ($X_{Mg} = 0.14$) (Fig. S16) with prograde growth zoning defined by increasing Mn and decreasing Mg from rim to core (Figs. S16 and S21; Table 3).

Microstructural Observations and Results of EBSD Analyses

Orthogneiss sample PH-1-15-20-3 contains recrystallized quartz surrounded by chlorite, muscovite, amphibole, and epidote that define the well-developed foliation (Fig. S22). Quartz grains feature undulose extinction and lobate and interfingering boundaries that are indicative of dynamic recrystallization via GBM at ~550–650 °C (e.g., Law, 2014). Microstructures include isoclinal folds, asymmetric porphyroclasts and boudins, and S-C fabric that is indicative of a top-to-the-southeast sense of shear.

Mylonitic orthogneiss sample PH-1-15-20-5 is quartz-rich and contains a well-developed foliation and mineral assemblage similar to that of sample PH-1-15-20-3 with the addition of recrystallized plagioclase grains (Fig. S23). Quartz grains show evidence for GBM based on lobate and interfingering boundaries.

Mylonitic orthogneiss sample PH-1-15-20-6 contains muscovite S-C fabric and asymmetric quartz, plagioclase, and amphibole porphyroclasts with recrystallized tails that are indicative of a north-side-up sense of shear (Fig. S24). Quartz grains feature undulose extinction and lobate and interfingering boundaries that are indicative of GBM.

Mylonitic orthogneiss sample PH-1-15-20-8 contains recrystallized quartz, plagioclase, and calcite, as well as chlorite, muscovite, and amphibole that form the well-developed foliation (Fig. S25). Minor pyrite occurs throughout the sample. Quartz grains feature undulose extinction and lobate and interfingering boundaries that are indicative of GBM. Quartz and mica form S-C fabric that is indicative of a north-side-up sense of shear.

Mylonitic marble sample PH-1-15-20-14 contains calcite and minor quartz that define the foliation (Fig. S26). Quartz and calcite grains are mostly similar in size and feature

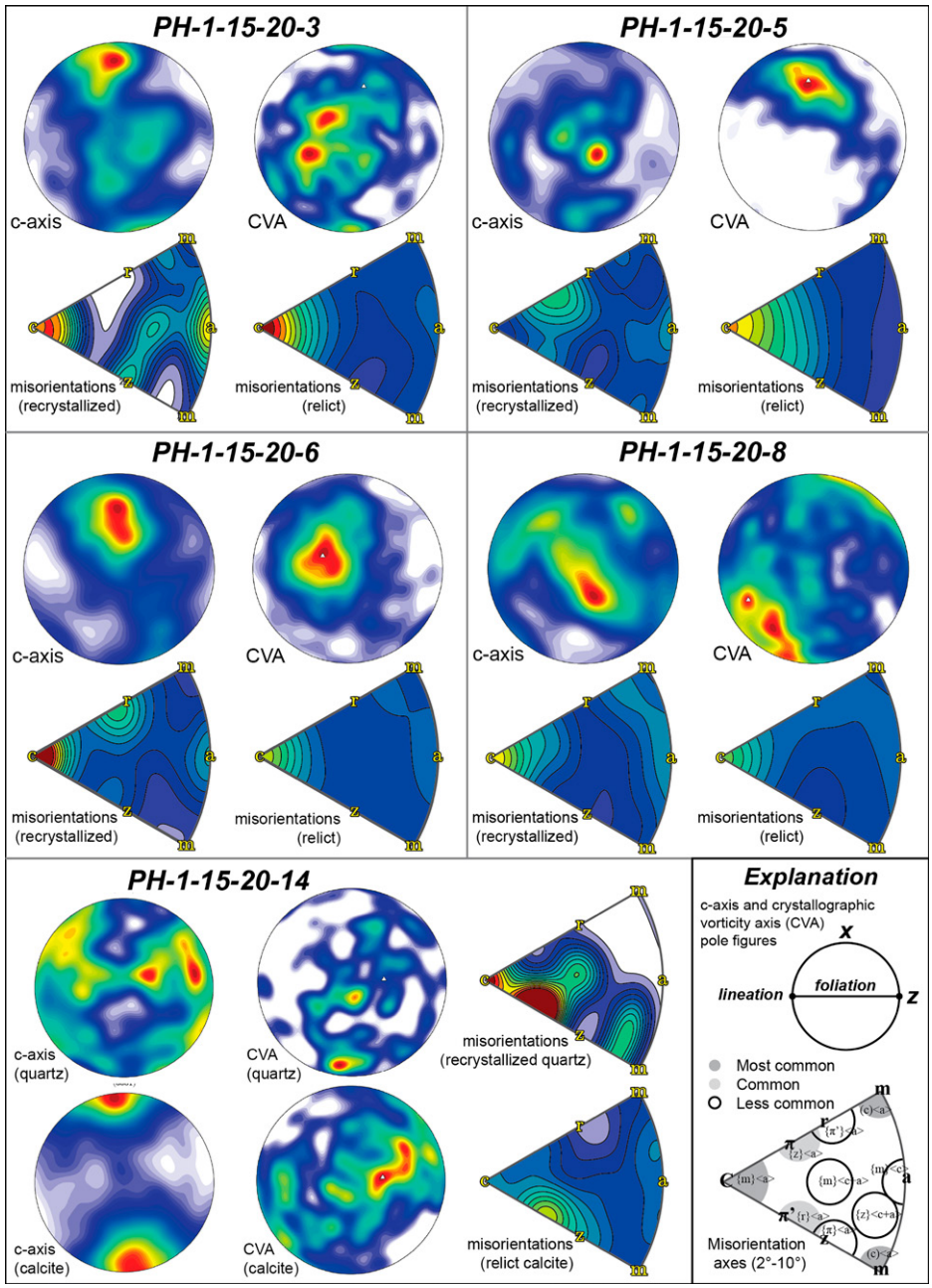

Figure 13. Results of electron backscatter diffraction analyses of quartz from five samples collected across the Lohit thrust shear zone, Dibang Valley, are shown.

Downloaded from http://pubs.geoscienceworld.org/gsa/gsabulletin/article-pdf/doi/10.1130/B36323.1/5738725/b36323.pdf
by University of Nevada Reno user

relatively straight boundaries that are indicative of dynamic recrystallization via subgrain rotation. Some foliation-parallel, calcite-rich layers contain smaller recrystallized grains and form aggregates with asymmetric tails that are indicative of a north-side-up sense of shear.

EBSD analyses of quartz grains within the five samples across the Lohit thrust shear zone reveal moderate to weak CPOs, which are indicated by *M* index values of 0.01–0.08, *R* values of >0.45, and *B* values of 0.12–0.54 and suggest fabrics trending toward random (Figs. 5 and 13; Table 4). Within the Lohit thrust shear zone, fabric intensity measured by these proxies decreases toward the observed location of the discrete Lohit thrust fault (Fig. 5). The *K* parameters are ≥1, demonstrating fabric shapes that range from girdle/cluster transitions toward uniaxial clusters (Woodcock, 1977). The single exception is the more girdled sample PH-1-15-20-6 ($K = 0.27$) (Table 4). Grain sizes of recrystallized quartz are 67–134 μm, which correspond to moderate–low flow stresses of 17–32 MPa (Cross et al., 2017).

Quartz *c*-axis distributions plotted on pole figures are somewhat dispersed, with most displaying maxima at, or just off, the center of the pole figures (*Y* axis) (Fig. 13). Sample PH-1-15-20-3 is an exception, with maxima at the top of the pole figure, perpendicular to the foliation near the *X* axis (Fig. 13). Calcite analyses for sample PH-1-15-20-14 show well-defined maxima near the pole figure *X* axes. Misorientation axes (5–10°) on an inverse pole figure plot show maxima clustered around the *c* axis for both recrystallized and relict grains (Fig. 13). Recrystallized grains show more dispersed and variable distributions, whereas the relict grains are more focused with concentrations near the *c* axis, except for sample PH-1-15-20-14, which shows a relict misorientation cluster near the π' axis (Neumann, 2000; Fig. 13). CVA analyses show that most are clustered near the center of the pole figure (*Y* axis), except for sample PH-1-15-20-8, which plots along the primitive circle nearly perpendicular to the foliation (Fig. 13).

DISCUSSION

Correlation of the Lohit Plutonic Complex as Gangdese Lower Arc Crust

Geochronologic results show that leucogneiss and leucogranite bodies of the Western Lohit Plutonic Complex belt (ca. 100–82 Ma) (Fig. 10; Table 1), located both within the Lohit thrust shear zone and in its hanging wall to the north (Fig. 4), were not emplaced during Cenozoic thrusting and instead correspond with published ca. 156–69 Ma granitoid crystallization ages of the Western and Eastern Lohit Plutonic Complex belts (Lin et al., 2013; Bikramaditya et al., 2020; Haproff et al., 2019; Fig. 4). In addition, a compilation of major- and trace-element geochemical data of 120 plutonic samples of the Western and Eastern Lohit Plutonic Complex belts (Sharma et al., 1991; Lin et al., 2013; Goswami, 2013; Haproff et al., 2019; Pebam and Kamalakannan, 2019; Bikramaditya et al., 2020) shows that Cretaceous Lohit Plutonic Complex granitoids are largely consistent in their granitoid-type classifications and compositions being indicative of volcanic arc origins (Figs. S6 and S7). Both the geochemical compositions and crystallization ages of the Cretaceous Lohit Plutonic Complex granitoids are comparable to those of the northern Gangdese batholith of the southern Lhasa terrane to the west, which supports previous interpretations that the lithotectonic units are correlative and were generated along a laterally continuous Andean-type margin along the southern Lhasa terrane (Lin et al., 2013; Haproff et al., 2019; Bikramaditya et al., 2020).

Geobarometry results of Lohit Plutonic Complex rocks indicate pressures of 4.3–10.8 kbar, equivalent to ~16–40 km depth (Pebam and Kamalakannan, 2019; this study; Fig. 12; Table 3). Exceptions include a few bodies of granite, leucogranite, and trondhjemite emplaced at ~7–8 km (~2 kbar) (Pebam and Kamalakannan, 2019; Fig. 12). Garnet-bearing migmatitic orthogneiss sample AZ-11-10-15-16, collected from the Cretaceous Western Lohit Plutonic Complex belt, records metamorphism at ~32 km depth (8.5 kbar) (Fig. 12). Similarly, mylonitic orthogneiss sample PH-1-8-13-12A, collected from the Cretaceous Western Lohit Plutonic Complex belt in the Lohit thrust shear zone, was emplaced at ~36 km depth (9.7 kbar) (Fig. 12). These depths are comparable to emplacement depths of ~36–40 km (9.7–10.8 kbar) for two Lohit Plutonic Complex gabbro samples (Pebam and Kamalakannan, 2019; Fig. 12).

We estimated Lohit Plutonic Complex paleocrustal thickness by compiling whole-rock Sr/Y and La/Yb ratios of granitoid samples and applying the filtering criteria of Profeta et al. (2015) and paired the Sr/Y–La/Yb calibration of Sundell et al. (2021; Fig. S27A). The results for six granitoid samples (Lin et al., 2013; Haproff et al., 2019; Bikramaditya et al., 2020; this study) plotted with their U–Pb crystallization ages show that from ca. 115–69 Ma, the crustal thickness of the Lohit Plutonic Complex was between ~38 km and 52 km (Fig. S27B). This range in crustal thickness is comparable to that of the Gangdese batholith of the Lhasa terrane over the same timespan (Cao et al., 2020; Sundell et al., 2021). Given that Lohit Plutonic Complex rocks were at ~32–40 km depth within a ~38–52-km-thick crust from ca. 115–69 Ma, we interpret that the Lohit Plutonic Complex represents exposed lower arc crust of the northern Gangdese batholith. This interpretation is supported by the similarities of the Lohit Plutonic Complex and other exposed lower continental arc crusts (e.g., Sierra Nevada batholith of the North American Cordillera; Saleeby et al., 2003), such as the presence of Mesoproterozoic garnet migmatitic orthogneiss (Fig. 6) intruded by latest Jurassic–Cretaceous intermediate- to felsic-composition, peraluminous, volcanic-arc diorite, tonalite, granodiorite, granite, and migmatitic orthogneiss and minor gabbro, amphibolite, leucogneiss, and leucogranite (Figs. 7 and S1). Prior to this study, Zhang et al. (2020) identified Gangdese lower arc crust with similar lithologic and geochemical characteristics ~150 km to the northwest, in the hanging wall of a ductile shear zone that was previously mapped as the easternmost Gangdese thrust (e.g., Ding et al., 2001; Fig. 1B). Researchers note that the existence of a major crustal thickening structure like the Gangdese thrust could have accommodated northward footwall underthrusting of old continental crust to generate S-type granitoids with negative $\varepsilon_{Hf}(t)$ in the lower crust (Zhang et al., 2015, 2020).

Cenozoic Deformation of the Tidding Mélange Complex and Crustal Thickening along the Indian-Neotethys Boundary

Our field observations demonstrate that deformation of the Tidding mélange complex occurred as: (1) top-to-the-south ductile shear concentrated across the ~1-km-wide Tidding thrust shear zone and discrete Tidding thrust fault located in the middle of the shear zone (Fig. 4B); and (2) the development of foliation-parallel compositional layering, mineral stretching lineation, top-to-the-south S-C fabric, asymmetric boudins, and south-vergent asymmetric and isoclinal folds (Fig. 9). Geothermobarometry results and GBM quartz textures of Tidding mélange complex samples (PH-1-8-13-26 and PH-11-9-15-40) indicate upper amphibolite-facies metamorphism at temperatures of >600 °C and depths of ~34–39 km (9–10.4 kbar) (Fig. 12; Table 3). These results are similar to published geothermobarometry results for hornblendite and amphibolite of the equivalent Mayodia mélange complex that indicate amphibolite-facies conditions at ~27–28 km depth (Ghosh and Ray, 2003a, 2003b; Ghosh et al., 2007; Fig. 12). Garnet chlorite schist samples PH-1-9-13-8 and PH-11-12-15-17 contain greenschist-facies mineral assemblages and *P–T* conditions (Fig. 12) that may reflect retrogression of the Tidding-Mayodia mélange complex following peak upper amphibolite-facies metamorphism.

Downloaded from http://pubs.geoscienceworld.org/gsa/gsabulletin/article-pdf/doi/10.1130/B36323.1/5738725/b36323.pdf
by University of Nevada Reno user

Upper amphibolite-facies metamorphism (9–10.4 kbar; >600 °C) of the Tidding mélange complex must have occurred prior to ca. 36–30 Ma, which is the oldest range of muscovite and biotite $^{40}Ar/^{39}Ar$ and zircon (U–Th)/He ages (Haproff et al., 2020; Salvi et al., 2020) that track cooling through lower temperatures of ~300–500 °C (Harrison et al., 1985; Hames and Bowring, 1994; Grove and Harrison, 1996; Harrison et al., 2009) and ~180 °C (Reiners, 2005). Based on an implied fast cooling rate (i.e., >30 °C/m.y.) and the hanging wall positions of the thermochronology samples, Haproff et al. (2020) interpreted that the ca. 36–30 Ma cooling was related to coeval surface erosion and exhumation of the Tidding mélange complex during motion over a footwall ramp along the Tidding thrust shear zone. Expanding upon this interpretation, the depth estimates of ~27–39 km for the Tidding mélange complex provide a minimum estimate of displacement over the footwall ramp. This displacement estimate, added to the ~40 km map-view distance between the root zone of the Tidding thrust shear zone to the southernmost exposure of the thrust (Haproff et al., 2020; Fig. 2), yields a minimum net displacement of ~67–79 km.

The post-30 Ma slip history of the Tidding thrust shear zone is unclear. New biotite and muscovite $^{40}Ar/^{39}Ar$ ages of ca. 21–20 Ma (samples PH-1-8-13-22B and PH-11-9-15-36) (Fig. 11A; Table 2), located north and south of the ca. 36–30 Ma samples (Fig. 4B), may reflect cooling following localized intra-unit deformation. Alternatively, the ca. 21–20 Ma $^{40}Ar/^{39}Ar$ ages may be a result of renewed exhumation and cooling during reactivated slip along the Tidding thrust shear zone following burial and reheating in the footwall of the Lohit thrust shear zone (see below). The ca. 21–20 Ma $^{40}Ar/^{39}Ar$ ages could also be a product of exhumation and cooling during displacement over a footwall ramp along the structurally lower Demwe thrust (Fig. 2), which has a minimum age of ca. 16 Ma based on biotite $^{40}Ar/^{39}Ar$ thermochronology (Salvi et al., 2020).

Given that the Tidding thrust shear zone is the major structure in the northern Indo-Burma Ranges placing remnant Neotethys oceanic lithosphere and accretionary metasedimentary rocks atop Indian continental rocks, we can compare its timing and geometry with those of other structures along the northern margin of the Himalayan orogen (Figs. 1B and 3). Initial obduction of Neotethys rocks atop the Tethyan Himalayan sequence occurred during the latest Cretaceous–Paleocene in southwestern and south-central Tibet (Murphy and Yin, 2003; Ding et al., 2005). Peak eclogite-facies metamorphism of subducted Indian continental rocks, including the Tso Morari and Kaghan Valley complexes of the northwestern Himalaya, initiated at ca. 47 Ma, and was followed by thrust-related exhumation at ca. 47–31 Ma (de Sigoyer et al., 2000; Schlup et al., 2003; Wilke et al., 2010; Donaldson et al., 2013). Similarly, Tethyan Himalayan sequence rocks exposed in the northwestern Himalaya, the Lopu Range of south-central Tibet, and southeastern Tibet record the onset of prograde metamorphism at ca. 46–40 Ma (Williams et al., 2001; Wiesmayr and Grasemann, 2002; Dunkl et al., 2011; Laskowski et al., 2016). Subsequent thrust-related exhumation and retrograde metamorphism of Tethyan Himalayan sequence rocks in the Lopu Range occurred at ca. 39–34 Ma (Laskowski et al., 2016). During the Oligocene–Miocene, southward migration of thrusting within the Tethyan Himalayan sequence and Greater Himalayan Crystalline Complex was coeval with out-of-sequence thrusting along the Indian-Neotethys boundary (Ratschbacher et al., 1994; Murphy and Yin, 2003; Dunkl et al., 2011), including slip along the ca. 25–10 Ma Great Counter thrust (Yin et al., 1999; Harrison et al., 2000; Wang et al., 2015; Laskowski et al., 2018).

In comparison with these existing constraints, the ca. 36–30 Ma earliest record of cooling, interpreted to be related to coeval surface erosion and exhumation during slip along the Tidding thrust shear zone, may represent a significantly delayed initial obduction of Neotethys rocks along the easternmost collisional boundary. Alternatively, ca. 36–30 Ma cooling may reflect the timing of reactivated, out-of-sequence exhumation during slip along the Tidding thrust shear zone that was roughly coincident with shortening and exhumation along the northern margin of the Himalayan orogen following an earlier, possibly latest Cretaceous–Paleogene obduction event.

Despite the broadly similar timing of thrust-related exhumation along the Indian-Neotethys boundary, key orogen-parallel variations include the contrasting geometries, kinematics, and timing of the south-directed Tidding thrust shear zone versus the widely exposed, north-directed, ca. 25–10 Ma Great Counter thrust (Yin et al., 1999; Harrison et al., 2000; Wang et al., 2015; Laskowski et al., 2018). In addition, the Tethyan Himalayan sequence and Greater Himalayan Crystalline Complex are not exposed in the footwall of the Tidding thrust shear zone as Indus-Yarlung suture zone rocks are thrust directly atop the Lesser Himalayan sequence-equivalent Mayodia gneiss (Sarma et al., 2012; Haproff et al., 2019; Figs. 2 and 3). These differences may ultimately be related to variations in the structural style and magnitude of deformation along the Indian-Neotethys boundary across the eastern Himalayan syntaxis. The Great Counter thrust in the Himalaya may have overthrust and buried a south-directed thrust at the base of the Indus-Yarlung suture zone, whereas in the northern Indo-Burma Ranges, a backthrust with top-to-Lhasa-terrane kinematics did not develop. The absence of the Tethyan Himalayan sequence and Greater Himalayan Crystalline Complex in the footwall of the Tidding thrust shear zone may be related to local underthrusting and/or increased shortening and erosion (Haproff et al., 2019, 2020).

Cenozoic Deformation of the Lohit Plutonic Complex and Crustal Thickening of the Neotethys-Lhasa Terrane Boundary

Field and microstructural observations demonstrate that crustal thickening along the southern Lhasa terrane margin of the northern Indo-Burma Ranges was concentrated along the ~5-km-wide Lohit thrust shear zone and the discrete Lohit thrust fault near the base of the shear zone (Figs. 4 and 5). In contrast to previous observations, the Lohit thrust shear zone has an overall subvertical geometry and north-side-up kinematics (Figs. 5, 8, S3, and S4). This geometry may be a result of rotation from an initial north-dipping geometry during late Miocene duplexing at lower structural levels (Haproff et al., 2020; Salvi et al., 2020). The Lohit thrust shear zone developed relatively weak CPOs as observed in our microstructural observations and EBSD results. GBM quartz deformation textures, *c*-axis distributions that plot near the *Y* axis, and misorientation axes are consistent with dominantly prism <a> slip (Fig. 13) at generalized temperatures of ~550–650 °C (e.g., Law, 2014). The misorientation plots for recrystallized grains show more variability, but we favor interpretations based on the relict grains, which potentially reveal more intra-granular crystallographic dispersion around the vorticity axis and therefore are more representative of flow conditions (e.g., Piette-Lauzière et al., 2020). These interpretations support prism <a> activity in quartz. CVA analyses suggest that most samples record sub-simple shear parallel to the mineral stretching lineation except for sample PH-1-15-20-8, which shows evidence of an out-of-plane, wrench component (e.g., Michels et al., 2015; Fig. 13). Thus, the recorded finite strain potentially reflects a variable kinematic history across the Lohit thrust shear zone, which explains the complicated and diffuse CPOs. The weak CPOs may also be related to pinning at quartz grain boundaries with other mineral phases. Nonetheless, we interpret that the Lohit thrust shear zone deformed at temperatures in

Downloaded from http://pubs.geoscienceworld.org/gsa/gsabulletin/article-pdf/doi/10.1130/B36323.1/5738725/b36323.pdf
by University of Nevada Reno user

the range of ~550–650 °C (e.g., Law, 2014), which is consistent with the relatively low flow stresses of ≤32 MPa that were observed via paleopiezometry (e.g., Hirth et al., 2001; Table 4). However, we acknowledge that strain rate, the polyphase nature of this deformation, and water content make this estimate imprecise. We note that the deformation temperatures ~550–650 °C are slightly cooler than the temperature of 725 ± 58 °C based on amphibole-plagioclase thermometry for the Lohit thrust shear zone (sample PH-1-8-13-12A) (Fig. 12; Table 3). The hotter temperature of 725 ± 58 °C may represent conditions during magmatic emplacement of the sample and/or adjacent plutons, whereas quartz within the sample re-equilibrated under slightly lower temperatures during deformation.

Measured increases in fabric intensity across ductile shear zones have been used to identify discrete structural discontinuities along which strain is concentrated (e.g., Starnes et al., 2020). Within the Lohit thrust shear zone, fabric intensity decreases southwards toward the observed location of the discrete Lohit thrust fault (Fig. 5 and Table 4). Paradoxically, this finding suggests relatively lower finite strain magnitudes toward the Lohit thrust fault. This spatial relationship may be the result of migration of the highest strain during the lifespan of the shear zone. In this scenario, the fabric intensity measurements record concentrated ductile strain along the northern margin of the shear zone during an earlier, possible non-discrete phase of the shear zone's lifespan. Subsequently, strain became concentrated along the southern margin of the shear zone where the Lohit thrust fault developed as the major structural discontinuity. This change may have occurred as the shear zone was exhumed and reached temperatures lower than ~550–650 °C, thus localizing strain along a more discrete and spatially limited brittle-plastic structure. More detailed examination of strain intensities and deformation conditions, mechanisms, and timing is needed across the Lohit thrust shear zone to test this hypothesis.

Slip along the Lohit thrust shear zone is interpreted to have been underway at ca. 25–23 Ma and may have continued until ca. 12–10 Ma, based on the $^{40}Ar/^{39}Ar$ results of K-feldspar and muscovite grains (samples PH-11-11-15-14 and PH-1-15-20-6, respectively) that form the mylonitic foliation and stretching lineation (Figs. 11 and S10–S12; Table 2). In this interpretation, the section of the Lohit thrust shear zone that previously deformed at ~550–650 °C was subsequently exhumed and cooled through ~500–125 °C as slip occurred along the basal, discrete Lohit thrust fault and erosion occurred on the surface (Figs. 4A, 5, and 11). Direct temporal constraints on the cessation of slip along the Lohit thrust shear zone remain unknown. Two ca. 25–24 Ma biotite $^{40}Ar/^{39}Ar$ ages and four ca. 13–11 Ma zircon (U–Th)/He ages from the Eastern Lohit Plutonic Complex belt (Salvi et al., 2020; this study; Figs. 4A and 11) fall within this time span and may reflect coeval cooling during hanging-wall exhumation and surface erosion. One ca. 31 Ma biotite $^{40}Ar/^{39}Ar$ age from the middle section of the Eastern Lohit Plutonic Complex belt (Salvi et al., 2020) (Fig. 4A) reflects slightly earlier cooling compared to Lohit Plutonic Complex rocks to the north and south.

From our constraints on the structural position, geometry, kinematics, and timing of the Lohit thrust shear zone, the most comparable structure to the west is the Gangdese thrust (Figs. 1 and 3). Both the Lohit thrust shear zone and the Gangdese thrust predominantly place Gangdese-equivalent, magmatic arc granitoids of the southern Lhasa terrane atop remnant Neotethys oceanic lithosphere and accretionary metasedimentary rocks (Figs. 1 and 3). The Lohit thrust shear zone is interpreted to have initiated with a north-dipping geometry and top-to-the-south kinematics like those of the Gangdese thrust. The Gangdese thrust was active at ca. 27–23 Ma and possibly terminated as late as ca. 18 Ma (Yin et al., 1994, 1999; Harrison et al., 2000), which overlaps with our interpreted timing of slip along the Lohit thrust shear zone at ca. 25–23 Ma and possibly as late as ca. 12–10 Ma. In addition, the Yarlung-Tsangpo Canyon thrust, located between the Gangdese thrust to the west and Lohit thrust shear zone to the southeast, has similar hanging-wall and footwall rock types as the two latter thrusts (Ding et al., 2001; Figs. 1 and 3) and may have been active at ca. 21–13 Ma based on biotite $^{40}Ar/^{39}Ar$ and U–Pb zircon ages in its hanging wall (Booth et al., 2004; Gong et al., 2015, and references therein). Although ca. 21–13 Ma slip along the Yarlung-Tsangpo Canyon thrust is largely more recent than the timing of the Gangdese thrust and Lohit thrust shear zone, it does overlap with the ca. 18 Ma lower age bound on the Gangdese thrust (Yin et al., 1994) and ca. 12–10 Ma possible youngest ages of exhumation related to slip along the Lohit thrust shear zone.

Based on the similarities between the Gangdese thrust, Lohit thrust shear zone, and Yarlung-Tsangpo Canyon thrust, we interpret that these faults were segments of a single, laterally continuous, south-directed thrust that served as the preeminent crustal thickening structure along the southern Lhasa terrane margin during the Oligocene–Miocene. This laterally continuous thrust may have formed part of a larger blind, south-directed duplex system analogous to the Gangdese culmination model of Laskowski et al. (2018) and remained at depths equivalent to just above the ~300–500 °C range of combined biotite and muscovite $^{40}Ar/^{39}Ar$ closure temperatures during its lifespan. Slip along the Gangdese thrust segment may have ceased by ca. 18 Ma (Yin et al., 1994), whereas the Lohit and Yarlung-Tsangpo Canyon thrust segments potentially remained active until after ca. 13–10 Ma. Following cessation of slip, much of the combined thrust remained buried, which explains the scarce exposures of the Gangdese thrust (Laskowski et al., 2018, Fig. 1B). In contrast, the more extensive surface exposures of the easternmost Gangdese thrust, Yarlung-Tsangpo Canyon thrust, and Lohit thrust shear zone in the eastern Himalayan syntaxis region and northern Indo-Burma Ranges are interpreted to be a product of localized exhumation during duplexing of Indian continental rocks at lower structural levels since late Miocene time (Ding et al., 2001; Booth et al., 2009; Gong et al., 2015; Govin et al., 2020). At Namche Barwa, late Miocene duplexing of Indian continental rocks resulted in broad antiformal folding and exhumation of the overlying combined Gangdese–Yarlung–Tsangpo Canyon–Lohit thrust (Ding et al., 2001) and Gangdese lower arc crust in its hanging wall. Similarly, late Miocene duplexing of Lesser Himalayan sequence-equivalent rocks in the northern Indo-Burma Ranges (Haproff et al., 2020; Salvi et al., 2020) exhumed and rotated the overlying Lohit thrust shear zone and Lohit Plutonic Complex lower arc crust in its hanging wall to their present-day orientations. Concentrated duplexing and exhumation in these regions since the late Miocene may have been related to clockwise crustal flow via distributed shortening around northeastern India (England and Houseman, 1986; Cobbold and Davy, 1988; Royden et al., 1997; Li et al., 2013; Haproff et al., 2018). In addition, focused river incision and erosion at the eastern Himalayan syntaxis and northern Indo-Burma Ranges may have assisted in concentrating duplexing to maintain critical taper, resulting in increased exhumation of overlying rocks (Zeitler et al., 2014; Govin et al., 2020; Liu et al., 2020).

Structural Evolution of the India-Asia Collisional Boundary

Beginning in the latest Cretaceous to latest Eocene, initial India-Asia collision and closure of the Neotethys Ocean resulted in the emplacement of remnant oceanic lithosphere and accretionary metasedimentary rocks atop the Indian continental margin (Murphy and Yin, 2003). During this period, Indian continental rocks

Downloaded from http://pubs.geoscienceworld.org/gsa/gsabulletin/article-pdf/doi/10.1130/B36323.1/5738725/b36323.pdf
by University of Nevada Reno user

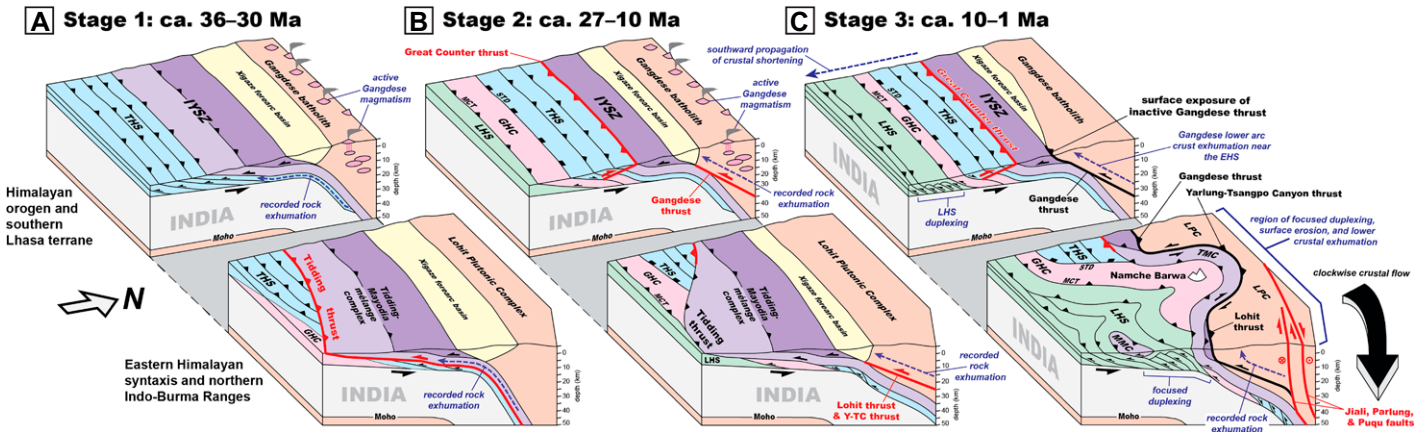

Figure 14. Schematic block diagrams show the Cenozoic structural evolution of the India-Asia collisional boundary. (A) By ca. 36–30 Ma, shortening and exhumation occurred within the Tethyan Himalayan sequence and Indus-Yarlung suture zone, including the Tidding and Mayodia mélange complexes. The Tidding thrust shear zone was active at that time. (B) From ca. 27–10 Ma, slip along the Gangdese–Yarlung–Tsangpo Canyon–Lohit thrust and hanging-wall exhumation were coeval with slip along the Great Counter thrust. Himalayan shortening continued to propagate southwards toward the foreland. (C) By ca. 10–1 Ma, focused duplexing and erosion resulted in folding, rotation, and exhumation of the overlying Gangdese–Yarlung–Tsangpo Canyon–Lohit thrust and its hanging-wall rocks, including Gangdese lower-arc crust. Focused duplexing may have been related to clockwise crustal flow around northeastern India.

were subducted beneath the southern Lhasa terrane and metamorphosed at peak eclogite-facies conditions, followed by thrust-related exhumation to mid-crustal depths (de Sigoyer et al., 2000; Schlup et al., 2003; Wilke et al., 2010; Dunkl et al., 2011; Donaldson et al., 2013; Laskowski et al., 2016). In the northern Indo-Burma Ranges, slip along the Tidding thrust shear zone by ca. 36–30 Ma exhumed Neotethys oceanic lithosphere and accretionary metasedimentary rocks (i.e., Tidding and Mayodia mélange complexes) from depths of ~27–39 km at upper amphibolite-facies conditions (Fig. 14A). A minimum estimate of displacement along the Tidding thrust shear zone is ~67–79 km. It is unclear whether the ca. 36–30 Ma phase of slip along the Tidding thrust shear zone occurred during delayed initial emplacement of Neotethys rocks atop the Indian continental margin or out-of-sequence reactivation following an earlier obduction event. Directly southeast of the northern Indo-Burma Ranges, slip along the Chongshan shear zone began at ca. 34–32 Ma (Wang et al., 2006; Akciz et al., 2008; Zhang et al., 2010; Fig. 14A), signaling the onset of partitioning of India-Asia convergence between shortening along the collisional boundary and southward strike-slip extrusion of Asian lithosphere.

During the Oligocene–Miocene, crustal thickening along the southern Lhasa terrane margin was accommodated by out-of-sequence slip along a laterally continuous, south-directed blind thrust formed by the Gangdese thrust, Yarlung-Tsangpo Canyon thrust, and Lohit thrust shear zone (Fig. 14B). At the eastern Himalayan syntaxis, the combined Gangdese–Yarlung–Tsangpo Canyon–Lohit thrust was rooted in the lower crust and exhumed Gangdese lower arc rocks to mid-crustal levels. South of the southern Lhasa terrane, Oligocene–Miocene shortening in the Tethyan Himalayan sequence and slip along the South Tibetan detachment and Main Central thrust were coeval with out-of-sequence shortening along the Indus-Yarlung suture zone (Ratschbacher et al., 1994; Murphy and Yin, 2003; Dunkl et al., 2011), including north-directed slip along the ca. 25–10 Ma Great Counter thrust (Yin et al., 1999; Harrison et al., 2000; Wang et al., 2015; Laskowski et al., 2018; Fig. 14B). Slip along the Gangdese–Yarlung–Tsangpo Canyon–Lohit thrust may have ceased by the early to middle Miocene, during which the thrust was buried along much of its length by the overlying Great Counter thrust and Kailas Formation. In the northern Indo-Burma Ranges, shortening migrated to Lesser Himalayan sequence-equivalent rocks with slip along the Demwe thrust by ca. 16 Ma (Salvi et al., 2020), which may have been coeval with out-of-sequence deformation in the Tidding mélange complex and Lohit Plutonic Complex. During this period, India-Asia convergence continued to be partitioned between shortening along the collisional boundary and strike-slip motion in southeastern Tibet along the Jiali, Puqu, and Parlung faults (ca. 23–11 Ma), and the Gaoligong shear zone (ca. 18–13 Ma) and Chongshan shear zone (ca. 19–14 Ma) (Zhong et al., 1991; Ding et al., 2001; Lee et al., 2003; Wang et al., 2006; Akciz et al., 2008; Lin et al., 2009; Zhang et al., 2010; Fig. 14C).

By late Miocene time, shortening continued to propagate southwards in the Himalayan orogen with the activation of the Main Boundary thrust and Main Frontal thrust (Meigs et al., 1995; DeCelles et al., 2001; Fig. 14C). At the eastern Himalayan syntaxis and northern Indo-Burma Ranges, clockwise crustal flow around northeastern India (e.g., Haproff et al., 2018) resulted in concentrated duplexing (>163 km of crustal shortening; Salvi et al., 2020) of Indian continental rocks at depth, modulated by focused river incision and erosion at the surface (Zeitler et al., 2014; Govin et al., 2020; Liu et al., 2020). Concentrated duplexing of Indian continental rocks folded, rotated, and exhumed the overlying Gangdese–Yarlung–Tsangpo Canyon–Lohit thrust (Ding et al., 2001) and Gangdese lower arc crust to their present-day orientations and surface exposures (Fig. 14C).

CONCLUSIONS

Our integrated field and analytical study across the northern Indo-Burma Ranges, combined with existing research of the Indus-Yarlung suture zone and southern Lhasa terrane to the west, improved our understanding of the Cenozoic crustal thickening history along the India-Asia collisional boundary. Key findings of this study include:

(1) Gangdese-equivalent, Cretaceous arc granitoids of the Lohit Plutonic Complex were emplaced at ~32–40 km depth in crust that is estimated to have been ~38–52 km thick. Based

Downloaded from http://pubs.geoscienceworld.org/gsa/gsabulletin/article-pdf/doi/10.1130/B36323.1/5738725/b36323.pdf
by University of Nevada Reno user

on similar emplacement depths and lithological and geochemical characteristics, we interpret that the Lohit Plutonic Complex is Gangdese lower arc crust, which is supported by lithologic and geochemical characteristics that are similar to those of other lower arc sections, including Gangdese lower arc crust identified ~150 km to the northwest (Zhang et al., 2020).

(2) Crustal thickening along the easternmost Indus-Yarlung suture zone (i.e., Tidding-Mayodia mélange complex) was accommodated via slip along the subvertical, north-side-up Lohit thrust shear zone and the south-directed Tidding thrust shear zone that form the respective upper and lower boundaries of the suture zone.

(3) Upper amphibolite metamorphic assemblages of Tidding and Mayodia mélange complexes indicate burial depths of ~27–39 km. Mélange rocks cooled at ca. 36–30 Ma, which we interpret was related to exhumation during slip along the north-dipping Tidding thrust shear zone. Similarly, Lohit Plutonic Complex rocks cooled at ca. 25–10 Ma, which is interpreted to be related to exhumation during slip along the Lohit thrust shear zone. Additional thermo- and geochronology coupled with geothermobarometry across the Lohit and Tidding thrust shear zones and their hanging walls can improve estimations of slip timing and *P–T* histories.

(4) Microstructural observations and EBSD results across the Lohit thrust shear zone show relatively weak CPOs, which indicate dominantly prism <a> slip, GBM quartz deformation textures, and flow stresses of ≤32 MPa at interpreted amphibolite-grade conditions. Fabric intensity decreases toward the observed location of the discrete Lohit thrust fault within the shear zone, which may be a product of migration of the highest strain.

The Tidding thrust shear zone of the northern Indo-Burma Ranges and the Great Counter thrust of the Himalayan orogen to the west both separate Indian continental rocks from the Indus-Yarlung suture zone. However, the north-dipping geometry, top-to-the-south kinematics, and ca. 36–30 Ma timing of the Tidding thrust shear zone differ from the south-dipping geometry, top-to-the-north kinematics, and ca. 25–10 Ma timing of the Great Counter thrust, which suggests that the thrusts are not correlative. In contrast, major contractional structures that separate the Lhasa terrane from the Indus-Yarlung suture zone, including the Lohit thrust shear zone and the Gangdese and Yarlung-Tsangpo Canyon thrusts to the west, initiated with similar north-dipping geometries, top-to-the-south kinematics, and Oligocene–Miocene timing. Based on these similarities, we interpret that these thrusts formed a laterally continuous, blind thrust system that served as the preeminent crustal thickening structure along the southern Lhasa terrane margin and exhumed Gangdese lower arc crust in its hanging wall during the Oligocene–Miocene. Surface exposure of the blind thrust system in the eastern Himalayan syntaxis and northern Indo-Burma Ranges may have been a product of late Miocene-focused duplexing, surface erosion, and exhumation related to clockwise crustal flow around northeastern India. Although the Gangdese thrust remains buried along much of its length, our investigation of the correlative Lohit thrust shear zone provides more details on the kinematic history of this important crustal thickening structure.

ACKNOWLEDGMENTS

This research was supported by the University of North Carolina Wilmington and Tectonics Program of the National Science Foundation (EAR 1914503, EAR 1914501, EAR 2210075, and EAR 2210074). We thank Rachel Wells (Fayetteville State University) for performing cathodoluminescence imaging, Kathleen Zanetti (University of Nevada, Las Vegas) for conducting the $^{40}Ar/^{39}Ar$ analyses, and Joel DesOrmeau (University of Nevada, Reno) for assistance with electron backscatter diffraction analyses. We also acknowledge editor Wenjiao Xiao and associate editor Lu Wang for handling the manuscript and Delores Robinson, Zoe Braden, and an anonymous reviewer for providing constructive reviews. Data presented in this paper are available in the EarthChem Geochron data repository at https://www.geochron.org.

REFERENCES CITED

Aitchison, J.C., Davis, A.M., and Luo, H., 2002, New constraints on the India–Asia collision: The lower Miocene Gangrinboche conglomerates, Yarlung Tsangpo suture zone, SE Tibet: Journal of Asian Earth Sciences, v. 21, p. 251–263, https://doi.org/10.1016/S1367-9120(02)00037-8.

Aitchison, J.C., Davis, A.M., and Luo, H., 2003, The Gangdese thrust: A phantom structure that did not raise Tibet: Terra Nova, v. 15, p. 155–162, https://doi.org/10.1046/j.1365-3121.2003.00480.x.

Akciz, S., Burchfiel, B.C., Crowley, J.L., Jiyun, Y., and Liangzhong, C., 2008, Geometry, kinematics, and regional significance of the Chong Shan shear zone, eastern Himalayan syntaxis, Yunnan, China: Geosphere, v. 4, p. 292–314, https://doi.org/10.1130/GES00111.1.

An, W., Hu, X., Garzanti, E., BouDagher-Fadel, M.K., Wang, J., and Sun, G., 2014, Xigaze forearc basin revisited (South Tibet): Provenance changes and origin of the Xigaze Ophiolite: Geological Society of America Bulletin, v. 126, p. 1595–1613, https://doi.org/10.1130/B31020.1.

Anderson, J.L., and Smith, D.R., 1995, The effects of temperature and fO_2 on the Al-in-hornblende barometer: The American Mineralogist, v. 80, p. 549–559, https://doi.org/10.2138/am-1995-5-614.

Armijo, R., Tapponnier, P., and Han, T., 1989, Late Cenozoic right-lateral strike-slip faulting in southern Tibet: Journal of Geophysical Research: Solid Earth, v. 94, p. 2787–2838, https://doi.org/10.1029/JB094iB03p02787.

Bachmann, F., Hielscher, R., and Schaeben, H., 2011, Grain detection from 2d and 3d EBSD data—Specification of the MTEX algorithm: Ultramicroscopy, v. 111, p. 1720–1733, https://doi.org/10.1016/j.ultramic.2011.08.002.

Betka, P.M., Seeber, L., Thomson, S.N., Steckler, M.S., Sincavage, R., and Zoramthara, C., 2018, Slip-partitioning above a shallow, weak décollement beneath the Indo-Burman accretionary prism: Earth and Planetary Science Letters, v. 503, p. 17–28, https://doi.org/10.1016/j.epsl.2018.09.003.

Bikramaditya, R.K., Chung, S.L., Singh, A.K., Lee, H.Y., Lin, T.H., and Iizuka, Y., 2020, Age and isotope geochemistry of magmatic rocks of the Lohit plutonic complex, eastern Himalaya: Implications for the evolution of Transhimalayan arc magmatism: Journal of the Geological Society, v. 177, p. 379–394, https://doi.org/10.1144/jgs2018-214.

Booth, A.L., Zeitler, P.K., Kidd, W.S., Wooden, J., Liu, Y., Idleman, B., Hren, M., and Chamberlain, C.P., 2004, U–Pb zircon constraints on the tectonic evolution of southeastern Tibet, Namche Barwa area: American Journal of Science, v. 304, p. 889–929, https://doi.org/10.2475/ajs.304.10.889.

Booth, A.L., Chamberlain, C.P., Kidd, W.S., and Zeitler, P.K., 2009, Constraints on the metamorphic evolution of the eastern Himalayan syntaxis from geochronologic and petrologic studies of Namche Barwa: Geological Society of America Bulletin, v. 121, p. 385–407, https://doi.org/10.1130/B26041.1.

Cai, F., Ding, L., Leary, R.J., Wang, H., Xu, Q., Zhang, L., and Yue, Y., 2012, Tectonostratigraphy and provenance of an accretionary complex within the Yarlung–Zangpo suture zone, southern Tibet: Insights into subduction–accretion processes in the Neo-Tethys: Tectonophysics, v. 574–575, p. 181–192, https://doi.org/10.1016/j.tecto.2012.08.016.

Cao, W., Yang, J., Zuza, A.V., Ji, W.Q., Ma, X.X., Chu, X., and Burgess, Q.P., 2020, Crustal tilting and differential exhumation of Gangdese Batholith in southern Tibet revealed by bedrock pressures: Earth and Planetary Science Letters, v. 543, https://doi.org/10.1016/j.epsl.2020.116347.

Catlos, E.J., Harrison, T.M., Kohn, M.J., Grove, M., Ryerson, F.J., Manning, C.E., and Upreti, B.N., 2001, Geochronologic and thermobarometric constraints on the evolution of the Main Central Thrust, central Nepal Himalaya: Journal of Geophysical Research: Solid Earth, v. 106, p. 16,177–16,204, https://doi.org/10.1029/2000JB900375.

Cobbold, P.R., and Davy, P.H., 1988, Indentation tectonics in nature and experiment. 2. Central Asia: Bulletin of the Geological Institutions of the University of Uppsala, v. 14, p. 143–162.

Copeland, P., Harrison, T.M., Yun, P., Kidd, W.S.F., Roden, M., and Zhang, Y., 1995, Thermal evolution of the Gangdese batholith, southern Tibet: A history of episodic unroofing: Tectonics, v. 14, p. 223–236, https://doi.org/10.1029/94TC01676.

Coudurier-Curveur, A., Tapponnier, P., Okal, E., Van der Woerd, J., Kali, E., Choudhury, S., Baruah, S., Etchebed, M., and Karakaş, Ç., 2020, A composite rupture model for the great 1950 Assam earthquake across the cusp of the East Himalayan syntaxis: Earth and Planetary Science Letters, v. 531, https://doi.org/10.1016/j.epsl.2019.115928.

Coulon, C., Maluski, H., Bollinger, C., and Wang, S., 1986, Mesozoic and Cenozoic volcanic rocks from central and southern Tibet: ^{39}Ar-^{40}Ar dating, petrological characteristics and geodynamical significance: Earth and Planetary Science Letters, v. 79, p. 281–302, https://doi.org/10.1016/0012-821X(86)90186-X.

Cross, A.J., Prior, D.J., Stipp, M., and Kidder, S., 2017, The recrystallized grain size piezometer for quartz: An EBSD-based calibration: Geophysical Research Letters, v. 44, p. 6667–6674, https://doi.org/10.1002/2017GL073836.

Dai, J.G., Wang, C.S., Hébert, R., Santosh, M., Li, Y.L., and Xu, J.Y., 2011, Petrology and geochemistry of peridotites in the Zhongba ophiolite, Yarlung Zangbo suture zone: Implications for the Early Cretaceous intra-oceanic subduction zone within the Neo-Tethys: Chemical Geology, v. 288, p. 133–148, https://doi.org/10.1016/j.chemgeo.2011.07.011.

Debon, F., Fort, P.L., Sheppard, S.M., and Sonet, J., 1986, The four plutonic belts of the Transhimalaya-Himalaya: A chemical, mineralogical, isotopic, and chronological synthesis along a Tibet-Nepal section: Journal of Petrology, v. 27, p. 219–250, https://doi.org/10.1093/petrology/27.1.219.

Downloaded from http://pubs.geoscienceworld.org/gsa/gsabulletin/article-pdf/doi/10.1130/B36323.1/5738725/b36323.pdf
by University of Nevada Reno user

DeCelles, P.G., Robinson, D.M., Quade, J., Ojha, T.P., Garzione, C.N., Copeland, P., and Upreti, B.N., 2001, Stratigraphy, structure, and tectonic evolution of the Himalayan fold-thrust belt in western Nepal: Tectonics, v. 20, p. 487–509, https://doi.org/10.1029/2000TC001226.

DeCelles, P.G., Kapp, P., Quade, J., and Gehrels, G.E., 2011, Oligocene–Miocene Kailas basin, southwestern Tibet: Record of postcollisional upper-plate extension in the Indus-Yarlung suture zone: Geological Society of America Bulletin, v. 123, p. 1337–1362, https://doi.org/10.1130/B30258.1.

DeCelles, P.G., Carrapa, B., Gehrels, G.E., Chakraborty, T., and Ghosh, P., 2016, Along-strike continuity of structure, stratigraphy, and kinematic history in the Himalayan thrust belt: The view from Northeastern India: Tectonics, v. 35, p. 2995–3027, https://doi.org/10.1002/2016TC004298.

de Sigoyer, J., Chavagnac, V., Blichert-Toft, J., Villa, I.M., Luais, B., Guillot, S., Cosca, M., and Mascle, G., 2000, Dating the Indian continental subduction and collisional thickening in the northwest Himalaya: Multichronology of the Tso Morari eclogites: Geology, v. 28, p. 487–490, https://doi.org/10.1130/0091-7613(2000)28<487:DTICSA>2.0.CO;2.

Dhoundial, D.P., Santra, D.K., and Dange, M.N., 1971, A new look at the stratigraphic and tectonic importance of Tidding limestone and serpentinite in Lohit district, NEFA: Geological Survey of India Miscellaneous Publication, v. 24, p. 91–114.

Ding, L., Zhong, D., Yin, A., Kapp, P., and Harrison, T.M., 2001, Cenozoic structural and metamorphic evolution of the eastern Himalayan syntaxis (Namche Barwa): Earth and Planetary Science Letters, v. 192, p. 423–438, https://doi.org/10.1016/S0012-821X(01)00463-0.

Ding, L., Kapp, P., Zhong, D., and Deng, W., 2003, Cenozoic volcanism in Tibet: Evidence for a transition from oceanic to continental subduction: Journal of Petrology, v. 44, p. 1833–1865, https://doi.org/10.1093/petrology/egg061.

Ding, L., Kapp, P., and Wan, X., 2005, Paleocene–Eocene record of ophiolite obduction and initial India-Asia collision, south central Tibet: Tectonics, v. 24, no. 3, https://doi.org/10.1029/2004TC001729.

Donaldson, D.G., Webb, A.A.G., Menold, C.A., Kylander-Clark, A.R., and Hacker, B.R., 2013, Petrochronology of Himalayan ultrahigh-pressure eclogite: Geology, v. 41, p. 835–838, https://doi.org/10.1130/G33699.1.

Dunkl, I., Antolín, B., Wemmer, K., Rantitsch, G., Kienast, M., Montomoli, C., Ding, L., Carosi, R., Appel, E., El Bay, R., and Xu, Q., 2011, Metamorphic evolution of the Tethyan Himalayan flysch in SE Tibet: Geological Society, London, Special Publication 353, p. 45–69, https://doi.org/10.1144/SP353.4.

Dupuis, C., Hébert, R., Dubois-Côté, V., Wang, C.S., Li, Y.L., and Li, Z.J., 2005, Petrology and geochemistry of mafic rocks from mélange and flysch units adjacent to the Yarlung Zangbo suture zone, southern Tibet: Chemical Geology, v. 214, p. 287–308, https://doi.org/10.1016/j.chemgeo.2004.10.005.

Dürr, S.B., 1996, Provenance of Xigaze fore-arc basin clastic rocks (Cretaceous, south Tibet): Geological Society of America Bulletin, v. 108, p. 669–684, https://doi.org/10.1130/0016-7606(1996)108<0669:POXFAB>2.3.CO;2.

Dutt, A., Singh, A.K., Srivastava, R.K., and Oinam, G., 2021a, Evidence of melt—and fluid—rock interactions in the refractory forearc peridotites and associated mafic intrusives from the Tuting–Tidding ophiolites, eastern Himalaya, India: Petrogenetic and tectonic implications: Geological Journal, v. 56, p. 2082–2110, https://doi.org/10.1002/gj.4043.

Dutt, A., Singh, A.K., Srivastava, R.K., Oinam, G., and Bikramaditya, R.K., 2021b, Geochemical and metamorphic record of the amphibolites from the Tuting–Tidding suture zone ophiolites, eastern Himalaya, India: Implications for the presence of a dismembered metamorphic sole: Geological Magazine, v. 158, p. 787–810, https://doi.org/10.1017/S0016756820000825.

Einsele, G., Liu, B., Dürr, S., Frisch, W., Liu, G., Luterbacher, H.P., Ratschbacher, L., Ricken, W., Wendt, J., Wetzel, A., and Yu, G., 1994, The Xigaze forearc basin: Evolution and facies architecture (Cretaceous, Tibet): Sedimentary Geology, v. 90, p. 1–32, https://doi.org/10.1016/0037-0738(94)90014-0.

England, P., and Houseman, G., 1986, Finite strain calculations of continental deformation 2. Comparison with the India-Asia collision zone: Journal of Geophysical Research: Solid Earth, v. 91, p. 3664–3676, https://doi.org/10.1029/JB091iB03p03664.

Gansser, A., 1964, Geology of the Himalayas: New York, Wiley Interscience, 289 p.

Garzanti, E., and Van Haver, T., 1988, The Indus clastics: Forearc basin sedimentation in the Ladakh Himalaya (India): Sedimentary Geology, v. 59, p. 237–249, https://doi.org/10.1016/0037-0738(88)90078-4.

Ghosh, B., and Ray, J., 2003a, Mineral chemistry of ophiolitic rocks of Mayodia-Hunli area of Dibang Valley district, Arunachal Pradesh, North Eastern India: Memoirs of the Geological Society of India, v. 52, p. 447–471.

Ghosh, B., and Ray, J., 2003b, Petrology of the ophiolitic assemblage around Mayodia, Dibang Valley district, Arunachal Pradesh, north-eastern India: Indian Minerals, v. 57, p. 39–52.

Ghosh, B., Mahoney, J., and Ray, J., 2007, Mayodia Ophiolites of Arunachal Pradesh, Northeastern Himalaya: Journal of the Geological Society of India, v. 70, p. 595.

Gong, J., Ji, J., Zhou, J., Tu, J., Sun, D., Zhong, D., and Han, B., 2015, Late Miocene thermal evolution of the eastern Himalayan syntaxis as constrained by biotite $^{40}Ar/^{39}Ar$ thermochronology: The Journal of Geology, v. 123, p. 369–384, https://doi.org/10.1086/682951.

Goswami, T.K., 2013, Subduction related magmatism: Constrains from the REE pattern in the Lohit Batholith, Arunachal Pradesh, India: Geosciences, v. 3, p. 128–141.

Govin, G., van der Beek, P., Najman, Y., Millar, I., Gemignani, L., Huyghe, P., Dupont-Nivet, G., Bernet, M., Mark, C., and Wijbrans, J., 2020, Early onset and late acceleration of rapid exhumation in the Namche Barwa syntaxis, eastern Himalaya: Geology, v. 48, p. 1139–1143, https://doi.org/10.1130/G47720.1.

Grove, M., and Harrison, T.M., 1996, $^{40}Ar^*$ diffusion in Fe-rich biotite: The American Mineralogist, v. 81, p. 940–951, https://doi.org/10.2138/am-1996-7-816.

Gururajan, N.S., and Choudhuri, B.K., 2003, Geology and tectonic history of the Lohit Valley, Eastern Arunachal Pradesh, India: Journal of Asian Earth Sciences, v. 21, p. 731–741, https://doi.org/10.1016/S1367-9120(02)00040-8.

Gururajan, N.S., and Choudhuri, B.K., 2007, Geochemistry and tectonic implications of the Trans-Himalayan Lohit plutonic complex, eastern Arunachal Pradesh: Journal of the Geological Society of India, v. 70, p. 17–33.

Hames, W.E., and Bowring, S.A., 1994, An empirical evaluation of the argon diffusion geometry in muscovite: Earth and Planetary Science Letters, v. 124, p. 161–169, https://doi.org/10.1016/0012-821X(94)00079-4.

Haproff, P.J., Zuza, A.V., and Yin, A., 2018, West-directed thrusting south of the eastern Himalayan syntaxis indicates clockwise crustal flow at the indenter corner during the India-Asia collision: Tectonophysics, v. 722, p. 277–285, https://doi.org/10.1016/j.tecto.2017.11.001.

Haproff, P.J., Zuza, A.V., Yin, A., Harrison, T.M., Manning, C.M., Ding, L., Wu, C., Chen, J., and Dubey, C.S., 2019, Geologic framework of the northern Indo-Burma Ranges: Lateral correlation of Himalayan-Tibetan lithologic units across the eastern Himalayan syntaxis: Geosphere, v. 15, p. 856–881, https://doi.org/10.1130/GES02054.1.

Haproff, P.J., Odlum, M.L., Zuza, A.V., Yin, A., and Stockli, D.F., 2020, Structural and thermochronologic constraints on the Cenozoic tectonic development of the northern Indo-Burma Ranges: Tectonics, v. 39, no. 9, https://doi.org/10.1029/2020TC006231.

Harrison, T.M., and Lovera, O.M., 2014, The multi-diffusion domain model: Past, present and future, *in* Jourdan, F., Mark, D.F., and Verati, C., $^{40}Ar/^{39}Ar$ Dating: From Archaeology to Planetary Sciences: Geological Society, London, Special Publication 378, p. 91–106, https://doi.org/10.1144/SP378.9.

Harrison, T.M., Duncan, I., and McDougall, I., 1985, Diffusion of ^{40}Ar in biotite: Temperature, pressure and compositional effects: Geochimica et Cosmochimica Acta, v. 49, p. 2461–2468, https://doi.org/10.1016/0016-7037(85)90246-7.

Harrison, T.M., Copeland, P., Kidd, W.S.F., and Yin, A., 1992, Raising Tibet: Science, v. 255, p. 1663–1670, https://doi.org/10.1126/science.255.5052.1663.

Harrison, T.M., Yin, A., Grove, M., Lovera, O.M., Ryerson, F.J., and Zhou, X., 2000, The Zedong Window: A record of superposed Tertiary convergence in southeastern Tibet: Journal of Geophysical Research: Solid Earth, v. 105, p. 19,211–19,230, https://doi.org/10.1029/2000JB900078.

Harrison, T.M., Célérier, J., Aikman, A.B., Hermann, J., and Heizler, M.T., 2009, Diffusion of ^{40}Ar in muscovite: Geochimica et Cosmochimica Acta, v. 73, p. 1039–1051, https://doi.org/10.1016/j.gca.2008.09.038.

He, S., Kapp, P., DeCelles, P.G., Gehrels, G.E., and Heizler, M., 2007, Cretaceous–Tertiary geology of the Gangdese Arc in the Linzhou area, southern Tibet: Tectonophysics, v. 433, p. 15–37, https://doi.org/10.1016/j.tecto.2007.01.005.

Hébert, R., Bezard, R., Guilmette, C., Dostal, J., Wang, C.S., and Liu, Z.F., 2012, The Indus-Yarlung Zangbo ophiolites from Nanga Parbat to Namche Barwa syntaxes, southern Tibet: First synthesis of petrology, geochemistry, and geochronology with incidences on geodynamic reconstructions of Neo-Tethys: Gondwana Research, v. 22, p. 377–397, https://doi.org/10.1016/j.gr.2011.10.013.

Heim, A., and Gansser, A., 1939, Central Himalaya: Delhi, Hindustan Publishing.

Hirth, G., Teyssier, C., and Dunlap, J.W., 2001, An evaluation of quartzite flow laws based on comparisons between experimentally and naturally deformed rocks: International Journal of Earth Sciences, v. 90, p. 77–87, https://doi.org/10.1007/s005310000152.

Hodges, K.V., 2000, Tectonics of the Himalaya and southern Tibet from two perspectives: Geological Society of America Bulletin, v. 112, p. 324–350, https://doi.org/10.1130/0016-7606(2000)112<324:TOTHAS>2.0.CO;2.

Holland, T., and Blundy, J., 1994, Non-ideal interactions in calcic amphiboles and their bearing on amphibole-plagioclase thermometry: Contributions to Mineralogy and Petrology, v. 116, p. 433–447, https://doi.org/10.1007/BF00310910.

Holland, T., and Powell, R., 1998, An internally consistent thermodynamic data set for phases of petrological interest: Journal of Metamorphic Geology, v. 16, p. 309–343, https://doi.org/10.1111/j.1525-1314.1998.00140.x.

Ismaïl, W.B., and Mainprice, D., 1998, An olivine fabric database: An overview of upper mantle fabrics and seismic anisotropy: Tectonophysics, v. 296, p. 145–157, https://doi.org/10.1016/S0040-1951(98)00141-3.

Jackson, S.E., Pearson, N.J., Griffin, W.L., and Belousova, E.A., 2004, The application of laser ablation–inductively coupled plasma–mass spectrometry to in situ U–Pb zircon geochronology: Chemical Geology, v. 211, p. 47–69, https://doi.org/10.1016/j.chemgeo.2004.06.017.

Ji, W.Q., Wu, F.Y., Chung, S.L., Li, J.X., and Liu, C.Z., 2009, Zircon U–Pb geochronology and Hf isotopic constraints on petrogenesis of the Gangdese batholith, southern Tibet: Chemical Geology, v. 262, p. 229–245, https://doi.org/10.1016/j.chemgeo.2009.01.020.

Kapp, P., and DeCelles, P.G., 2019, Mesozoic–Cenozoic geological evolution of the Himalayan-Tibetan orogen and working tectonic hypotheses: American Journal of Science, v. 319, p. 159–254, https://doi.org/10.2475/03.2019.01.

Kellett, D.A., Cottle, J.M., and Larson, K.P., 2019, The South Tibetan Detachment System: History, advances, definition and future directions: Geological Society, London, Special Publication 483, p. 377–400, https://doi.org/10.1144/SP483.2.

Kruhl, J.H., 1996, Prism-and basal-plane parallel subgrain boundaries in quartz: A microstructural geothermobarometer: Journal of Metamorphic Geology, v. 14, p. 581–589, https://doi.org/10.1046/j.1525-1314.1996.00413.x.

Laskowski, A.K., Kapp, P., Vervoort, J.D., and Ding, L., 2016, High-pressure Tethyan Himalaya rocks along the

Downloaded from http://pubs.geoscienceworld.org/gsa/gsabulletin/article-pdf/doi/10.1130/B36323.1/5738725/b36323.pdf
by University of Nevada Reno user

India-Asia suture zone in southern Tibet: Lithosphere, v. 8, p. 574–582, https://doi.org/10.1130/L544.1.

Laskowski, A.K., Kapp, P., and Cai, F., 2018, Gangdese culmination model: Oligocene–Miocene duplexing along the India-Asia suture zone, Lazi region, southern Tibet: Geological Society of America Bulletin, v. 130, p. 1355–1376, https://doi.org/10.1130/B31834.1.

Law, R.D., 2014, Deformation thermometry based on quartz c-axis fabrics and recrystallization microstructures: A review: Journal of Structural Geology, v. 66, p. 129–161, https://doi.org/10.1016/j.jsg.2014.05.023.

Law, R.D., Schmid, S.M., and Wheeler, J., 1990, Simple shear deformation and quartz crystallographic fabrics: A possible natural example from the Torridon area of NW Scotland: Journal of Structural Geology, v. 12, p. 29–45, https://doi.org/10.1016/0191-8141(90)90046-2.

Law, R.D., Searle, M.P., and Simpson, R.L., 2004, Strain, deformation temperatures and vorticity of flow at the top of the Greater Himalayan Slab, Everest Massif, Tibet: Journal of the Geological Society, v. 161, p. 305–320, https://doi.org/10.1144/0016-764903-047.

Leary, R., Orme, D.A., Laskowski, A.K., DeCelles, P.G., Kapp, P., Carrapa, B., and Dettinger, M., 2016, Along-strike diachroneity in deposition of the Kailas Formation in central southern Tibet: Implications for Indian slab dynamics: Geosphere, v. 12, p. 1198–1223, https://doi.org/10.1130/GES01325.1.

Lee, H.Y., Chung, S.L., Wang, J.R., Wen, D.J., Lo, C.H., Yang, T.F., Zhang, Y., Xie, Y., Lee, T.Y., Wu, G., and Ji, J., 2003, Miocene Jiali faulting and its implications for Tibetan tectonic evolution: Earth and Planetary Science Letters, v. 205, p. 185–194, https://doi.org/10.1016/S0012-821X(02)01040-3.

Lee, H.Y., Chung, S.L., Lo, C.H., Ji, J., Lee, T.Y., Qian, Q., and Zhang, Q., 2009, Eocene Neotethyan slab breakoff in southern Tibet inferred from the Linzizong volcanic record: Tectonophysics, v. 477, p. 20–35, https://doi.org/10.1016/j.tecto.2009.02.031.

Le Fort, P., 1975, Himalayas: The collided range. Present knowledge of the continental arc: American Journal of Science, v. 275, p. 1–44.

Li, Z.H., Xu, Z., Gerya, T., and Burg, J.P., 2013, Collision of continental corner from 3-D numerical modeling: Earth and Planetary Science Letters, v. 380, p. 98–111, https://doi.org/10.1016/j.epsl.2013.08.034.

Lin, T.H., Lo, C.H., Chung, S.L., Hsu, F.J., Yeh, M.W., Lee, T.Y., Ji, J.Q., Wang, Y.Z., and Liu, D., 2009, $^{40}Ar/^{39}Ar$ dating of the Jiali and Gaoligong shear zones: Implications for crustal deformation around the eastern Himalayan syntaxis: Journal of Asian Earth Sciences, v. 34, p. 674–685, https://doi.org/10.1016/j.jseaes.2008.10.009.

Lin, T.H., Chung, S.L., Kumar, A., Wu, F.Y., Chiu, H.Y., and Lin, I., 2013, Linking a prolonged Neo-Tethyan magmatic arc in South Asia: Zircon U-Pb and Hf isotopic constraints from the Lohit Batholith, NE India: Terra Nova, v. 25, p. 453–458, https://doi.org/10.1111/ter.12056.

Liu, Y., Tan, X., Ye, Y., Zhou, C., Lu, R., Murphy, M.A., Xu, X., and Suppe, J., 2020, Role of erosion in creating thrust recesses in a critical-taper wedge: An example from Eastern Tibet: Earth and Planetary Science Letters, v. 540, https://doi.org/10.1016/j.epsl.2020.116270.

Long, S., McQuarrie, N., Tobgay, T., and Grujic, D., 2011, Geometry and crustal shortening of the Himalayan fold-thrust belt, eastern and central Bhutan: Geological Society of America Bulletin, v. 123, p. 1427–1447, https://doi.org/10.1130/B30203.1.

Mainprice, D., Bachmann, F., Hielscher, R., Schaeben, H., and Lloyd, G.E., 2015, Calculating anisotropic piezoelectric properties from texture data using the MTEX open source package, *in* Faulkner, D.R., Mariani, E., and Mecklenburgh, J., Rock Deformation from Field, Experiments and Theory: A Volume in Honour of Ernie Rutter: Geological Society, London, Special Publication 409, p. 223–249, https://doi.org/10.1144/SP409.2.

Malpas, J., Zhou, M.F., Robinson, P.T., and Reynolds, P.H., 2003, Geochemical and geochronological constraints on the origin and emplacement of the Yarlung Zangbo ophiolites, Southern Tibet, *in* Dilek, Y., and Robinson, P.T., eds., Ophiolites in Earth History: Geological Society, London, Special Publication 218, p. 191–206, https://doi.org/10.1144/GSL.SP.2003.218.01.11.

Maurin, T., and Rangin, C., 2009, Structure and kinematics of the Indo-Burmese Wedge: Recent and fast growth of the outer wedge: Tectonics, v. 28, no. 2, https://doi.org/10.1029/2008TC002276.

McDermid, I.R., Aitchison, J.C., Davis, A.M., Harrison, T.M., and Grove, M., 2002, The Zedong terrane: A Late Jurassic intra-oceanic magmatic arc within the Yarlung–Tsangpo suture zone, southeastern Tibet: Chemical Geology, v. 187, p. 267–277, https://doi.org/10.1016/S0009-2541(02)00040-2.

McQuarrie, N., Robinson, D., Long, S., Tobgay, T., Grujic, D., Gehrels, G., and Ducea, M., 2008, Preliminary stratigraphic and structural architecture of Bhutan: Implications for the along strike architecture of the Himalayan system: Earth and Planetary Science Letters, v. 272, p. 105–117, https://doi.org/10.1016/j.epsl.2008.04.030.

Meigs, A.J., Burbank, D.W., and Beck, R.A., 1995, Middle–late Miocene (>10 Ma) formation of the Main Boundary thrust in the western Himalaya: Geology, v. 23, p. 423–426, https://doi.org/10.1130/0091-7613(1995)023<0423:MLMMFO>2.3.CO;2.

Michels, Z.D., Kruckenberg, S.C., Davis, J.R., and Tikoff, B., 2015, Determining vorticity axes from grain-scale dispersion of crystallographic orientations: Geology, v. 43, p. 803–806, https://doi.org/10.1130/G36868.1.

Misra, D.K., 2009, Litho-tectonic sequence and their regional correlation along the Lohit and Dibang valleys, eastern Arunachal Pradesh: Journal of the Geological Society of India, v. 73, p. 213–219, https://doi.org/10.1007/s12594-009-0077-x.

Misra, D.K., and Singh, T., 2002, Tectonic setting and neotectonic features along the Eastern Syntaxial Bend (Lohit and Dibang), Arunachal Himalaya, *in* Pant, C.C., and Sharma, A.K., Aspects of Geology and Environment of the Himalaya: Nainital, India, Gyanodaya Prakashan, p. 19–40.

Mitra, G., Bhattacharyya, K., and Mukul, M., 2010, The Lesser Himalayan duplex in Sikkim: Implications for variations in Himalayan shortening: Journal of the Geological Society of India, v. 75, p. 289–301, https://doi.org/10.1007/s12594-010-0016-x.

Molnar, P., and Tapponnier, P., 1975, Cenozoic tectonics of Asia: Effects of a continental collision: Science, v. 189, p. 419–426, https://doi.org/10.1126/science.189.4201.419.

Morley, C.K., Naing, T.T., Searle, M., and Robinson, S.A., 2020, Structural and tectonic development of the Indo-Burma ranges: Earth-Science Reviews, v. 200, https://doi.org/10.1016/j.earscirev.2019.102992.

Mukhopadhyay, B., and Dasgupta, S., 2015, Earthquake swarms near eastern Himalayan syntaxis along Jiali Fault in Tibet: A seismotectonic appraisal: Geoscience Frontiers, v. 6, p. 715–722, https://doi.org/10.1016/j.gsf.2014.12.009.

Murphy, M.A., and Yin, A., 2003, Structural evolution and sequence of thrusting in the Tethyan fold-thrust belt and Indus-Yalu suture zone, southwest Tibet: Geological Society of America Bulletin, v. 115, p. 21–34, https://doi.org/10.1130/0016-7606(2003)115<0021:SEASOT>2.0.CO;2.

Nandy, D.R., 1973, Geology and structural lineaments of the Lohit Himalaya (Arunachal Pradesh) and adjoining area, *in* Seminar on Geodynamics of the Himalayan Region: Hyderabad, National Geophysical Research Institute, p. 167–172.

Nandy, D.R., 1976, The Assam syntaxis of the Himalayas-A reinterpretation: Geological Survey of India Miscellaneous Publication 24, p. 363–367.

Neumann, B., 2000, Texture development of recrystallised quartz polycrystals unravelled by orientation and misorientation characteristics: Journal of Structural Geology, v. 22, p. 1695–1711, https://doi.org/10.1016/S0191-8141(00)00060-2.

Ni, J., and York, J.E., 1978, Late Cenozoic tectonics of the Tibetan plateau: Journal of Geophysical Research: Solid Earth, v. 83, p. 5377–5384, https://doi.org/10.1029/JB083iB11p05377.

Nielsen, C., Chamot-Rooke, N., and Rangin, C., 2004, From partial to full strain partitioning along the Indo-Burmese hyper-oblique subduction: Marine Geology, v. 209, p. 303–327, https://doi.org/10.1016/j.margeo.2004.05.001.

Ningthoujam, P.S., Dubey, C.S., Lolee, L.K., Shukla, D.P., Naorem, S.S., and Singh, S.K., 2015, Tectonic studies and crustal shortening across Easternmost Arunachal Himalaya: Journal of Asian Earth Sciences, v. 111, p. 339–349, https://doi.org/10.1016/j.jseaes.2015.07.003.

Orme, D.A., Carrapa, B., and Kapp, P., 2015, Sedimentology, provenance and geochronology of the Upper Cretaceous–Lower Eocene western Xigaze forearc basin, southern Tibet: Basin Research, v. 27, p. 387–411, https://doi.org/10.1111/bre.12080.

Paton, C., Woodhead, J.D., Hellstrom, J.C., Hergt, J.M., Greig, A., and Maas, R., 2010, Improved laser ablation U–Pb zircon geochronology through robust downhole fractionation correction: Geochemistry, Geophysics, Geosystems, v. 11, no. 3, https://doi.org/10.1029/2009GC002618.

Pearce, J.A., Harris, N.B., and Tindle, A.G., 1984, Trace element discrimination diagrams for the tectonic interpretation of granitic rocks: Journal of Petrology, v. 25, p. 956–983, https://doi.org/10.1093/petrology/25.4.956.

Pebam, J., and Kamalakannan, D., 2019, Petrogenesis and emplacement of magmatic rocks of Lohit Plutonic Complex, Arunachal Trans-Himalaya, Northeast India: Indian Journal of Geosciences, v. 73, p. 213–230.

Petrus, J.A., and Kamber, B.S., 2012, VizualAge: A novel approach to laser ablation ICP-MS U–Pb geochronology data reduction: Geostandards and Geoanalytical Research, v. 36, p. 247–270, https://doi.org/10.1111/j.1751-908X.2012.00158.x.

Piette-Lauzière, N., Larson, K.P., Kellett, D.A., and Graziani, R., 2020, Intracrystalline vorticity record of flow kinematics during shear zone reactivation: Journal of Structural Geology, v. 140, https://doi.org/10.1016/j.jsg.2020.104134.

Profeta, L., Ducea, M.N., Chapman, J.B., Paterson, S.R., Gonzales, S.M.H., Kirsch, M., Petrescu, L., and DeCelles, P.G., 2015, Quantifying crustal thickness over time in magmatic arcs: Scientific Reports, v. 5, https://www.doi.org/10.1038/srep17786.

Quanru, G., Guitang, P., Zheng, L., Chen, Z., Fisher, R.D., Sun, Z., Ou, C., Dong, H., Wang, X., Li, S., and Lou, X., 2006, The Eastern Himalayan syntaxis: Major tectonic domains, ophiolitic mélanges and geologic evolution: Journal of Asian Earth Sciences, v. 27, p. 265–285, https://doi.org/10.1016/j.jseaes.2005.03.009.

Quidelleur, X., Grove, M., Lovera, O.M., Harrison, T.M., and Yin, A., 1997, Thermal evolution and slip history of the Renbu-Zedong Thrust, southeastern Tibet: Journal of Geophysical Research: Solid Earth, v. 102, p. 2659–2679, https://doi.org/10.1029/96JB02483.

Rangin, C., Maurin, T., and Masson, F., 2013, Combined effects of Eurasia/Sunda oblique convergence and East-Tibetan crustal flow on the active tectonics of Burma: Journal of Asian Earth Sciences, v. 76, p. 185–194, https://doi.org/10.1016/j.jseaes.2013.05.018.

Ratschbacher, L., Frisch, W., Liu, G., and Chen, C., 1994, Distributed deformation in southern and western Tibet during and after the India-Asia collision: Journal of Geophysical Research: Solid Earth, v. 99, p. 19,917–19,945, https://doi.org/10.1029/94JB00932.

Reiners, P.W., 2005, Zircon (U-Th)/He thermochronometry: Reviews in Mineralogy and Geochemistry, v. 58, p. 151–179, https://doi.org/10.2138/rmg.2005.58.6.

Robinson, D.M., DeCelles, P.G., Garzione, C.N., Pearson, O.N., Harrison, T.M., and Catlos, E.J., 2003, Kinematic model for the Main Central thrust in Nepal: Geology, v. 31, p. 359–362, https://doi.org/10.1130/0091-7613(2003)031<0359:KMFTMC>2.0.CO;2.

Royden, L.H., Burchfiel, B.C., King, R.W., Wang, E., Chen, Z., Shen, F., and Liu, Y., 1997, Surface deformation and lower crustal flow in eastern Tibet: Science, v. 276, p. 788–790, https://doi.org/10.1126/science.276.5313.788.

Ryan, W.B., Carbotte, S.M., Coplan, J.O., O'Hara, S., Melkonian, A., Arko, R., Weissel, R.A., Ferrini, V., Goodwillie, A., Nitsche, F., and Bonczkowski, J., 2009, Global multi-resolution topography synthesis: Geochemistry, Geophysics, Geosystems, v. 10, no. 3, https://doi.org/10.1029/2008GC002332.

Saha, P., Acharyya, S.K., Balaram, V., and Roy, P., 2012, Geochemistry and tectonic setting of Tuting metavolcanic

Downloaded from http://pubs.geoscienceworld.org/gsa/gsabulletin/article-pdf/doi/10.1130/B36323.1/5738725/b36323.pdf
by University of Nevada Reno user

rocks of possible ophiolitic affinity from eastern Himalayan syntaxis: Journal of the Geological Society of India, v. 80, p. 167–176, https://doi.org/10.1007/s12594-012-0129-5.

Saleeby, J., Ducea, M., and Clemens-Knott, D., 2003, Production and loss of high-density batholithic root, southern Sierra Nevada, California: Tectonics, v. 22, no. 6, https://doi.org/10.1029/2002TC001374.

Salvi, D., Mathew, G., Kohn, B., Pande, K., and Borgohain, B., 2020, Thermochronological insights into the thermotectonic evolution of Mishmi hills across the Dibang Valley, NE Himalayan syntaxis: Journal of Asian Earth Sciences, v. 190, https://doi.org/10.1016/j.jseaes.2019.104158.

Sarma, K.P., Nandy, S., and Mazumdar, N., 2012, Structural studies of the Mishmi block in parts of Dibang Valley of Arunachal Himalaya, Northeast India: International Journal of Geology: Earth and Environmental Sciences, v. 2, p. 43–56.

Schärer, U., Xu, R.H., and Allègre, C.J., 1984, U–Pb geochronology of Gangdese (Transhimalaya) plutonism in the Lhasa-Xigaze region, Tibet: Earth and Planetary Science Letters, v. 69, p. 311–320, https://doi.org/10.1016/0012-821X(84)90190-0.

Schlup, M., Carter, A., Cosca, M., and Steck, A., 2003, Exhumation history of eastern Ladakh revealed by $^{40}Ar/^{39}Ar$ and fission-track ages: The Indus River–Tso Morari transect, NW Himalaya: Journal of the Geological Society, v. 160, p. 385–399, https://doi.org/10.1144/0016-764902-084.

Schmid, S.M., and Casey, M., 1986, Complete fabric analysis of some commonly observed quartz c-axis patterns: Geophysical Monograph, v. 36, p. 263–286, https://doi.org/10.1029/GM036p0263.

Sharma, K.K., Choubey, V.M., and Chatti, H.R., 1991, Geological setting of the ophiolites and magmatic arc of the Lohit Himalaya (Arunachal Pradesh), India with special reference to their petrochemistry: Physics and Chemistry of the Earth, v. 18, p. 277–292, https://doi.org/10.1016/0079-1946(91)90005-Z.

Singh, A.K., and Singh, R.B., 2011, Zn-and Mn-rich chromespinels in serpentinite of Tidding suture zone, eastern Himalaya and their metamorphism and genetic significance: Current Science, v. 100, p. 743–749.

Singh, A.K., and Singh, R.B., 2013, Genetic implications of Zn-and Mn-rich Cr-spinels in serpentinites of the Tidding suture zone, eastern Himalaya, NE India: Geological Journal, v. 48, p. 22–38, https://doi.org/10.1002/gj.2428.

Skemer, P., Katayama, I., Jiang, Z., and Karato, S.I., 2005, The misorientation index: Development of a new method for calculating the strength of lattice-preferred orientation: Tectonophysics, v. 411, p. 157–167, https://doi.org/10.1016/j.tecto.2005.08.023.

Sláma, J., Košler, J., Condon, D.J., Crowley, J.L., Gerdes, A., Hanchar, J.M., Horstwood, M.S., Morris, G.A., Nasdala, L., Norberg, N., and Schaltegger, U., 2008, Plešovice zircon—a new natural reference material for U–Pb and Hf isotopic microanalysis: Chemical Geology, v. 249, p. 1–35, https://doi.org/10.1016/j.chemgeo.2007.11.005.

Stacey, J.T., and Kramers, J.D., 1975, Approximation of terrestrial lead isotope evolution by a two-stage model: Earth and Planetary Science Letters, v. 26, p. 207–221, https://doi.org/10.1016/0012-821X(75)90088-6.

Starnes, J.K., Long, S.P., Gordon, S.M., Zhang, J., and Soignard, E., 2020, Using quartz fabric intensity parameters to delineate strain patterns across the Himalayan Main Central thrust: Journal of Structural Geology, v. 131, https://doi.org/10.1016/j.jsg.2019.103941.

Stipp, M., Stünitz, H., Heilbronner, R., and Schmid, S.M., 2002, Dynamic recrystallization of quartz: Correlation between natural and experimental conditions, *in* DeMeer, S., Drury, M.R., DeBresser, J.H.P., and Pennock, G.M., eds., Deformation Mechanisms, Rheology and Tectonics: Current Status and Future Perspectives: Geological Society, London, Special Publication 200, p. 171–190, https://doi.org/10.1144/GSL.SP.2001.200.01.11.

Sundell, K.E., Laskowski, A.K., Kapp, P.A., Ducea, M.N., and Chapman, J.B., 2021, Jurassic to Neogene quantitative crustal thickness estimates in southern Tibet: GSA Today, v. 31, p. 4–10, https://doi.org/10.1130/GSATG461A.1.

Tapponnier, P., and Molnar, P., 1977, Active faulting and tectonics in China: Journal of Geophysical Research: Solid Earth and Planets, v. 82, p. 2905–2930, https://doi.org/10.102z9/JB082i020p02905.

Thakur, V.C., and Jain, A.K., 1974, Tectonics of the region of eastern Himalayan syntaxis: Current Science, v. 43, p. 783–785.

Thakur, V.C., and Jain, A.K., 1975, Some observations of deformation and metamorphism in the rocks of some parts of Mishmi Hills, Lohit district, (NEFA), Arunachal Pradesh: Himalayan Geology, v. 5, p. 339–364.

Thingbaijam, K.K.S., Nath, S.K., Yadav, A., Raj, A., Walling, M.Y., and Mohanty, W.K., 2008, Recent seismicity in Northeast India and its adjoining region: Journal of Seismology, v. 12, p. 107–123, https://doi.org/10.1007/s10950-007-9074-y.

Vermeesch, P., 2018, IsoplotR: A free and open toolbox for geochronology: Geoscience Frontiers, v. 9, p. 1479–1493, https://doi.org/10.1016/j.gsf.2018.04.001.

Vollmer, F.W., 1990, An application of eigenvalue methods to structural domain analysis: Geological Society of America Bulletin, v. 102, p. 786–791, https://doi.org/10.1130/0016-7606(1990)102<0786:AAOEMT>2.3.CO;2.

Wang, C., Li, X., Liu, Z., Li, Y., Jansa, L., Dai, J., and Wei, Y., 2012, Revision of the Cretaceous–Paleogene stratigraphic framework, facies architecture and provenance of the Xigaze forearc basin along the Yarlung Zangbo suture zone: Gondwana Research, v. 22, p. 415–433, https://doi.org/10.1016/j.gr.2011.09.014.

Wang, C., Ding, L., Zhang, L.Y., Kapp, P., Pullen, A., and Yue, Y.H., 2016, Petrogenesis of Middle–Late Triassic volcanic rocks from the Gangdese belt, southern Lhasa terrane: Implications for early subduction of Neo-Tethyan oceanic lithosphere: Lithos, v. 262, p. 320–333, https://doi.org/10.1016/j.lithos.2016.07.021.

Wang, E., Kamp, P.J., Xu, G., Hodges, K.V., Meng, K., Chen, L., Wang, G., and Luo, H., 2015, Flexural bending of southern Tibet in a retro foreland setting: Scientific Reports, v. 5, p. 1–9, https://doi.org/10.1038/srep12076.

Wang, Y., Fan, W., Zhang, Y., Peng, T., Chen, X., and Xu, Y., 2006, Kinematics and $^{40}Ar/^{39}Ar$ geochronology of the Gaoligong and Chongshan shear systems, western Yunnan, China: Implications for early Oligocene tectonic extrusion of SE Asia: Tectonophysics, v. 418, p. 235–254, https://doi.org/10.1016/j.tecto.2006.02.005.

Wang, Y., Sieh, K., Tun, S.T., Lai, K.Y., and Myint, T., 2014, Active tectonics and earthquake potential of the Myanmar region: Journal of Geophysical Research: Solid Earth, v. 119, p. 3767–3822, https://doi.org/10.1002/2013JB010762.

Webb, A.A.G., Guo, H., Clift, P.D., Husson, L., Müller, T., Costantino, D., Yin, A., Xu, Z., Cao, H., and Wang, Q., 2017, The Himalaya in 3-D: Slab dynamics controlled mountain building and monsoon intensification: Lithosphere, v. 9, p. 637–651, https://doi.org/10.1130/L636.1.

Wen, D.R., Liu, D., Chung, S.L., Chu, M.F., Ji, J., Zhang, Q., Song, B., Lee, T.Y., Yeh, M.W., and Lo, C.H., 2008, Zircon SHRIMP U–Pb ages of the Gangdese batholith and implications for Neotethyan subduction in southern Tibet: Chemical Geology, v. 252, p. 191–201, https://doi.org/10.1016/j.chemgeo.2008.03.003.

Wenk, H.R., and Wilde, W.R., 1972, Orientation Distribution Diagrams for Three Yule Marble Fabrics: Washington, D.C., American Geophysical Union Geophysical Monograph Series, v. 16, p. 83–94, https://doi.org/10.1029/GM016p0083.

Wiedenbeck, M.A.P.C., Alle, P., Corfu, F., Griffin, W.L., Meier, M., Oberli, F.V., Quadt, A.V., Roddick, J.C., and Spiegel, W., 1995, Three natural zircon standards for U-Th-Pb, Lu-Hf, trace element and REE analyses: Geostandards Newsletter, v. 19, p. 1–23, https://doi.org/10.1111/j.1751-908X.1995.tb00147.x.

Wiesmayr, G., and Grasemann, B., 2002, Eohimalayan fold and thrust belt: Implications for the geodynamic evolution of the NW-Himalaya (India): Tectonics, v. 21, p. 8-1–8-18, https://www.doi.org/10.1029/2002TC001363.

Wilke, F.D., O'Brien, P.J., Gerdes, A., Timmerman, M.J., Sudo, M., and Ahmed Khan, M., 2010, The multistage exhumation history of the Kaghan Valley UHP series, NW Himalaya, Pakistan from U–Pb and $^{40}Ar/^{39}Ar$ ages: European Journal of Mineralogy, v. 22, p. 703–719, https://doi.org/10.1127/0935-1221/2010/0022-2051.

Williams, H., Prince, C., Argles, T., and Harris, N.B.W., 2001, Thermal evolution of the Himalayan metamorphic belt, Garhwal, India: Constraints from $^{40}Ar–^{39}Ar$ and Sm–Nd data: Journal of Asian Earth Sciences, v. 19, p. 75.

Woodcock, N.H., 1977, Specification of fabric shapes using an eigenvalue method: Geological Society of America Bulletin, v. 88, p. 1231–1236, https://doi.org/10.1130/0016-7606(1977)88<1231:SOFSUA>2.0.CO;2.

Xu, W.C., Zhang, H.F., Harris, N., Guo, L., Pan, F.B., and Wang, S., 2013, Geochronology and geochemistry of Mesoproterozoic granitoids in the Lhasa terrane, south Tibet: Implications for the early evolution of Lhasa terrane: Precambrian Research, v. 236, p. 46–58, https://doi.org/10.1016/j.precamres.2013.07.016.

Yin, A., 2006, Cenozoic tectonic evolution of the Himalayan orogen as constrained by along-strike variation of structural geometry, exhumation history, and foreland sedimentation: Earth-Science Reviews, v. 76, p. 1–131, https://doi.org/10.1016/j.earscirev.2005.05.004.

Yin, A., and Harrison, T.M., 2000, Geologic evolution of the Himalayan-Tibetan orogen: Annual Review of Earth and Planetary Sciences, v. 28, p. 211–280, https://doi.org/10.1146/annurev.earth.28.1.211.

Yin, A., Harrison, T.M., Ryerson, F.J., Wenji, C., Kidd, W.S.F., and Copeland, P., 1994, Tertiary structural evolution of the Gangdese thrust system, southeastern Tibet: Journal of Geophysical Research: Solid Earth, v. 99, p. 18,175–18,201, https://doi.org/10.1029/94JB00504.

Yin, A., Harrison, T.M., Murphy, M.A., Grove, M., Nie, S., Ryerson, F.J., Xiao Feng, W., and Zeng Le, C., 1999, Tertiary deformation history of southeastern and southwestern Tibet during the Indo-Asian collision: Geological Society of America Bulletin, v. 111, p. 1644–1664, https://doi.org/10.1130/0016-7606(1999)111<1644:TDHOSA>2.3.CO;2.

Zeitler, P.K., Meltzer, A.S., Brown, L., Kidd, W.S., Lim, C., and Enkelmann, E., 2014, Tectonics and topographic evolution of Namche Barwa and the easternmost Lhasa block, Tibet, *in* Nie, J., Horton, B.K., and Hoke, G.D., Toward an Improved Understanding of Uplift Mechanisms and the Elevation History of the Tibetan Plateau: Geological Society of America Special Paper 507, p. 23–58.

Zhang, B., Zhang, J., and Zhong, D., 2010, Structure, kinematics and ages of transpression during strain-partitioning in the Chongshan shear zone, western Yunnan, China: Journal of Structural Geology, v. 32, p. 445–463, https://doi.org/10.1016/j.jsg.2010.02.001.

Zhang, Z., Ding, H., Palin, R.M., Dong, X., Tian, Z., and Chen, Y., 2020, The lower crust of the Gangdese magmatic arc, southern Tibet, implication for the growth of continental crust: Gondwana Research, v. 77, p. 136–146, https://doi.org/10.1016/j.gr.2019.07.010.

Zhang, Z., Dong, X., Xiang, H., Ding, H., He, Z., and Liou, J.G., 2015, Reworking of the Gangdese magmatic arc, southeastern Tibet: Post-collisional metamorphism and anatexis: Journal of Metamorphic Geology, v. 33, p. 1–21, https://doi.org/10.1111/jmg.12107.

Zhang, Z.M., Dong, X., Santosh, M., and Zhao, G.C., 2014, Metamorphism and tectonic evolution of the Lhasa terrane, Central Tibet: Gondwana Research, v. 25, p. 170–189, https://doi.org/10.1016/j.gr.2012.08.024.

Zhong, D., Wang, Y., and Ding, L., 1991, The Tertiary Gaoligong intracontinental strike-slip fault and its associated extensional structure in Western Yunnan, China, *in* Chinese Academy of Sciences, Institute of Geology and Geophysics, Division of Lithosphere Tectonic Evolution Annual Report 1989–1990: Beijing, Institute of Geology and Geophysics Chinese Academy of Sciences, p. 18–24.

Zhu, D.C., Pan, G.T., Chung, S.L., Liao, Z.L., Wang, L.Q., and Li, G.M., 2008, SHRIMP zircon age and geochemical constraints on the origin of Lower Jurassic volcanic rocks from the Yeba Formation, southern Gangdese, South Tibet: International Geology Review,

Downloaded from http://pubs.geoscienceworld.org/gsa/gsabulletin/article-pdf/doi/10.1130/B36323.1/5738725/b36323.pdf
by University of Nevada Reno user

v. 50, p. 442–471, https://doi.org/10.2747/0020-6814.50.5.442.

Zhu, D.C., Zhao, Z.D., Pan, G.T., Lee, H.Y., Kang, Z.Q., Liao, Z.L., Wang, L.Q., Li, G.M., Dong, G.C., and Liu, B., 2009, Early Cretaceous subduction-related adakite-like rocks of the Gangdese Belt, southern Tibet: Products of slab melting and subsequent melt–peridotite interaction?: Journal of Asian Earth Sciences, v. 34, p. 298–309, https://doi.org/10.1016/j.jseaes.2008.05.003.

Zhu, D.C., Wang, Q., Zhao, Z.D., Chung, S.L., Cawood, P.A., Niu, Y., Liu, S.A., Wu, F.Y., and Mo, X.X., 2015, Magmatic record of India-Asia collision: Scientific Reports, v. 5, p. 1–9, https://doi.org/10.1038/srep17236.

Ziabrev, S., Aitchison, J., Abrajevitch, A., Davis, A., and Luo, H., 2003, Precise radiolarian age constraints on the timing of ophiolite generation and sedimentation in the Dazhuqu terrane, Yarlung–Tsangpo suture zone, Tibet: Journal of the Geological Society, v. 160, p. 591–599, https://doi.org/10.1144/0016-764902-107.

Zibra, I., Lu, Y., Clos, F., Weinberg, R.F., Peternell, M., Wingate, M.T.D., Prause, M., Schiller, M., and Tilhac, R., 2020, Regional-scale polydiapirism predating the Neoarchean Yilgarn orogeny: Tectonophysics, v. 779, https://doi.org/10.1016/j.tecto.2020.228375.

Zuza, A.V., Henry, C.D., Dee, S., Thorman, C.H., and Heizler, M.T., 2021, Jurassic–Cenozoic tectonics of the Pequop Mountains, NE Nevada, in the North American Cordillera hinterland: Geosphere, v. 17, p. 2078–2122, https://doi.org/10.1130/GES02307.1.

Science Editor: Wenjiao Xiao
Associate Editor: Lu Wang

Manuscript Received 8 September 2021
Revised Manuscript Received 25 June 2022
Manuscript Accepted 24 August 2022

Printed in the USA

Downloaded from http://pubs.geoscienceworld.org/gsa/gsabulletin/article-pdf/doi/10.1130/B36323.1/5738725/b36323.pdf
by University of Nevada Reno user